arXiv:1512.07393v1 [physics.ins-det] 23 Dec 2015

Proceedings of the third French-Ukrainian workshop on the instrumentation developments for HEP

***

October 15-16, 2015, LAL, Orsay, France

Participants of the workshop, LAL, Orsay, 16 October 2015

URL: http://french-ukrainian-workshop-2015.lal.in2p3.fr/

Edited by F.A. Danevich
23 December 2015

Contents

Foreword 4

Program 5

On classical and quantum effects at scattering of fast charged particles in ultra-thin crystal 8
S.N. Shul'ga, N.F. Shul'ga, S. Barsuk, I. Chaikovska, R. Chehab

Transition radiation by low-energy relativistic "half-bare" electron 18
N.F. Shul'ga, S.V. Trofymenko, S.Ya. Barsuk, O.A. Bezshyyko

An Improvement to Phase Reconstruction Techniques applied to Smith-Purcell Radiation Measurements with Noise 26
N. Delerue, O. Bezshyyko, V. Khodnevych

Comparison of Smith-Purcell radiation models 28
M. Malovytsia, N. Delerue

Production and applications of parametric X-rays emitted by relativistic particles 35
A.V. Shchagin, I. Chaikovska, R. Chehab

Hybrid and Metal Microdetector Systems for measuring in real time spatial distribution of charged particles and X-rays beams 45
V. Pugatch, I. Momot, O. Kovalchuk, O. Okhrimenko, Y. Prezado

Studies of sensitive area for a single InGrid detector 53
A. Chaus, M.Titov, O.Bezshyyko, O.Fedorchuk

LHCb RMS status and operation at 13 TeV 61
O. Okhrimenko, S. Barsuk, F. Alessio, V. Pugatch

Focusing of relativistic electron Gaussian bunches by nonresonant wakefield excited in plasma 66
V.I. Maslov, N. Delerue, I.P. Levchuk, I.N. Onishchenko

Modelling point defects dynamics in irradiated foils: patterning and pattern selection 74
D. Kharchenko, V. Kharchenko, I. Lysenko

ALERT: A Low Energy Recoil Detector 80
G. Charles

Molybdenum containing scintillating bolometers for double-beta decay search (LUMINEU program) 86
D.V. Poda (the LUMINEU Collaboration)

Foreword

The reports collected in these proceedings have been presented in the third French-Ukrainian workshop on the instrumentation developments for high-energy physics held at LAL, Orsay on October 15-16. Joint developments between French and Ukrainian laboratories and universities as well as new proposals have been discussed. Workshop hosted about 40 presentations from more than 50 participants from the two countries. The program was focused on developments for accelerator and beam monitoring, detector developments, experimental platforms, joint developments for large-scale high-energy physics projects, neutrino physics and medical applications. Organisation of the workshop was possible thanks to the support from Science and Technology Centre in Ukraine (STCU), National Centre for Scientific Research (CNRS) and Linear Accelerator Laboratory (LAL). The workshop was conducted in the scope of the IDEATE International Associated Laboratory (LIA).

Sergey Barsuk

Program

15th October 2015

09:15 Achille Stocchi, Introduction

R&D on accelerators: beam diagnostics

09:30 Nikolai F. Shulga (KIPT and KNU): Quantum effects at radiation by ultrarelativistic electrons in long undulator and at scattering in ultrathin crystals

10:00 Sergii P. Fomin (KIPT), Computer simulation of high energy charged particle passage through aligned crystals

10:15 Oleksiy Fomin (KIPT and KNU), Qausireflection of relativistic charged particle beam by a thin crystal

10:25 Sergii V. Trofimenko (KIPT), Ionization loss and transition radiation processes by high-energy 'half-bare' electron

10:40 Angeles Faus-Golfe (LAL), Electron beam uses and applications in ThomX

R&D on accelerators: beam diagnostics

11:10 Daniil Brzhechko (TSNUK), UA9 - slow extraction

11:20 Vasyl Drozd (TSNUK), Installation and test of the Fiber Beam Loss Monitor at PHIL

11:30 Nicolas Delerue (LAL), Smith-Purcell radiation

11:40 Alexander V. Shchagin (KIPT), Production and applications of X-rays emitted by relativistic particles

11:55 Valery M. Pugatch (KINR), Hybrid and Metal Microdetector Systems for measuring spatial and time distribution of the charged particles and X-rays beams

12:10 Oleksii Kovalchuk (KINR), Design of the Metal Microstrip Detector for the beam profile studies at PHIL

12:20 Oleksandre Okhrimenko (KINR), LHCb RMS status and operation at 13 TeV

12:30 Discussion

R&D on accelerators: lasers, RF and simulations

14:00 V.I. Maslov, I.P. Levchuk, I.N. Onishchenko (KIPT), Focusing of relativistic electron bunches by nonresonant wakefield excited in plasma

14:15 Nicolas Delerue (LAL), New acceleration techniques 14:30 Stéphane Berry (CEA), XFEL village

14:50 Discussion

Nuclear Physics

15:05 Eric Voutier (IPNO), Prospects for a new measurement of the proton radius

15:25 Georgi Georgiev (CSNSM), ALTO

15:45 Giulia Hull (IPNO), R&D on scintillating materials for Nuclear Physics

16:00 Discussion

Medical applications

16:30 Marie Jacquet (LAL)

16:45 Sara Spadola (IMNC), Optimization of an intraoperative beta imaging probe dedicated to tumor margins control during radioguided cancer surgery

17:00 Marc-Antoine Verdier (IMNC), Intrinsic Performances of the MAGICS Compact Gamma-Camera

17:15 Slava Sharyy (IRFU), Development of the innovative detectors for PET at IRFU

17:30 Olga Kochebina (IRFU), CaLIPSO-PET simulation with GATE/GEANT4

17:40 Samuel Meyroneinc (CPO): CPO

18:00 Discussion

18:30 Visit of CPO

16th October 2015

R&D on detectors

09:15 Slava Kubytsky (LAL), Diamond detectors

09:30 Andrey Nagai (LAL), SiPM

09:45 Leonid Burmistrov (LAL), UA9 - CPFM

10:00 (Oleg Bezshyyko, Andrii Chaus), Micromegas/InGrid

10:15 Giovanni Calderini (LPNHE), Si for ATLAS upgrade

10:30 Nikolai I. Maslov (KIPT), Radiation resistance of Si detectors research using electrons and bremsstrahlung of KhIPT linacs

11:00 Dmytro Kharchenko (IAP-Sumy), Modeling Radiation Defects Dynamics and Microstructure Transformations in Irradiated Solids

11:15 Gabriel Charles (IPNO), ALERT: A Low Energy Recoil Tracker

11:30 Denys Poda (CSNSM), Molybdenum containing scintillating bolometers for double beta decay search (LUMINEU program)

11:45 Discussion

Experimental platforms

12:00 Hugues Monard (LAL), ThomX

12:15 Pierre Lepercq (LAL), PHIL

Medical applications

14:00 Slava Sharyy (IRFU), Development of the innovative detectors for PET at IRFU

14:15 Olga Kochebina (IRFU), CaLIPSO-PET simulation with GATE/GEANT4

Experimental platforms

14:25 Oleg Bezshyyko (TSNUK), Leetech

14:35 Sophie Kazamias, Laserix

14:50 Visit of Laserix

Developments for HEP projects

15:50 Maksym Teklishyn (GSI), Charmonium description using decays to hadronic states with LHCb,

16:05 Stephane Monteil (LPC-Clermont), FCC

16:20 Emi Kou (LAL), Flavour Physics at SuperBelle

16:35 Francois Le Diberder (LAL), Flavour Physics at ILC

16:50 Discussion

Neutrino

17:05 Mathieu Bongrand (LAL), SOLID

17:20 Fedor Danevich (KINR), Instrumentation for double beta decay experiments

17:35 Discussion

17:50 LIA discussion

On classical and quantum effects at scattering of fast charged particles in ultrathin crystal

S.N. Shul'ga[a], N.F. Shul'ga[a,b,], S. Barsuk[c], I. Chaikovska[c], R. Chehab[c]

[a] *National Science Center "Kharkov Institute of Physics and Technology", Kharkiv 61108, Ukraine*

[b] *Karazin Kharkiv National University, Kharkiv 61022, Ukraine*

[c] *LAL, IN2P3-CNRS and Université Paris Sud, 91898 Orsay Cedex, France*

Abstract

Classical and quantum properties of scattering of charged particles in ultrathin crystals are considered. A comparison is made of these two ways of study of scattering process. In the classical consideration we remark the appearance of sharp maxima that is referred to the manifestation of the rainbow scatering phenomenon and in quantum case we show the sharp maxima that arise from the interference of single electrons on numerous crystal planes, that can be expressed in the terms of reciprocal lattice vectors. We show that for some parameters quantum predictions substantially differ from the classical ones. Estimated is the influence of the beam divergence on the possibility of experimental observation of the studied effects.

PACS numbers: 29.27.-a, 61.85.+p, 34.80.Pa, 61.05.J

Keywords: relativistic charged particles, thin crystal, scattering, channelling, rainbow scattering, electron diffraction.

1 Introduction

The motion of a fast charged particle near direction of one of its planes or axes can be considered as a motion in the field of continuous planes or strings. These are the cases of particle channelling or over-barrier motion. A number of theoretical and experimental studies have been made devoted to these phenomena (see, e.g., [1, 2, 3, 4, 5, 6] and references therein). In order to describe the effects of interaction of a charged particle with medium we must get first of all the characteristics of its motion.

Interesting phenomena may happen just at the beginning of such motion, in the transitional area before the particle has completed several oscillations inherent in channelling or above-barrier motion in this case. Such a regime is realized in crystals thin enough, with the thicknesses that vary from less than tenths of micron (hundreds of Å) for MeV particles to several tens of microns for hundreds of GeV particles (the characteristic dimension of such an area depends on the particle energy as a square-root function). In our study we will call these ultrathin crystals. In this work we will mostly consider few-MeV charged particles, so our range of crystal thicknesses spreads from about hundreds up to thousands of Ångströms. In the last years the technologies were developed to produce such crystals, and these crystals have been used for channelling experiments [7, 8, 9, 10, 11]. In the paper we will propose the experimental study of angular distributions of electrons scattered by an unltrathin crystal.

The problem of obtaining characteristics of the motion of a charged particle in these conditions may be resolved both by means of quantum and classical theories, at that higher is the particle energy, more the quantum and classical solutions match one other.

In this work we will stress on the energies low enough so as quantum effects become essential in the particle motion but still high enough so that the crystal thickness required for observing these effects was reachable. For electrons we can propose the study at energies 4 Mev for mostly quantum motion and 50 MeV where some comparison of quantum results with the classical ones begins to be reasonable. The conditions, necessary for the study of phenomena considered in this paper, can be met with use of modern technologies of creating ultrathin crystals and the experiments can be realized on the base of accelerators PhIL and ThomX in the laboratory LAL in Orsay, France.

In this paper we consider the case of planar scattering only as the one which reveals the essence of the nature of the processes, two-dimensional case of axial scattering being mostly only a generalization of it (although, some phenomena as, for example, dynamical chaos, will be only possible at axial scattering). Our observations require low beam divergence, so one should aspire to get it low for experiments. It is possible to improve the divergence by squeezing the beam in the direction perpendicular to crystal planes using magnetic field: simultaneously the beam will stretch out along the planes but this would create no problem in our one-dimensional study.

Here we will consider the case of parallel incidence of a particle relatively a crystal plane. The incidence under a small angle relatively plane reveals other interesting effects and is a subject of a separate study.

2 Classical scattering

We can consider the interaction of a fast particle with matter both within the classical and the quantum theory. The classical theory of scattering is based upon the definition of the particle trajectory in external field. At motion of a particle along crystal planes its trajectory in transversal direciton is defined as a solution of the differential equation of motion [1, 2, 3, 4, 5],

$$\ddot{x} = -\frac{c^2}{E_\parallel}\frac{\partial}{\partial x}U\left(x\right), \tag{1}$$

where x is the coordinate of the particle in the plane of transverse motion, $E_\parallel = c\sqrt{p_\parallel^2 + m^2c^2}$ and $U(x)$ is the potential energy of a particle in the continuous potential of crystal planes. In this article we will neglect such phenomena as multiple scattering or radiation energy losses of a particle by assuming them to be small enough, that is the consequence of a small crystal thickness, therefore small particle path in the field of atomic forces.

The continuous potential of a crystal plane is obtained as the average of the fields of atoms along it with taking into account of random deviations of atom positions relatively their places in the lattice caused by heat oscillations [5]. As a model of a solitary atom potential we took the Molière potential that is widely used to describe atomic electric forces. In order to obtain the potential of entire crystal along the chosen direction we must summarize all non-negligible contributions of the neighbouring planes.

So, for both positively and negatively charged particles (PCP and NCP) in a crystal the continuous plane potential is a series of periodically placed potential wells and potential barriers.

We must turn the potential upside down making the wells become barriers and vice versa if the sign of particle charge changes to the opposite (see Figure 1).

In this case the potential in the neighbourhood of the bottom of the well for both PCP and NCP can be approximated by a parabola

$$U(x) = b(x - x_0)^2 + d, \tag{2}$$

where the parameters x_0, b, d may be found using a fitting procedure. The solution of equation of motion (1) in the case of particles moving in such parabolic potential (in the case of parallel incidence) is a set of harmonic curves $x = x_0 \cos \omega t$, where $\omega = \sqrt{2c^2 |b| / E_\parallel}$, therefore the spatial period of oscillations is

$$T = \pi\beta\sqrt{2E_\parallel / |b|}\,, \tag{3}$$

where $\beta = v/c$. We can define T_0 as the basic oscillation period that corresponds to a particle entering in the crystal in immediate proximity to the well bottom x_0. As we move away from x_0, the form of real potential deviates from the parabolic one, therefore the oscillation periods deviate from T_0. We can compare such a behaviour of NCP and PCP by analysing the difference between the real continuous potential and its fit by parabolas.

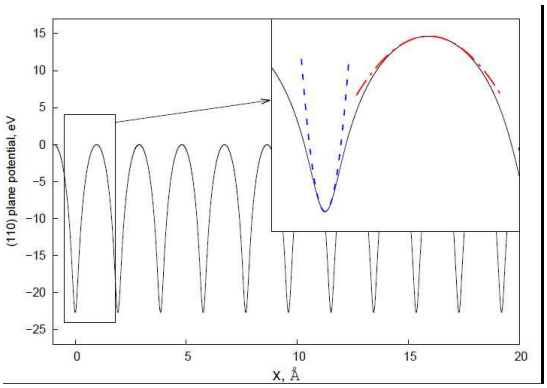

Figure 1: Continuous potential of the plane (110) of Si crystal (solid line) and its approximations by quadratic functions of coordinates near extrema (blue dashed line – approximation of the potential well for negative particles, red dash-and-dot line – the one for positive particles, in this case is turned upside down)

As far as in some vicinity of the well bottom the real potential remains close enough to its quadratic approximation, some part of particles falling into a crystal are "focused" after scattering if the crystal thickness is a small integer number of half-periods $T_{\frac{1}{2}} = T_0/2$ of the particle oscillations within the approximated parabolic potential (2). As the thickness increases, the focusing effect weakens because of increasing difference of real coordinates of the oscillation nodes for different impact parameters. Obviously, the strongest focusing is observed at the first half-oscillation, $L = T_{\frac{1}{2}}$. We can see in Figure 1 that the bottom of the potential well for PCP is approximated by a parabola much better than for NCP. It means that PCP will be focused more strongly and that the focusing effect will persist for a larger number of periods than for NCP (moreover, as stated below, the oscillation period for PCP is much larger than for NCP,

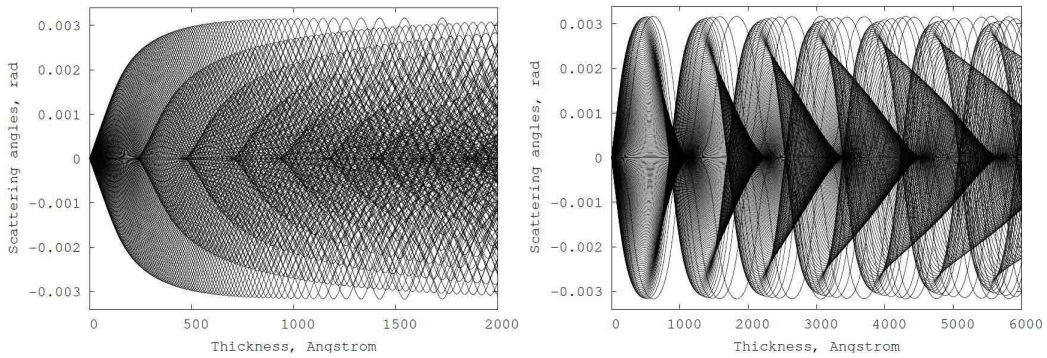

Figure 2: Classical scattering angles for different impact parameters of 4 MeV electrons incident onto a 2000 Å Si crystal parallel to (110) plane (left) and for different impact parameters of 4 MeV positrons incident onto a 6000 Å Si crystal parallel to (110) plane (right)

so the thickness where the focusing effect can be observed is substantially larger for PCP than for NCP that is caused by these two factors).

For positively ($^+$) and negatively ($^-$) charged particles the parameters $b^\pm$ in the fit (2) of the potential of the (110) plane of Si crystal are $|b^+| = 17.01\,\mathtt{eV/Å}^2$ and $|b^-| = 407.6\,\mathtt{eV/Å}^2$. Therefore, we have

$$\begin{aligned} T^+_{\frac{1}{2}} &= 0.5385\beta\sqrt{E_\parallel[eV]}\mathtt{Å}, \\ T^-_{\frac{1}{2}} &= \quad 0.11\beta\sqrt{E_\parallel[eV]}\mathtt{Å}. \end{aligned} \tag{4}$$

So, for this crystal plane the period for positively charged particles is almost 5 times larger than for negatively charged particles, that is only explained by the geometry of potential.

From Figure 1 we see that, as far as we go away from the well bottom, the real potential curve for NCP becomes wider than its parabolic approximation and the one for PCP becomes narrower. This fact causes different symmetry of the scattering pictures for NCP and PCP in the neighbourhood of thicknesses $L = n{\cdot}T_{\frac{1}{2}}$, where n is an integer number, what is observed at comparison of both graphs of Figure 2: we see that because of this the caustic lines for PCP cross among themselves, and the number of crossing caustics increases with thickness, that all not being observed for NCP.

Figure 2 is a set of scattering angles of fast charged particles with a large number (200) of different impact parameters uniformly distributed throughout the full interval between planes. The maximal angular amplitude of oscillations in these graphs (along vertical axis) corresponds to the critical channelling angle,

$$\psi_c = \sqrt{2U_{\max}/E_\parallel}. \tag{5}$$

The difference in these pictures is only caused by the asymmetry of planar potential relatively turnover upside down that is connected with the change of sign of the particle charge. We can see that entire scattering picture for PCP even changes its entire angular dimensions at first half-periods of oscillations, while in the case of NCP it quickly reaches its maximal value and then only changes its internal structure. Near each "focusing point" we see a caustic line enveloping the curves with similar impact parameters, coming out from this focusing point. As the thickness exceeds the "focusing point" the angular density having there a sharp maximum

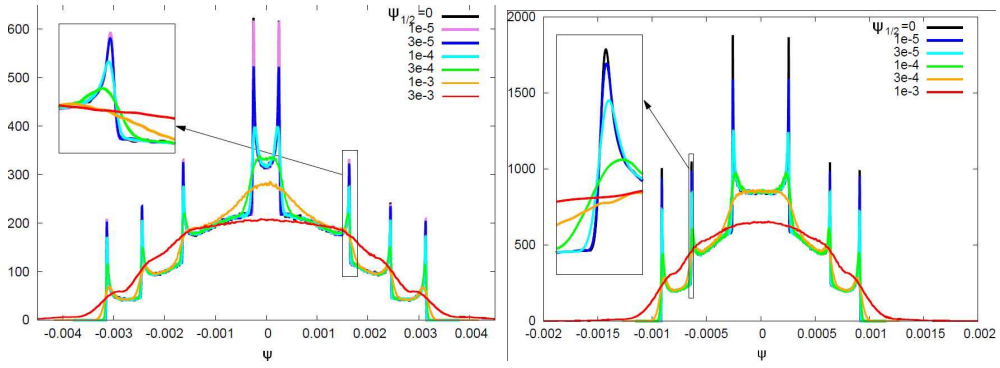

Figure 3: Classical simulation for scattering with different initial divergences for beams of 4 MeV electrons by a 750 ÅSi crystal (left) and 50 MeV electrons by a 2000 Å Si crystal (right), both along the (110) plane

begins to bifurcate, and the two shown up maxima branch off in opposite directions, as observed in the plot of angular distributions of scattered electrons. The sections of the graphs of Figure 2 at constant thickness are proportional to the density of trajectories. By using these sections one can build the angular distributions of electrons scattered by crystal planes (see Figure 3). Near the caustic lines, we have a strong increase of the density of lines from one side and abrupt decrease from the other. The angular distribution (Figure 3) it is manifested as sharp maxima at corresponding angles, the angular distance between maxima being spread with the increase of thickness. We treat the presence of such sharp maxima as an appearance of the rainbow scattering phenomenon [12]. It, applied to axial channelling, is studied in works [13, 14, 15, 16, 9, 10].

A real beam is not parallel, and, as far as we consider the angular properties of scattering, we must account for this fact. In order to do this, we performed a simulation of the scattering picture of charged particles of a beam with different initial angular spread (Figure 3). The ideal situation of a parallel beam is also considered in order to see a "pure" picture. We can see that, as far as the initial beam spread increases, the rainbow lines disappear being smeared. We consider the angular distribution of the particles in the initial beam as gaussian, and characterize the angular spread using the parameter "half-width-at-half-maximum" that means that at the angle corresponding to this parameter we have half of the maximal beam intensity (which is observed in center). We will designate this parameter as $\psi_{\frac{1}{2}}$.

By performing a simulation and using such parameters for the description of a beam, we will see that in order to see the rainbow effect in classical study at scattering of, e.g., 4 MeV electrons in 750 Å Si crystal the beam angular spread must be at least not larger than $\psi_{\frac{1}{2}} \sim 3{\cdot}10^{-4} - 1{\cdot}10^{-3}$ rad. The analogous condition for 50 MeV electrons in the 2000 Å Si crystal gives us $\psi_{\frac{1}{2}} \sim 1{\cdot}10^{-4} - 3{\cdot}10^{-4}$ rad, being in both cases about $0.1 - 0.3\ \psi_c$.

So, as we can see, the conditions imposed on the beam quality in order to see the sharp maxima in classical study are strong enough, although we find them to be reachable.

3 Quantum scattering

In order to realize the quantum study we need to describe the initial beam as a wave packet, instead of the set of point-like particles as in classical case, and to study its development with time. As in the classical case, we must take into account that the initial beam has some spatial dimensions and angular spread. The analysis of the wave function will give us the information about the wave packet motion.

Within the quantum theory, a fast particle moving in a certain direction can be presented as a plane wave. A beam as a set of particles is therefore a set of plane waves, their directions of motion being distributed according to the laws of distribution of particles in the beam. We, however, find useful to describe mathematically the single particle wave function as a Gaussian wave packet

$$\Psi\left(x, t=0\right) = \frac{1}{\sqrt{\sigma\sqrt{\pi}}} \exp\left(-\frac{x^2}{2\sigma^2} + i\frac{p_x x}{\hbar}\right), \tag{6}$$

where the parameter σ corresponds to the wave packet that covers a large number of neighbouring planes, hence, through the uncertainty relations, follows a very low angular divergence of such a wave packet.

In order to find the evolution of quantum state of the system with time we used the action of the time evolution operator onto the wave function. Such a way, with purpose to study the bound states levels, has been used in the works [17, 18, 19, 20, 21, 22].

The essence of our way of finding the evolution of wave packet is following: the change of the wave function with a time step δt is obtained as a result of action of the time evolution operator onto its last step value:

$$\Psi\left(x, t+\delta t\right) = \exp\left(-\frac{i}{\hbar}\delta t\, \hat{H}\right) \Psi\left(x, t\right). \tag{7}$$

But, we must take into account that the Hamiltonian of transverse motion is a sum of two *non-commutating* terms

$$\hat{H} = -\frac{\hbar^2 c^2}{2E_{\|}} \frac{d^2}{dx^2} + eU\left(x\right), \tag{8}$$

that calls forth that we cannot present the exponent (7) of the hamiltonian (8) as a simple consequent product of exponents. This does not let us take δt as large as desired that would be in the case of absence of the potential, and we need to look for some approximation in order to get valuable results. In order to perform the expansion of the exponent in (7) in series in terms of δt we may use the Zassenhaus product formula. So, with precision up to terms proportional to $(\delta t)^3$, we have:

$$\begin{aligned} &\exp\left(-\tfrac{i}{\hbar}\,\delta t \hat{H}\right) \approx \\ &\exp\left(-\tfrac{i}{2\hbar} eU\left(x\right)\delta t\right) \exp\left(i\tfrac{\hbar c^2 \delta t}{2E_{\|}} \tfrac{d^2}{dx^2}\right) \exp\left(-\tfrac{i}{2\hbar} eU\left(x\right)\delta t\right). \end{aligned} \tag{9}$$

In order to deal with the differential operator as an exponent index and not to calculate higher order derivatives we may take use of Fourier series formalism in which taking the derivative is reduced to the multiplication of each Fourier series term by a number. This procedure is exposed in the works [17, 21, 22], and so on.

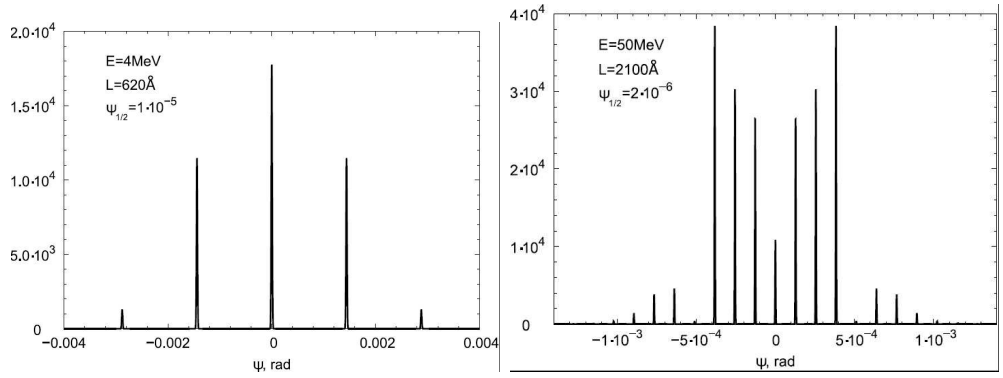

Figure 4: Diffraction of single electrons on (110) planes of Si crystal

Once we have the wave function in position space we can take a Fourier transform in order to get it in momentum space. Therefore, by taking the square of its absolute value we obtain the angular distribution of scattered particles in quantum case. So, the probability for the particle scattering in the interval $[\psi, \psi + d\psi]$ is

$$dw(\psi) = \left| \int \Psi\left(x, t = L/v\right) e^{-ip_{\parallel}\psi x/\hbar} dx \right|^2 \frac{p_{\parallel} d\psi}{2\pi\hbar}. \tag{10}$$

In our study the wave functions describing single particles correspond to almost plane waves with the divergence of about $\psi_{\frac{1}{2}} \sim 0.001\psi_c$. In Figure 4 we can see that the diffraction picture of single electrons in crystal is a row of δ-like maxima. The set of equidistant narrow maxima can be explained as the expansion in reciprocal lattice vectors. We can represent the particles as waves with the wavelength equal to the de Broglie length $\lambda\!\!\!^{-} = \hbar/p_{\parallel}$, therefore the angles corresponding to the maxima must satisfy the relation

$$\psi_n = g_n/p_{\parallel}, \tag{11}$$

where $g_n = 2\pi\hbar n/d_x$ is the reciprocal lattice vector, n – integer number and d_x is the distance between the crystl planes. By the other words, we consider the crystal as a diffraction grating and the particles scattering – as a scattering of de Broglie waves on this grating, so the sharp maxima present on Figure 4 we explain as the manifestation of the interference of electrons with themselves at scattering on different planes. Higher is the particle energy, more densely the allowed angles for particle scattering are situated. As far as the distance between the peaks is proportional to $1/E$ (11) and the channelling angle $\psi_c \propto 1/\sqrt{E}$, for higher energies we have the number of quantum peaks inside the scattering range increasing proportional to the square root of E. We can estimate the number of peaks: $N_p \approx \psi_c/\psi_T = \frac{\sqrt{2U_{\max}}d}{2\pi c\hbar}\sqrt{E}$. For the (110) plane of Si crystal it is approximately $N_p \sim \sqrt{E[MeV]}$.

We get the results for scattering in quantum case by averaging contributions of solitary wave packets of single charged particles by summing up their contributions with Gauss distribution function that modulates the beam divergence:

$$\overline{w_{beam}(\psi)} = \frac{1}{\sigma_b\sqrt{\pi}} \int e^{-\psi_i^2/\sigma_b^2}\, w(\psi_i, \psi)\, d\psi_i, \tag{12}$$

where $\overline{w_{beam}(\psi)}$ states for the density of probability of scattering of the beam incident as a whole parallel to the crystal planes in the direction ψ, and $w(\psi_i, \psi)$ is the density of probability that the particle incident at the angle ψ_i to the planes is scattered in the direction ψ.

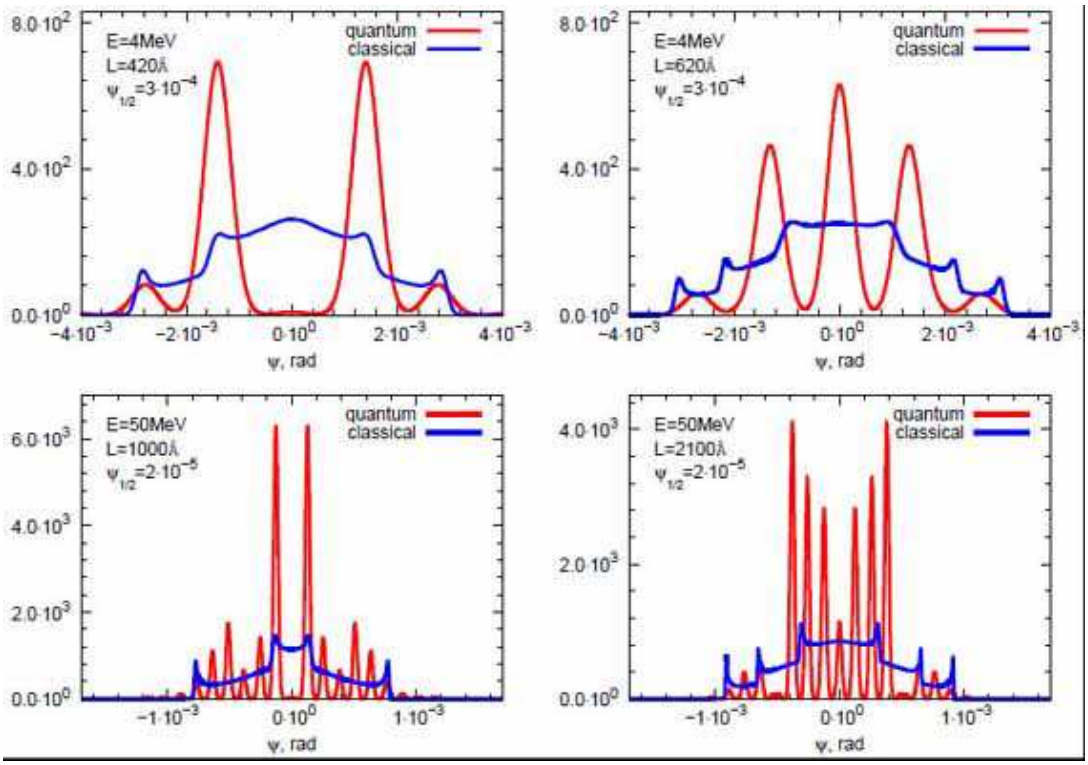

Figure 5: Quantum and classical simulations of angular distribution of 4 MeV (above) and 50 MeV (below) electrons scattered in a Si crystal incident parallel to the (110) plane

It is possible to compare quantum results for angular distributions with the classical ones at the same parameters. In Figure 5 we present quantum angular distributions obtained by the method described here and the classical ones as solutions of the classical equation of motion (1). We see that, lower is the particle energy, greater is the difference between the classical and quantum pictures. Particularly for low energies, the classical and quantum pictures may be substantially different. Besides, the averaging over a diverging beam in quantum case can make neighbouring maxima flow together, make them disappear or displace them. For example, on the picture for 420 Å we see that the central part of the angular distribution of scattering, being elevated in classical distribution, is strongly depressed in quantum case. From the other hand, for higher energies, the sharp maxima observed in classical pictures have some manifestation in quantum case: for the angles that correspond to them the quantum peaks are higher, and for GeV energies they flow together so as quantum picture approaches the classical one.

As written above, the positions of quantum and classical maxima have different nature, so the positions of quantum ones do not depend on the crystal thickness (at the absence of strong influence of the beam divergence), whereas the classical ones migrate towards outside of the scattering figure with the increase of thickness, so any coincidence of classical and quantum maxima is accidental. It can be observed at one crystal thickness and not be observed for another one.

4 Conclusion

In this paper we propose an idea for experiment on planar scattering of fast charged particles in ultrathin crystal, in order to observe quantum and classical effects that can manifest themselves in scattering picture. If the quality of beam and crystal is good enough and the resolution of detectors is high enough we expect the observing of a series of spots of different brightness that, by varying the initial parameters may be referred to manifestation of quantum or classical nature of processes at interaction of charged particles with ultrathin crystal.

The obtained results for angular distributions of the electrons scattered by a ultrathin crystal show that, for Si crystal with thickness about several hundreds of Å the quantum effects at scattering can be essential, that are connected with the interference effect of single electrons on a set of crystal planes. This effect is particilarly bright for the electrons energies about a few MeV. As the plots on Figure 5 show, the electron beam must have parameters attainable on the PhIl and ThomX facilities in the laboratory LAL in Orsay, France.

We did not include in this paper the study of the levels of transversal energy of particles that they occupy in the potential wells of crystal potential. These energy levels are to be observed by using other technical measures, such that will let us register the photons irradiated at interaction of charged particles with crystal, so such observations could reply the question about the mechanisms of arising of these levels and their nature, whether they are connected only with the potential well form or also with the reciprocal influence of neighbouring crystal planes and interference of charged particles on them. These questions could be answered by performing, in addition and in connection with the study proposed in this paper, of another study of radiation arising at interaction of charged particles with ultrathin crystal.

5 Acknowledgement

Research conducted in the scope of the IDEATE International Associated Laboratory (LIA). The work was done with partial support of the NAS of Ukraine, project Φ-12 and of Ministry of Education and Science of Ukraine (project no. 0115U000473). One of the authors (S.N. Shul'ga) is grateful to the Laboratoire de l'Accélérateur Linéaire where the essential part of this work was done and its researchers for the hospitality and fruitful discussions.

References

[1] J. Lindhard, Dansk. Vidensk. Mat.-Fys. Medd. **34** (1965) No. 14.

[2] D.S. Gemmell, Rev. of Mod. Phys. **46** (1974) 129-227.

[3] M.A. Kumakhov, Radiation by channelled particles in crystals. Energoatomizdat Publ., Moscow, 1986 [in Russian].

[4] V.A. Bazylev, Z.K. Zhevago, Radiation of Fast Particles in Matter and External Fields. Nauka Publ., Moscow, 1987 [in Russian].

[5] A.I. Akhiezer, N.F. Shulga, High Energy Electodynamics in Matter, G&B, London, 1996.

[6] P. Rullhusen, X. Artru, P. Dhez, Novel Radiation Sources Using Relativistic Electrons From Infrared to X-Rays. World Scientific, 1998, 202 p.

[7] V. Guidi, A. Mazzolari, et al., Physical Review Letters **108** (2012) 014801.

[8] Z.Y. Dang, M. Motapothula, et al., Applied Physics Letters **99** (2011) 223105.

[9] M. Motapothula, S. Petrović, N. Nešković, et al., Phys. Rev. **B86** (2012) 205426.

[10] M. Motapothula, Z.Y. Dang, et al., NIM **B283** (2012) 29-34.

[11] M. Motapothula, Z.Y. Dang et al., Phys. Rev. Lett. **108** (2012) 195502.

[12] H.M. Nussenzveig, Diffraction Effects in Semiclassical Scattering, Cambridge University Press, Cambridge, 1992.

[13] H.F. Krause, S. Datz, P.F. Dittner, et al. Phys. Rev. **B33** (1986) 6036-6044.

[14] N. Nešković Phys. Rev. **B33** (1986) 6030-6035.

[15] S. Petrović, M. Ćosić, and N. Nešković, Phys. Rev. **A88** (2013) 012902.

[16] N. Nešković and B. Perović, Phys. Rev. Lett. **59** (1987) 308-310.

[17] M.D. Feit, J.A. Fleck, Jr. et al., Journ. of Comp. Phys. **47** (1982) 412-433.

[18] S.B. Dabagov, L.I. Ognev, NIM **B30** (1988) 185-190.

[19] S.B. Dabagov, L.I. Ognev, Journ of Techn. Phys. **58** (1988) 256-264 [in Russian].

[20] S.B. Dabagov, L.I. Ognev, Journ of Techn. Phys. **58** (1988) 1695-1701 [in Russian].

[21] A.V. Kozlov, N.F. Shulga, V.A. Cherkaskiy, Phys.Lett. **A374** (2010) 4690-4694.

[22] N.F. Shul'ga, V.V. Syshchenko, V.S. Neryabova, NIM **B309** (2013) 153-156.

Transition radiation by low-energy relativistic 'half-bare' electron

N.F. Shul'ga [a,b], S.V. Trofymenko[a,b], S.Ya. Barsuk[c], O.A. Bezshyyko[d]

[a] *Akhiezer Institute for Theoretical Physics of National Science Center 'Kharkov Institute of Physics and Technology ', Kharkov, Ukraine*
[b] *Karazin Kharkov National University, Kharkov, Ukraine*
[c] *LAL, Université Paris-Sud, CNRS/IN2P3, Orsay, France*
[d] *Taras Shevchenko National University of Kyiv, Kyiv, Ukraine*

Abstract

The problem of transition radiation generated by relativistic electron which has non-equilibrium electromagnetic field around it at its impinging upon conducting plate is considered. The conditions under which such non-equilibrium ('halh-bare') state of electron significantly influences upon characteristics of the particle transition radiation are discussed. It is proposed to investigate experimentally such influence for incident electrons at low energies (several MeV).

PACS numbers: 41.60.Dk

Keywords: Transition radiation, 'half-bare' electron

1 Introduction

When a charged particle traverses the interface between two media with different electromagnetic properties transition radiation (TR) is generated. In usual statement of the problem about TR of a particle traversing single interface the radiation characteristics depend on physical properties of the media, the particle energy and the angle of its incidence upon interface. It is usually assumed that the particle, before impinging upon interface, moves uniformly and rectilinearly during long period of time and has equilibrium coulomb field around it. This is however not the case for particles which change their state of motion (accelerate) before traversing the boundary between media. Such situation, for instance, takes place if a particle before impinging upon the interface is deflected from the initial direction of motion (by external field or bent crystal) (Fig. 1a).

According to [1, 2], by the moment of time t after deflection the electromagnetic field inside the sphere of radius $R = ct$ (c is the speed of light) with the center in the deflection point will coincide with coulomb field of the particle moving in final direction while outside the sphere (the region of space which the signal about deflection has not yet reached) it is still coulomb field of the particle moving in the initial direction. During some period of time after deflection the field around the deflected particle is non-equilibrium. The spectrum of virtual photons which constitute the field of scattered particle lacks significant part of frequencies comparing to corresponding spectrum of equilibrium coulomb field. The restoration of the field around the particle after scattering occurs in such way that each single-frequency component of this field (Fourier component or virtual photon) regenerates only on distance from the deflection

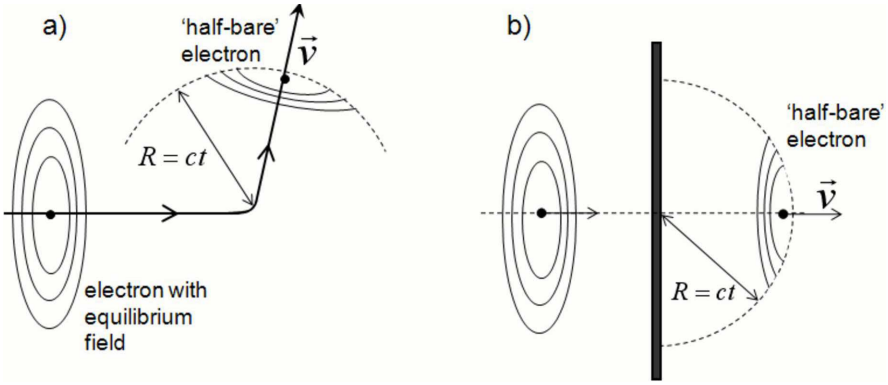

Figure 1: Schematic structure of electromagnetic fields around the particle after its deflection to a large angle (a) and after traversal of a conducting plate (b).

point known as coherence length: $l_C \sim \gamma^2\lambda$, where γ is the particle Lorenz-factor and λ is the wavelength of the considered component. The deflected (scattered) electron with such incomplete electromagnetic field around it is known as 'half-bare' electron. Here we use the notion of deflection 'point' which is valid if consider the Fourier components of the fields produced in this process for which $l_C >> a$, where a is the characteristic linear size of the region in which deflection occurs. The condition $R >> a$ should be fulfilled as well.

The manifestations of such non-equilibrium state of high-energy (multi-GeV) electron were previously theoretically considered [3, 4, 5, 6] and experimentally observed [7, 8, 9, 10] in bremsstrahlung emitted by the particle during its multiple scattering on the atoms while moving through substance. In this case the 'half-bare' state, in which electron appeared after scatterings, resulted in suppression of radiation intensity in certain frequency range (Landau-Pomeranchuk-Migdal [3, 4] and Ternovsky-Shul'ga-Fomin [5, 6] effects).

In the present paper we propose to study the influence of 'half-bare' state of electron upon its millimeter wavelength TR characteristics which is generated at impinging of such electron upon thin conducting plate situated in vacuum at several MeV energy of incident electrons (which corresponds to the energy of electrons delivered by photoinjector PHIL at LAL Orsay). The plate could be placed in the final direction of motion of deflected electron in the vicinity of the deflection area. However calculations [11] show that the considerable change of TR characteristics (due to 'half-bareness' of the particle) takes place in the case when relatively large deflection angle ($\chi >> 1/\gamma$) is obtained within the area much smaller than the coherence length l_C for the considered radiation wavelength. At low energies it is technically difficult to realize such condition and another way of obtaining electrons in 'half-bare' state is needed. The considerations made in [12] show that the structure of electromagnetic field around the electron analogous to the one after the particle deflection to a large angle could be obtained by electron traversal of thin conducting plate (Fig. 1b). Hence, characteristics of TR generated by preliminarily deflected electron should be analogous to the ones of TR emitted by electron which before impinging upon the second plate 'undresses' traversing the first one and the latter process is proposed to be used for investigation of 'half-bare' electron TR at low particle energies.

2 Transition radiation by low-energy 'half-bare' electron at oblique incidence upon conducting plate

Let us note that the study of radiation in millimeter wavelength region generated during high-energy electron traversal of a system of two conducting plates (Fig. 2) was previously made in the work [13]. In this work the coherent TR generated by 150 MeV bunched electron beam which traversed a radiator system consisting of an upstream aluminum foil and a downstream inclined aluminum mirror was investigated. In the considered experiment radiation suppression (comparing to radiation on a single mirror in the absence of the foil) and its gradual growth with the increase of distance between the mirror and the foil was observed. It is necessary to note that the foil and the mirror of rather small transversal (with respect to the direction of the electron velocity) size were used and in most part of the measurements this size was smaller than characteristic transversal size of electromagnetic fields of impinging electrons. This makes the characteristics of generated radiation influenced by diffraction of electromagnetic field on the plates edges and different from the corresponding characteristics of TR from an infinite target. However, as follows from the paper, it was the theory of TR generated on the plates of infinite size which was used to interpret the experimental data in [13].

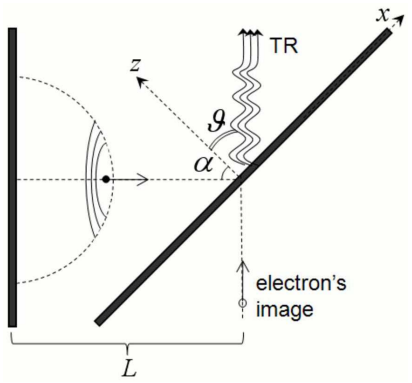

Figure 2: TR by 'half-bare' electron on the inclined plate (for $\alpha = \pi/4$).

In the present paper we propose to investigate the peculiarities of 'half-bare' electron TR in the millimeter wavelength range at low energies (several MeV). At such energies the characteristic transversal size of the particle's own field (for the given wavelength it is defined by expression $l_T \sim \gamma\lambda/2\pi$) is quite small and the condition of 'infinite plate' could be easily realized. Such condition means that the linear transversal dimensions of both TR-radiating plates should be larger than l_T and the approximation of infinite size of the plates is valid for theoretical description of measured radiation characteristics. The diffraction of the electron's field on the plates' edges is absent. Moreover under the considered conditions the radiation formation length l_C is rather small (however macroscopic) and it is possible to make the measurements not only for distances (between the plates) much smaller than l_C (as in [13]) but on distances comparable and larger than this value as well. As we show, in this case it is possible to observe new features of 'half-bare' electron TR such as enhancement of radiation intensity comparing to the one emitted by electron with equilibrium field and oscillation of TR intensity with the change of distance between the plates.

The consideration of TR in millimeter wavelength region in our case is also preferable since it allows to make measurements in the wave zone of radiation process (place the detector on distance much larger than l_C from the plates) and not to use additional equipment (parabolic focusing mirrors, for instance) to eliminate the effect of pre-wave zone in radiation measurements [14, 15]. Among the vices of the proposed experimental conditions it is necessary to note the lower intensity of TR comparing to the case of electrons of higher energies.

Let us consider backward (to the half-space from which the electron comes to the plate) transition radiation generated at impinging upon thin conducting plate of 'half-bare' electron which 'undresses' during preliminary traversal of another conducting plate (Fig. 2). As was noted the TR characteristics in the considered case should be similar to TR characteristics in the case of electron traversal of the plate after being deflected to a large angle. In the considered case the second plate (on which backward TR occurs) should have some inclination relatively to the first one (vertical) so that the backward TR could pass the first plate and arrive at the detectors.

The necessity to use the inclined plate in the considered case at rather low energies (the calculations is made for 3.5 MeV electrons) causes significant perturbation of the 'elegant' azimuthally symmetrical structure of TR calculated in high-energy approximation (presented in [13]). Nevertheless in the considered case the 'half-bare' state of electron still significantly influences upon its TR characteristics and could be experimentally registered.

In order to calculate the considered TR spectral-angular density we use the method of images which is valid also in relativistic case if consider radiation from infinite ideally conducting plates [12, 16]. In this method the radiation emitted at 'half-bare' electron impinging upon the inclined plate is considered as radiation produced by electron and its image inside the inclined plate during their motion towards the point of electron traversal of the plate and abrupt stop at this point. Moreover the 'half-bareness' (as a result of electron traversal of another plate) is taken into account by taking the moment of time at which this motion begins as $t_0 = -L/v$, where L is the length of electron's path between the plates and v is the particle velocity. The calculations give the following expression for TR spectral-angular density of 'half-bare' electron in this case:

$$\frac{\pi^2 c}{e^2}\frac{d^2\mathcal{E}}{d\omega do} = \left(\frac{\mathbf{n}\times\boldsymbol{\beta_1}}{1-\mathbf{n}\boldsymbol{\beta_1}}\right)^2 I_1 + \left(\frac{\mathbf{n}\times\boldsymbol{\beta_2}}{1-\mathbf{n}\boldsymbol{\beta_2}}\right)^2 I_2 - \frac{\boldsymbol{\beta_1}\boldsymbol{\beta_2} - (\mathbf{n}\boldsymbol{\beta_1})(\mathbf{n}\boldsymbol{\beta_2})}{(1-\mathbf{n}\boldsymbol{\beta_1})(\mathbf{1}-\mathbf{n}\boldsymbol{\beta_2})} I_{12}, \tag{1}$$

which differs from the corresponding expression for electron with equilibrium field by the presence of interference factors

$$I_1 = \sin^2\left[\frac{\omega l}{2v}(1-\beta_x\sin\theta\cos\phi+\beta_z\cos\theta)\right],$$

$$I_2 = \sin^2\left[\frac{\omega l}{2v}(1-\beta_x\sin\theta\cos\phi-\beta_z\cos\theta)\right],$$

$$I_{12} = \sin^2\left[\frac{\omega l}{2v}(1-\beta_x\sin\theta\cos\phi+\beta_z\cos\theta)\right] + \sin^2\left[\frac{\omega l}{2v}(1-\beta_x\sin\theta\cos\phi-\beta_z\cos\theta)\right] -$$

$$-\sin^2\left[\frac{\omega l}{2v}\beta_z\cos\theta\right].$$

In order to obtain the expression for TR by electron with equilibrium field (see, for example, [17]) we have to put I_1 and I_2 equal to 1/4 while I_{12} equal to 1/2).

The quantity ϕ in (1) is the azimuthal angle in the plane of the inclined plate (the angle between x-axis and projection of radiation direction vector $\mathbf{n}$ on the plate surface). θ is the angle between $\mathbf{n}$ and z-axis. $\boldsymbol{\beta_1}$ and $\boldsymbol{\beta_2}$ are the dimensionless velocities of electron and its 'image' which moves symmetrically to electron with respect to the inclined plate. They have the same magnitude v/c. Also $\beta_x = (v/c)\sin\alpha$, $\beta_z = (v/c)\cos\alpha$ and

$$\mathbf{n}\boldsymbol{\beta_1} = \beta_x \sin\theta\cos\phi - \beta_z\cos\theta,$$

$$\mathbf{n}\boldsymbol{\beta_2} = \beta_x \sin\theta\cos\phi + \beta_z\cos\theta,$$

$$(\mathbf{n}\times\boldsymbol{\beta_{1,2}})^2 = v^2/c^2 - (\mathbf{n}\boldsymbol{\beta_{1,2}})^2$$

For measurements in the wavelength region $\lambda < 5\ mm$ ($\gamma\lambda/2\pi < 0.56\ cm$) a plate (vertical) with transversal size $2\times 2\ cm$ may be used (it should be larger than the transversal size of the electron's coulomb field $2l_T \sim \gamma\lambda/\pi$). If we take $\alpha = \pi/4$ (the inclined plate in this case should have then $\sqrt{2}$ times larger dimension along the x-axis in order to have the same transversal cross-section) the minimal distance L of the electron's path between the plates which can be achieved is $1\ cm$. The expression (1) is valid for arbitrary energies of incident electron and at sufficiently high-energies coincides with expression used in [13].

3 The peculiarities of 'half-bare' electron TR

Changing the distance L, the observation angle θ and the measured TR wavelength λ it is possible to investigate the difference between the 'half-bare' electron TR characteristics and the ones of electron with equilibrium field. According to (1), this difference can manifest itself both in radiation suppression and enhancement, change of angular distribution and dependence of TR intensity on the radiated wavelength (which is absent for TR by electron with equilibrium field).

Fig. 3 shows that the intensity of TR by 'half-bare' electron in the vicinity of the radiation maxima for electron with equilibrium field can be either suppressed or enhanced depending on the value of the parameter $\delta = L/l_C$. Namely, if the condition $\delta << 1$ is fulfilled the radiation will be suppressed (thick solid curve). Otherwise enhancement may take place. In any case the considered TR has wider angular distribution (around the direction of the electron image velocity) than the radiation by electron with equilibrium field. Here we use the denomination $\mathcal{E}_{\omega,o} = (4\pi^2 c/e^2)d^2\mathcal{E}/d\omega do$ for the dimensionless quantity proportional to TR spectral-angular density.

Fig. 4 represents the examples of dependence of TR intensity on distance L between the plates (on the magnitude of the electron 'half-bareness') for different radiation wavelengths.

Again for $\delta << 1$ (the electron's field is significantly suppressed) the radiation is suppressed (thick line on Fig. 4a). For larger values of this parameter radiation is enhanced and further radiation dependence on increasing L has the type of oscillations (Fig. 4b). The possibility to observe at least several such oscillations depends on spectral and angular resolution of the used detector.

Let us note that finite spectral and angular resolutions of the detector should blur small amplitude quick oscillations which exist on all the presented figures and are caused by the first

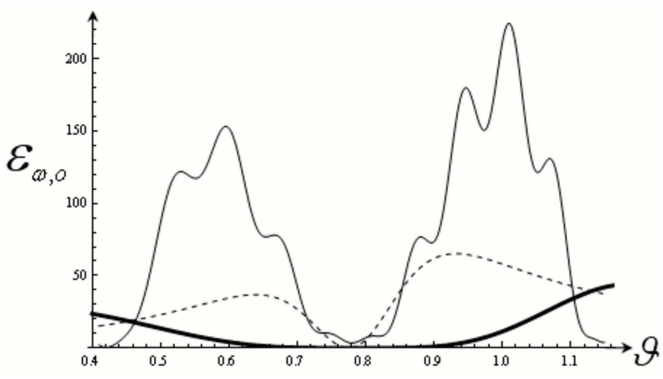

Figure 3: TR angular distribution for $\phi = 0$. Dashed line – radiation by electron with equilibrium field; thin solid line - radiation by 'half-bare' electron for $\lambda = 3\ mm$, $L = 4\ cm$ ($\delta \approx 0.27$); thick solid line – radiation by 'half-bare' electron for $\lambda = 5\ mm$, $L = 1\ cm$ ($\delta \approx 0.04$).

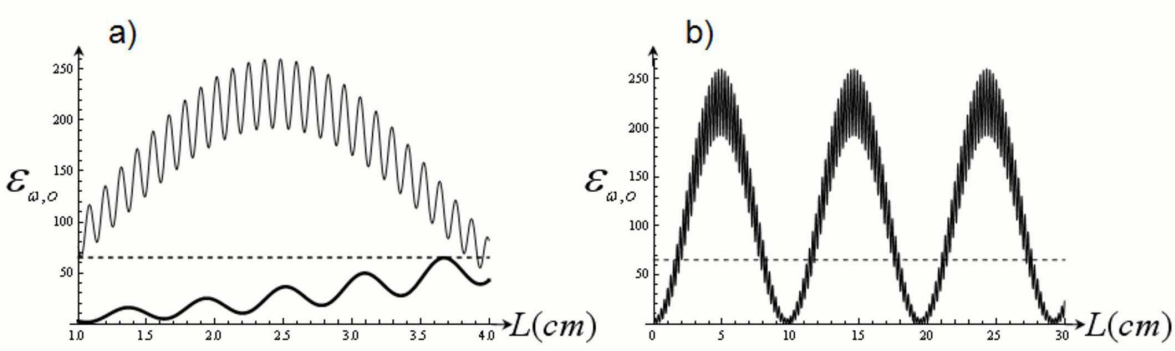

Figure 4: TR dependence on L for $\phi = 0$ and $\theta = \alpha + 1/\gamma$ (TR maximum for electron with equilibrium field). Dashed lines – radiation by electron with equilibrium field. a) solid lines – radiation by 'half-bare' electron for $\lambda = 1\ mm$ (thin line) and for $\lambda = 5\ mm$ (thick line). b) $\lambda = 2\ mm$ for much larger range of L.

and the third terms in (1).

As far as the absolute value of the radiation signal from single bunch is concerned, for the angle of distribution maximum for electron with equilibrium field $\theta = \alpha + 1/\gamma$ it can be estimated as follows (the estimation is made for the case of total coherence of radiation by all 10^9 particles of the bunch):

$$\frac{d^2\mathcal{E}}{d\omega do} \sim 10\ \frac{eV{\cdot}s}{sr}.$$

If the detector used for radiation registration has, for instance, the detection area $2 \times 2\ mm$ and the distance between the detector position and the inclined plate is about 1 meter the total amount of energy radiated by a single bunch in the wavelength range $2\ mm < \lambda < 2.1\ mm$ which detector registers can be estimated as

$$\Delta\mathcal{E} \sim 0.5\ MeV.$$

4 Some aspects of radiation detection technique

The detection technique required for the studies considered above should be efficient in the millimeter-wave range. Currently these detectors are being rapidly developed for a number of applications in science and technology – wide-band wireless applications and communications, automotive radars, safety control, military use, mm-wave astrophysics. Therefore a variety of equipment (generators and detecting systems) for millimeter-wave range is available at the market of industrial and scientific instruments. During last years both branches progress – room-temperature sensors with accompanying electronics (cheaper approach) and cryogenic detector technologies (maximum of sensitivity, it is used primarily for astrophysics). Individual detectors achieved photon noise limited performance for ground-based imaging in the 1990s. The photon noise from only astrophysical sources achievable in space with a cold telescope is of about $10^{-18}\ W/\sqrt{Hz}$, varies somewhat with wavelength, and is within actually demonstrated sensitivities. In this decade imaging will be driven not by cryogenic detector sensitivity but by array formats. Detector arrays have doubled in format every 20 months over the past 10 years. In order to choose a given instrument, we plan a full simulation and bench tests in order to motivate using cryogenic sensitive detectors (or arrays); to determine the main sources of noise; estimate the expected levels of signal in millimeter-wave range.

5 Conclusions

The non-equilibrium state of electromagnetic field around relativistic electron can significantly influence upon characteristics of transition radiation by such electron. This effect can be observed, for instance, after particle deflection from initial direction of motion or during electron traversal of conducting foil. At several MeV energies the second process is more promising for experimental investigations of peculiarities of transition radiation by such 'half-bare' electron. The calculations show that such properties are well pronounced in the millimeter region of radiated wavelengths. Both the radiation intensity suppression and enhancement as well as change of its angular distribution comparing to the case of radiation by electron with equilibrium field could be studied in this case. The results of investigation of transition radiation generated by 'half-bare' particles might be valuable in connection with application of transition radiation based techniques for particle beams analysis. It is relevant, for instance, for deflected beams which consist of particles extracted from from primary linear beams or accelerator storage rings. Such beams may represent the example of beams of 'half-bare' particles.

6 Acknowledgements

The research is conducted in the scope of the IDEATE International Associated Laboratory (LIA). The work was partially supported by the project F12 of NAS of Ukraine, the project no. 0115U000473 of the Ministry of Education and Science of Ukraine and by the project of NAS of Ukraine for young researchers (contract no. M63/56-2015).

References

[1] E.L. Feinberg, Sov. Phys. Usp. 23 (1980) 629 [UFN 132 (1980) 255].

[2] A.I. Akhiezer, N.F. Shul'ga, High Energy Electrodynamics in Matter. – Moscow: Nauka, 1993. – 344 p.

[3] L.D. Landau, I.Y. Pomeranchuk, Doklady AS USSR 92 (1953) 535.

[4] A.B. Migdal, Phys. Rev. 103 (1956) 1811.

[5] F.F. Ternovsky, JETP 39 (1960) 171.

[6] N.F. Shul'ga, S.P. Fomin, JETP Lett. 27 (1978) 117.

[7] P.L. Anthony, R. Becker-Szendy, P.E. Bosted et al., Phys. Rev. Lett. 75 (1995) 1949.

[8] S. Klein, Rev. Mod. Phys. 71 (1998) 1501.

[9] H.D. Thomsen, J. Esberg, K. Kirsebom et al., Phys. Lett. B. 672 (2009) 323.

[10] H.D. Thomsen, J. Esberg, K.K. Andersen et al., Phys. Rev. D. 81 (2010) 052003.

[11] N.F. Shul'ga, S.V. Trofymenko, V.V. Syshchenko, JETP Letters 93 (2011) 3.

[12] N.F. Shul'ga, S.V. Trofymenko, V.V. Syshchenko, Il Nuovo Cimento 34 C (2011) 327.

[13] Y. Shibata, K. Ishi, T. Tokahashi et al., Phys. Rev. E 49 (1994) 785.

[14] M. Castellano, V. Verzilov et al., Phys. Rev. E 67 (2003) 015501.

[15] B.N. Kalinin, G.A. Naumenko, A.P. Potylitsyn et al., JETP Lett. 84 (2006) 136.

[16] V.L. Ginzburg, V.N. Tsytovich, Transition Radiation and Transition Scattering. – Moscow: Nauka, 1984. – 360 p.

[17] F.G. Bass, V.M. Yakovenko, Sov. Phys. Usp. 8 (1965) 420 [UFN 86 (1965) 189].

An Improvement to Phase Reconstruction Techniques applied to Smith-Purcell Radiation Measurements with Noise

N. Delerue[a], O. Bezshyyko[b], V. Khodnevych[b]

[a] *LAL, Univ. Paris-Sud, CNRS/IN2P3, Université Paris-Saclay, Orsay, France*
[b] *Taras Shevchenko National University of Kyiv, Ukraine*

Abstract

We recently reported on an implementation of phase noise reconstruction technique. In further work we found how to further improve our result when there is a strong noise background. We report on this here.

1 Introduction

We recently published a paper comparing different phase reconstruction techniques [1] and making an extensive study of the. After finalizing this paper we realized that it is possible to improve further the performance achieve by such reconstruction techniques when the signal is modified by a strong random noise. Here we report only the improvements to that paper and we invite the interested reader to refer to the original publication [1].

2 High frequency extrapolation

In [1] we used a high frequency extrapolation method inspired from [2]. This method relied heavily on the value of the last point of the spectrum to determine the high frequency extrapolation coefficient. Although this performs well in ideal world simulations this can be significantly affected by noise on this data point.

Further analysis of simulated cases where this method did not perform well by giving incorrect profile FWHM led us to understand that we would get better results by replacing the value of the last data point by an average of the last 3 data points. The figure 1 shows that using this method the error on Δ_{FWHM} is significantly decreased as it is often dominated by the wings of the profile. The χ^2 of the distributions is only marginally affected by the high frequency extrapolation. Interestingly, although this method was meant to address mostly high noise measurements we see that the performance are also significantly improved when the gain is lower.

We have also estimated the performance of our reconstruction method: On a computer Intel Core-i5-3317U at 1.7 GHz computing the reconstruction using the Hilbert transform take 0.025 seconds. Calculating the reconstruction using the Kramers-Kronig method take 155.021 seconds.

3 Discussion

We have found the by modifying the high frequency extrapolation of our phase reconstruction method we significantly reduce the error on the FWHM of the reconstructed profile.

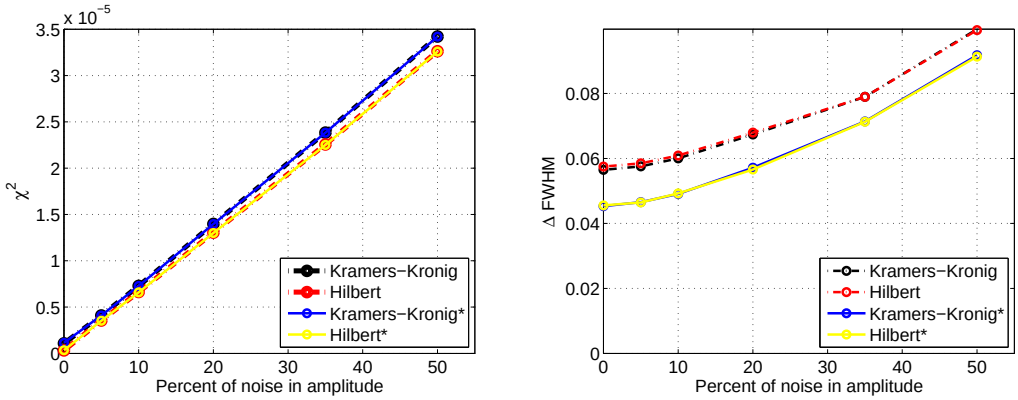

Figure 1: Mean χ^2 and Δ_{FWXM} as function of noise amplitude. The black and red lines correspond to the method published in [1] whereas the data in yellow and blue use the average of the last 3 data point to estimate the high frequency extrapolation coefficients. For each data points 1000 simulations were performed.

References

[1] N. Delerue, V. Hodenych et al. Study of Phase Reconstruction Techniques applied to Smith-Purcell Radiation Measurements. ArXiv 1512.01282, submitted to PRST-AB

[2] R. Lai, U. Happek and A. J. Sievers Measurement of the Longitudinal Asymmetry of a Charged Particle Bunch from the Coherent Synchrotron or Transition Radiation Spectrum. Phys. Rev. E, Vol. 50, No. 6, R4294 1994

Comparison of Smith-Purcell radiation models

Maksym Malovytsia[a,b], **Nicolas Delerue**[b]

[a] *V.N. Karazin Kharkiv National University, School of Physics and Technology, Department of Nuclear and Medical Physics, Kharkiv, Ukraine*
[b] *LAL, Univ. Paris-Sud, CNRS/IN2P3, Univ. Paris-Saclay, Orsay, France*

Abstract

Smith-Purcell radiation is used in several applications including the measurement of the longitudinal profile of electron bunches. A correct reconstruction of such profile requires a good understanding of the underlaying model. We have compared the two leading models of Smith-Purcell radiation and shown that they are in good agreement. We have also studied the interference effects that modulate the signal in the near-field zone.

1 Introduction

Smith-Purcell (SP) radiation [1] has been discovered sixty years ago. This phenomena occurs, when charged particles pass near periodical conductive grating. The wavelength of the radiation produced is given by a simple equation:

$$\lambda = \frac{d}{n}\left(\frac{1}{\beta} - cos\theta\right) \tag{1}$$

where λ is the wavelength of the radiation, d is the period of the grating, n is the order of the radiation and θ is the polar observation angle (see Fig. 1).

There are several ideas of applications based on SP radiation, including non-invasive bunch profile measurement methods [2].

Several models [3] of SP radiation intensity distribution were proposed. Though there are experiment for each of these models, that agrees with these theory a comparison of these models is important to discriminate them experimentally.

It has also been shown in [4] that the predicted intensities should be affected by interference effects.

2 Models

The Surface Current (SC) and Resonant Diffraction Radiation (RDR) models are presented in [3] as a semi-analytical equations, which could be easily calculated, so they are easy to use in the SP radiation simulations. However those expressions are achieved with the assumption that the detector is infinitely far from the source of radiation and grating strips have infinite length.

Karlovets and Poptylitsyn in their work [4] proposed a basic model of SP radiation. The idea was to use Backward Diffraction Radiation (BDR), described in [5], and calculate the intensity on the detector point as interference of the waves from each point of the grating. Using this approach automatically includes grating sizes and source-detector distance. The problem of

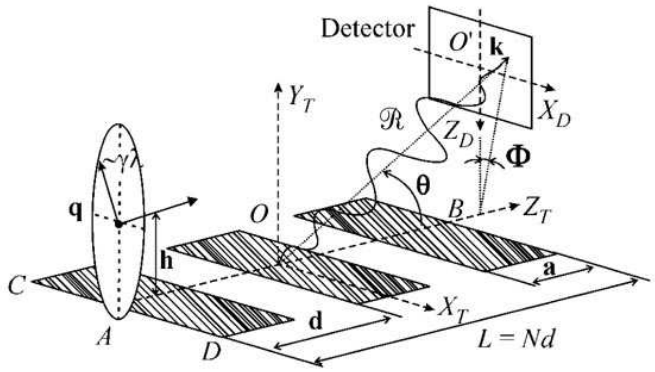

Figure 1: Disposition of the grating, detector, bunch and radiation. Flat grating [4]

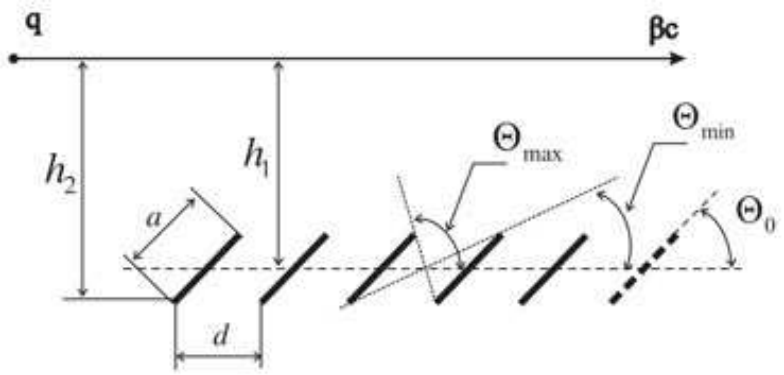

Figure 2: Disposition of the grating, detector and bunch. Grating with inclined strips [3]

using this method is long computation time, as the equations for intensity of SP radiation are expressed through double integrals.

It is also must be mentioned that, unlike SC and RDR models, BDR model proposed in [4] does not include blaze angle θ_0 (see Fig. 2). It could be easily done, by changing every term of the Eq. 8 in [4], that represents beam-grating separation, by variable that depends on the position over the grating. For example:

$$h \to h - \Delta Z_T \sin\theta_0 \tag{2}$$

where, h - impact parameter $-a/2 < \Delta Z_T < a/2$ - position relative to the center of strip, that bunch currently passing.

2.1 Simplifications of BDR

Numerical computation of BDR model requires considerable amount of time, but there are cases, when it could be simplified. For the "full" BDR model next equation was taken, with assumption, that $h >> a/2$:

$$\begin{pmatrix} E_x^D \\ E_z^D \end{pmatrix} = Const \int_{-M/2}^{M/2} dX_T \sum_{m=1}^{N} \int_{-a/2}^{a/2} d\Delta Z_T \; A \frac{K_1\left[\frac{2\pi}{\beta\gamma\lambda}\sqrt{X_T^2+h^2}\right]}{\sqrt{X_T^2+h^2}} \cos\theta_0 \exp\Delta\phi \begin{pmatrix} X_T \\ h \end{pmatrix} \quad (3)$$

$$\begin{aligned} \Delta\phi &= \frac{2\pi}{\lambda}\left(\Delta R + \frac{Z_{Tm} + \Delta Z_T \cos\theta_0}{\beta}\right) \\ \Delta R &= \Big\{ (R_0 \sin\Theta \sin\Phi - X_T)^2 + (R_0 \sin\Theta \cos\Phi - \Delta Z_T \sin\theta_0)^2 \\ &\quad + (R_0 \cos\Theta - Z_{Tm} - \Delta Z_T \cos\theta_0)^2 \Big\}^{\frac{1}{2}} - R_0 \\ Z_T &= Z_{Tm} + \Delta Z_T \cos\theta_0 \\ Z_{Tm} &= \frac{d\,(2m+1-N)}{2} \end{aligned} \quad (4)$$

Here, X_T and Z_T are the coordinates of the point on the grating surface, K_1 is modified Bessel function of the second kind, $\Delta\phi$ is the difference in phases of the waves emitted from arbitrary point of the target and middle of the grating, N is the number of grating strips, ΔZ_T is coordinate of the source point relative to the center of the closest strip, h and d are the same as in Eq. (1) and Eq. (2). In our simulation waves were considered to interfere in one point so X_D and Z_D from [6] had been considered 0.

2.1.1 Far zone

The far zone is the range of distances between the source and the detector at which interference effects are not visible, alternatively it could be said, that it is distances at which we see our grating as single point of radiation. Criterion for the far zone has been obtained by Karlovets and Potylitsyn in [4]:

$$R_0 \gg N^2 d(1+\cos\theta) \quad (5)$$

It was derived from the assumption, that difference in phases of two waves coming from two furthest strips of grating is much smaller than 2π. Using this approximations it is easy to integrals, which will significantly decrease computation time.

2.1.2 Short grating strips

When the detector is closer that the far zone limit different assumption are possible if the following condition is met:

$$R_0 \gg \frac{d}{4(1-\cos\theta)} \quad (6)$$

With this simplification it is possible to obtain single integral expression for the intensity of the SP radiation, but integrated function is more complicated than in case of the Eq. (5).

2.2 Experimental parameters

As parameters for our simulations it was decided to use real experiments, as it would be possible to compare theory with experiment later. The experiments are SPESO at Soleil Synchrotron and E-203 at SLAC. For convenience the initial parameters are presented in the table below.

Parameter/Experiment	SPESO	E-203	E-203	E-203
γ	200	40000	40000	40000
$d, \mu m$	10000	1500	250	50
h, mm	1	1	1	1
$\theta_0, degree$	30	30	30	30
M, mm	100	20	20	20
L, mm	180	40	40	40
R_0	280	220	220	220

Here γ - lorentz factor, d - period of the grating, h - inpact parameter, θ_0 blaze angle, M, L width, length(along the beam direction) of the grating, R_0 - source-detector distance. See Fig. 1, 2

2.3 Comparison of the SC, RDR and BDR

As both SC and RDR models are working in the far zone they could be only compared to the far zone simplification of the BDR model. For these several sets of data were created. For each model for each θ from 40 to 140 degree with a step of 10 degree plots of phi distribution of intensity per solid angle were created and then combined into one figure for comparison. Also plot of ratio between BDR and SC models was made.

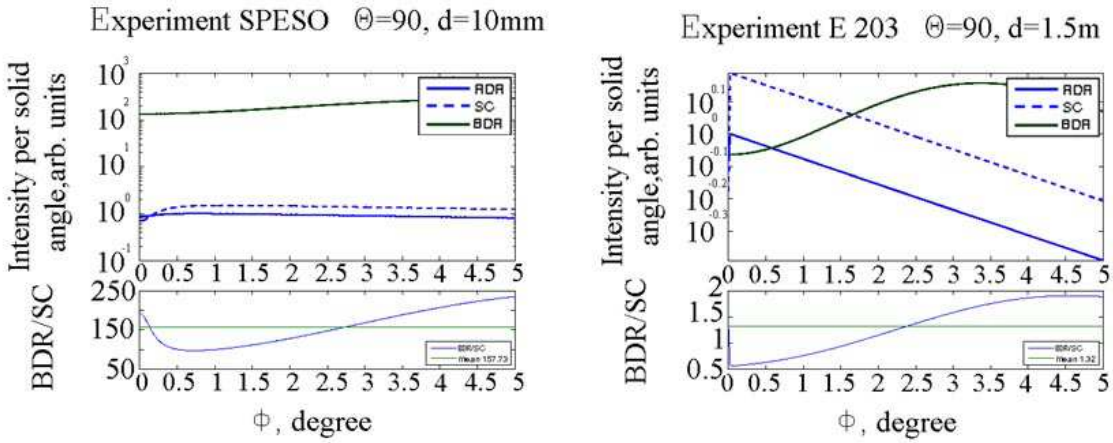

Figure 3: Phi distribution for SPESO(left) and E 203 d=1.5mm(right).

One can see that on the Fig. 2.3 BDR model decreasing slower than on 2.3, it could be easily explained. Even if our source is point-like, it still can have interference at large distances, and interference picture will be dependant on the wavelength and the smaller the wavelength the faster intensity will go down when (in this case) azimuthal angle is changed.

Another problem is despite SC and RDR being close, they are much different from BDR model. This happens because in BDR grating sizes are accounted for. In fact if one start increasing length (M) of the grating strips, simulated BDR model will be becoming more like SC and RDR as shown on Fig. 2.3.

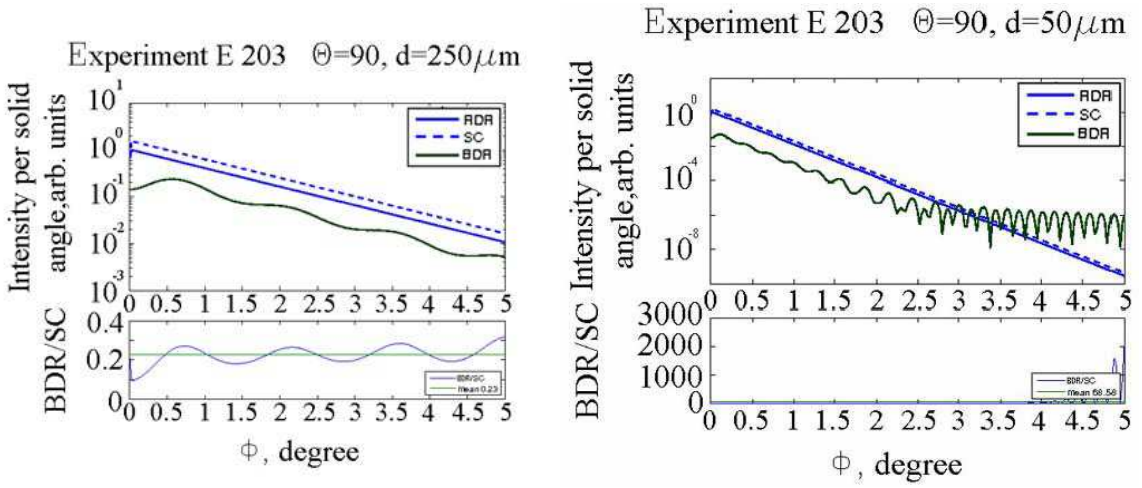

Figure 4: Phi Distribution for E 203 d=250μm(left) and E 203 d=50μm(right)

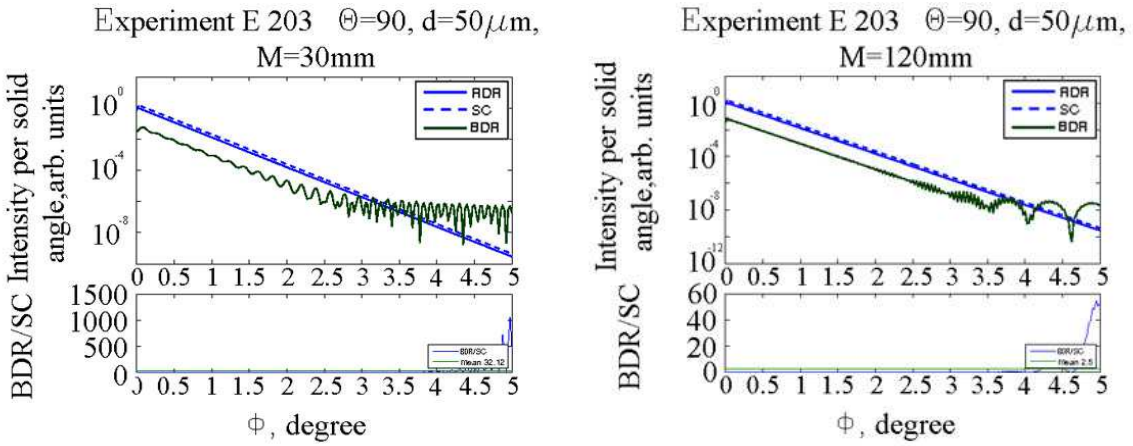

Figure 5: Phi Distribution for E 203 d=50μm M=30mm(left) and M=120mm(right)

As one can see on Fig. 2.3 and Fig. 2.3 the RDR and SC models produce the same angular distribute and the signal intensity are comparable (within experimental uncertainties). It would there fore be difficult to discriminate experimentally between these models.

3 Interference

In far zone models the signal intensity is inversely proportional to the square of the distance between the source and the detector. This changes when is closer closer to the source and one

must then use the full model for BDR. As can be seen on Fig. 3 the intensity per solid angle is constant at big distances and begins to oscillate at small distances. This means that the interference at near source distances depends not only on the angles, but on the distance also. And as shown on the 3 the interference effect can be considerable.

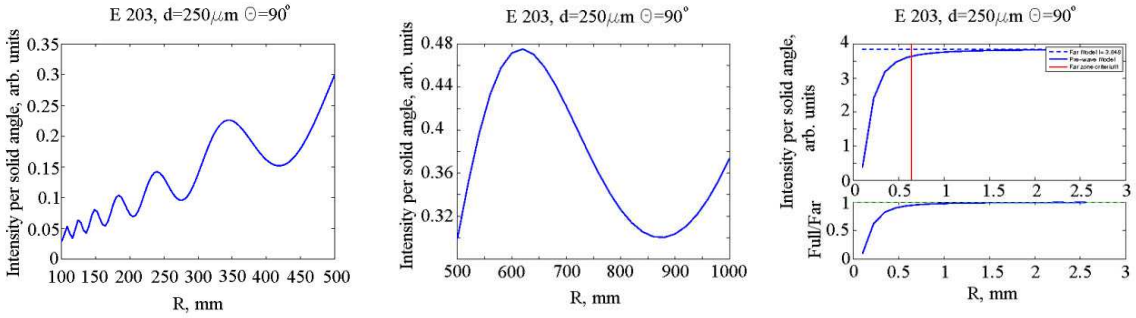

Figure 6: Dependence of the intensity from R

It is important to know if we should consider interference effects in our calculations or not, for this we have criterion for determining if we are in the far zone or not is Eq. 5. For easier understanding it could be visualized as curve in the two dimensional plot shown on Fig. 7, where ZY plane is $X_T Z_T$ on Fig. 1.

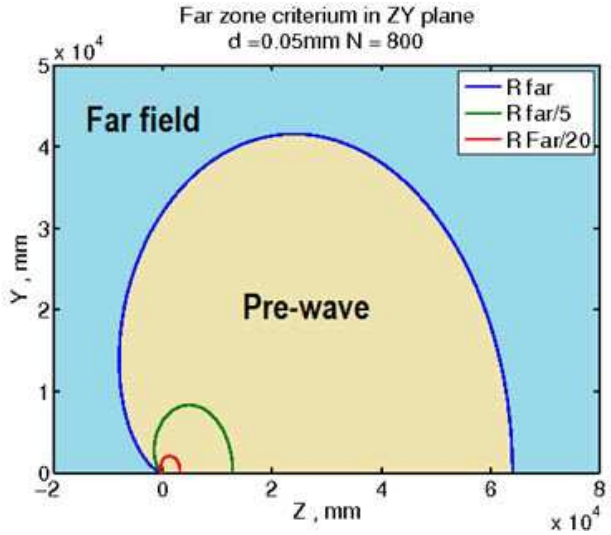

Figure 7: Far zone criterion

4 Summary

We have studied two important effect that can change the intensity of the Smith-Purcell Radiation and could thus affect its usability as a longitudinal profile monitor. We have compared the two leading models under experimental conditions and shown that it would not be possible

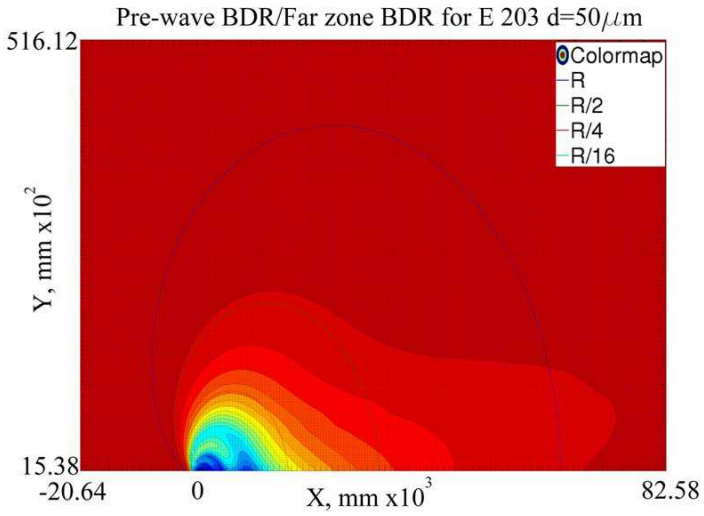

Figure 8: Intensity color map

to discriminate them experimentally. We have also shown that interferences in the near field zone have a significant effect and must be taken into account to estimate the correct intensity of SPR.

References

[1] S.J. Smith and E.M. Purcell, Phys. Rev. 92 (1953) 1069.

[2] H. Andrews et al., Nucl. Instr. Meth. A (2014) 212, Proceedings of the first European Advanced Accelerator Concepts Workshop 2013.

[3] D.V. Karlovets and A.P. Potylitsyn, Phys. Rev. ST Accel. Beams 9 (2006) 080701.

[4] D. Karlovets and A. Potylitsyn, JETP Letters 84 (2007) 489.

[5] V. Verzilov, Physics Letters A 273 (2000) 135.

[6] P. Karataev, Physics Letters A 345 (2005) 428.

Production and applications of parametric X-rays emitted by relativistic particles

A.V. Shchagin[a, b, c, 1], **I. Chaikovska**[c], **R. Chehab**[c]

[a] *Kharkiv Institute of Physics and Technology, Kharkiv 61108, Ukraine*
[b] *Belgorod State University, Belgorod 308015, Russia*
[c] *Laboratoire de l'Accelerateur Lineaire (LAL), Universite Paris-Sud, Bat. 200, 91898 Orsay, France*

Abstract: The nature of parametric X-ray radiation (PXR) excited by relativistic charged particles passing through a family of crystallographic planes is discussed. The PXR is a quasi-monochromatic radiation with energy smoothly tunable in the range from few to hundreds keV. The main properties of parametric X-ray radiation, like yield, angular distributions, spectral peak energy and polarization are considered. Some results of theoretical calculations and experimental research of the PXR properties are presented. Areas of PXR applications like as calibration of X-ray space telescopes by the PXR beam, obtaining of a shadow and phase-contrast images, control of electron beam parameters are described. Some possibilities for generation of secondary X-ray beams from crystals at ThomX in LAL are discussed.

PACS numbers: 41.60.-m, 61.80.Cb

Keywords: parametric X-ray radiation, virtual photons, crystal diffraction

November 27, 2015

1 Introduction

Parametric X-ray radiation (PXR) arises when a relativistic charged particle crosses a family of crystallographic planes in a crystal. M.L. Ter-Mikaelian devised a kinematic theory to describe this radiation in a classical approximation (see equations (28.157 - 28.160) in book [1] and also review [2]). Ter-Mikaelian named this radiation "resonant radiation" [1], but in the later literature the term "parametric X-ray radiation" (PXR) is used by an analogy to optical parametric Cherenkov radiation [3] which occurs when a charged particle crosses a medium consisting of periodically ordered layers with different dielectric constants. The results of classical calculations [1] were confirmed by quantum calculations performed by H. Nitta [4]. The fact that the kinematic theory can describe the basic properties of PXR emitted at large angles to the incident particle velocity vector is also confirmed by many experiments (see, for example, reviews [5, 6, 7, 8, 9] of such research). Let us note that, unlike conventional Cherenkov radiation, PXR is emitted if the particle velocity is less than the phase velocity of the radiation propagation in the crystal. Below, we will consider some of main properties of the PXR, mainly following to Ref. [9], where the kinematic theory of the PXR has been developed with use of Fresnel coefficients, and also discuss some applications of the PXR.

[1]Corresponding author: shchagin@kipt.kharkov.ua

2 The origin of the PXR

The emission of the PXR can be considered as a transformation of virtual photons accompanying a relativistic charged particle. The transformation occurs due to interaction of the field of relativistic particle with a periodically arranged family of crystallographic planes in a crystal. As a result, the so-called PXR reflection is emitted from the crystal. The PXR reflection is emitted around of the Bragg direction relative to incident beam of particles. Typical diagram of generation of the PXR reflection is given in Fig. 1.

Let us examine some properties of virtual photons that are associated with a charged particle which travels through a medium with constant velocity $\vec{V}$ and Lorentz factor $\gamma \gg 1$, where

$$\gamma = \frac{1}{\sqrt{1 - \left(\frac{V}{c}\right)^2}}, \qquad V = \left|\vec{V}\right|, \tag{1}$$

The angular distribution J_v of normalized spectral density of virtual photons associated with a charged particle moving in a medium can be described by the formula (1.24) in book [10]. In the approximation of small angular deviations from the direction of the particle velocity $\vec{V}$ and in the conditions $\gamma \gg 1$, $\hbar\omega \ll \gamma \cdot mc^2$, where m is the particle mass, the formula for angular distribution J_v has the form (see formula (4) in paper [11])

$$J_v = \left(\frac{dN_v}{d\Omega \frac{d\omega}{\omega}}\right)_{\perp} = \frac{\alpha \cdot z^2}{\pi^2} \frac{\delta_{v\perp}^2 + \delta_{v\parallel}^2}{\left(\gamma_{eff}^{-2} + \delta_{v\perp}^2 + \delta_{v\parallel}^2\right)^2}, \tag{2}$$

where dN_v is the number of virtual photons in the solid angle $d\Omega$; $\alpha = \frac{e^2}{\hbar \cdot c} \approx \frac{1}{137}$ is the fine-structure constant, z is the particle charge in units of the electron charge $-e$; $\hbar$ is the Planck constant, $\delta_{v\perp}$, $\delta_{v\parallel} \ll 1$ are small angles between the direction of the radiation propagation and the direction of the particle velocity $\vec{V}$ in arbitrarily chosen perpendicular directions, $\sqrt{\delta_{v\perp}^2 + \delta_{v\parallel}^2}$ is the angle between the vector $\vec{V}$ and the direction of the radiation propagation, $\gamma_{eff} = \left(\gamma^{-2} + |\chi_0|\right)^{-\frac{1}{2}}$ is the effective relativistic factor [12] with due regard for Ter-Mikaelian longitudinal density effect [1] (further, the density effect), χ_0 is the dielectric susceptibility for the radiation frequency ω higher than the frequencies of the atomic transitions and off the resonance frequencies, $|\chi_0| = 1 - \varepsilon = \left(\frac{\omega_p}{\omega}\right)^2$, where ε is the mean dielectric constant, and ω_p is the plasma frequency of the medium. Let us also note that the phase velocity of the X-ray propagation in the medium is usually higher than the speed of light, $\frac{c}{\sqrt{\varepsilon}} > c$, because $\varepsilon < 1$.

One can see from expression (2) that the virtual photons are symmetrically distributed around the velocity vector of the particle $\vec{V}$. The maximum of the distribution is resided at the angle γ_{eff}^{-1} to the particle's velocity vector $\vec{V}$, and there is a dip in the center of the distribution. The diagrams of the angular distributions of virtual photons are shown in Fig. 1. The spectral distribution of virtual photons does not have any peculiarities. One can see from formula(2) that the number of virtual photons propagating in any direction per unit frequency interval monotonically decreases as the frequency increases, $\frac{dN_v}{d\Omega d\omega} \sim \frac{1}{\omega}$.

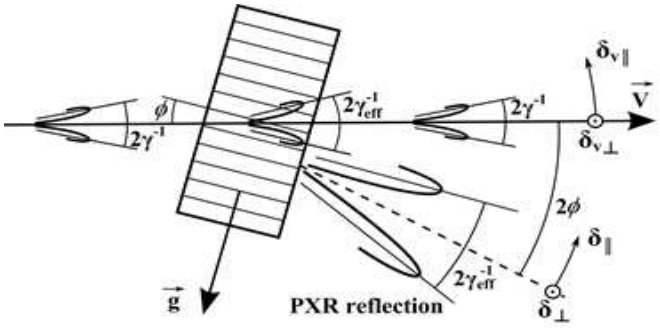

Figure 1: Typical schematic of PXR reflection generation, shown in the diffraction plane. A charged particle moves with the constant velocity $\vec{V}$ in vacuum and crosses the crystalline plate. Angular coordinates $\delta_{v\perp}$, $\delta_{\perp}$, which are measured in the directions perpendicular to this plane, are marked by circles with dots. One of the crystallographic planes of the crystal with a nonzero structure factor, shown by the dashed line, is characterized by the reciprocal lattice vector $\vec{g}$. Angular distributions for the number of virtual photons of the particle in a stationary state are depicted by diagrams at different sections of the particle trajectory: distribution in the crystal with a maximal number of virtual photons at angles $\delta_{v\perp}$, $\delta_{v\parallel} = \pm\gamma_{eff}^{-1}$, and distribution in the vacuum, before the particle enters and after it leaves the crystal, with the quantity γ^{-1} instead of γ_{eff}^{-1} and a maximal number of virtual photons at angles $\delta_{v\perp}$, $\delta_{v\parallel} = \pm\gamma^{-1}$; ϕ is the angle between the crystallographic planes and the vector $\vec{V}$. The PXR reflection is emitted at the angle 2ϕ to the vector $\vec{V}$. Angular distribution for the yield of the real photons in PXR reflection [17] is shown by the diagram; the maximal yield in the PXR reflection is found in the directions at the angles $\delta_{\perp}$, $\delta_{\parallel} = \pm\gamma_{eff}^{-1}$ to the direction of the PXR reflection center (Bragg direction), shown by the dashed line.

3 The PXR yield

Considering the reflection of the virtual photons (2) from the crystal, one can find the formula for the differential (with respect to the angles) yield of PXR [9, 11]

$$Y_{PXR} = \frac{dN_{PXR}}{d\Omega} = \frac{\alpha \cdot z^2 \cdot M \cdot \left|\chi_g\left(\omega_{PXR}\right)\right|^2}{\left(\frac{c}{V\sqrt{\varepsilon}} - \cos\theta\right)^2} \frac{\delta_{\perp}^2 + \delta_{\parallel}^2 \cdot \cos^2 2\phi}{\left(\gamma_{eff}^{-2} + \delta_{\perp}^2 + \delta_{\parallel}^2\right)^2}, \tag{3}$$

where $\delta_{\perp}$, $\delta_{\parallel} \ll 1$ are the small angles that define the direction of the radiation propagation with respect to the direction of the PXR reflection center (Bragg direction). The angles $\delta_{\perp}$, $\delta_{\parallel}$ are measured in the directions perpendicular and parallel to the PXR diffraction plane, respectively. The PXR diffraction plane goes through the vectors $\vec{V}$ and $\vec{g}$. The angle between the velocity vector of the particles $\vec{V}$ and the PXR reflection center equals 2ϕ in the diffraction plane, $\theta = 2\phi - \delta_{\parallel}$, and M is the number of crystallographic planes which contribute to the formation of PXR reflection. In a crystal which is transparent at frequency ω_{PXR}, M is simply the number of crystallographic planes crossed by the moving particle. In the case of an absorbing crystal, M decreases due to the attenuation of the radiation in the crystal. The effective number of crystallographic planes which contribute to the formation of PXR reflection in this case can be found using Eqs. (13), (14) in paper [13]: The expression for

radiation frequency ω_{PXR} is described below by eq. (4). Diagrams for angular distributions of the virtual photos accompanying the relativistic charged particle in the vacuum, and in the crystal, and of real photons in the PXR reflection are shown in Fig. 1. The formula (3) has been obtained in kinematical approximation without account of secondary reflections of emitted radiation from crystallographic planes. Experimental research of the PXR differential yield and confirmation of the validity of kinematic PXR theory can be found, e.g. in papers [5, 6, 9, 12, 13, 14, 15, 16, 17, 18, 19]. Calculations of the distribution of the PXR yield in the PXR reflections emitted at different angles can be found in refs [20, 21].

The absolute differential yield in the maxima of the PXR reflection observed in experiments with a thin silicon crystal, is, for example, on the order of $2 \cdot 10^{-4}$ quanta per electron per sr at an electron energy of 25.7 MeV [12], and on the order of $5 \cdot 10^{-3}$ quanta per electron per sr at an electron energy of 855 MeV [15].

4 Frequency of the PXR spectral peak

The PXR is quasi-monochromatic radiation. The frequency ω_{PXR} of the PXR first-order spectral peak is described by the formula

$$\omega_{PXR} = \frac{g \cdot V \cdot \sin\phi}{1 - \frac{V\sqrt{\varepsilon}}{c}\cos\theta} \tag{4}$$

Expression (4) was first derived in monograph [1] (see Eqs. (28.6) and (28.158) in [1]) from the energy and momentum conservation laws. Moreover, frequency (4) can be obtained from the Huygens scheme for PXR, proposed in book [5]. One of the remarkable properties of PXR lies with the ability to gradually tune the frequency of the PXR spectral peak by simply rotating the crystal target placed in a beam of accelerated particles, i.e. correspondingly changing the angle ϕ in formula (4). Gradual tuning of the PXR spectral peak frequency has been observed in various experiments in the energy range of PXR quanta from several keV [12, 14] up to 400 keV [22]. The measurements in cited articles experimentally confirmed the validity of expression (4).

5 The PXR spectral peak width

The normalized FWHM (full width at half of maximum) of the PXR spectral peak is

$$\frac{\Delta\omega}{\omega_{PXR}} = 0.89 \cdot M^{-1}. \tag{5}$$

This formula was obtained in Ref. [23], where PXR emitted from a finite transparent crystal was simply considered as a constant amplitude wave train. The number of oscillations in the train was equal to the number of crystallographic planes M which the particle crossed. Note that the expression for the normalized FWHM of the PXR spectral peak (5) was obtained for ideal conditions, without taking into account the effects of particle multiple scattering in the crystal, the radiation attenuation in the crystal itself, or the experimental angular resolution. Therefore, expression (5) holds true only in the case of relatively thin transparent crystals and ideal angular resolution. Changing these conditions can lead to the broadening of the

PXR spectral peak. The influence of the real experimental angular resolution, the experiment geometry, and the radiation attenuation on the width of the PXR spectral peak was studied in Refs. [14, 24], and the influence of particle multiple scattering was looked at in paper [25].

The normalized FWHM of the PXR spectral peak in experiments with a thin crystal is typically of the order of 10^{-2} [14], and a minimal normalized width of up to 10^{-9} can be obtained by generating focused PXR from a particle moving in a channeling regime through a long bent crystal [26] (see also Ref. [20]). In this case, the length of the PXR wave train and coherent length can reach huge as for X-rays values of several centimeters [26].

6 Linear polarization of the PXR

The differential yield of the PXR is completely linearly polarized. But the directions of linear polarization are different in different parts of the PXR reflection. The polarization structure of the PXR reflection is described by curves that are tangent to the directions of linear polarization in every point. The curves can be represented by the equation

$$\delta_{\perp} = B \cdot \left|\delta_{\parallel}\right|^{-\frac{1}{\cos(2\phi)}} \tag{6}$$

with arbitrary constant B. There is a significant difference in the structures of the linear polarization (6) in the PXR reflections emitted in the front and rear hemispheres. In the case of PXR reflection emitted in the front hemisphere for $2\phi < \frac{\pi}{2}$, curves (6), which are tangent to the directions of the linear polarization, have a hyperbolic form, while in the case of emission in the rear hemisphere, $2\phi > \frac{\pi}{2}$, these curves are parabolic. The calculated results for the structure of the linear polarization in PXR reflections emitted at various angles in the front and rear hemispheres are present in Fig. 2 in paper [27], as well as in figures plotted in papers [20, 21]. The calculated results are in good agreement with the results of the lab measurements of the PXR polarization performed by in Ref. [28].

7 Applications of the PXR

The PXR is a beam of linearly polarized monochromatic X-ray radiation. The PXR photon energies can be smoothly tuned in the range from a few to hundreds of keV. However, the sources of synchrotron or Compton backscattering radiation can be more powerful because of multiple emission of radiation by every electron that move in a storage ring. But PXR source can be easy installed at any linear accelerator without a storage ring and PXR reflection can be emitted at big angle to the electron beam. Besides, the PXR source can provide soft monochromatic tunable gamma-ray beam with energy of photons up to hundreds of keVs. Let us describe briefly some of possible applications of the PXR.

The experiment [22] demonstrated that PXR can provide beam with photon energies no less than 400 keV. This fact encouraged research for application of the PXR for calibration of hard X-ray or soft gamma-ray space telescopes. It was found in Ref. [29, 30] that PXR source can provide enough for calibration flux of monochromatic linearly polarized radiation at distance about 500 m with photon energies of hundreds keV. The distance is necessary to provide low enough divergence for whole telescope's aperture.

Crystals have a number of crystallographic planes. The PXR reflections are produced in every of them. Therefore a number of PXR reflections are emitted simultaneously and coherently in different directions from only one crystal installed in a particle beam. The application of such multi-beam generation for obtaining several coherent X-ray beams simultaneously has been proposed in [29].

The PXR beam with photon energy exceeding K-edges of elements U and Pu can provide K-shell ionization of these atoms. Observation of K-lines of characteristic X-ray radiation would allow identification of these elements. Possibilities of the X-ray locator based on the PXR source to control nuclear materials nonproliferation was analyzed in Refs. [31, 32]. It was found that the remote location of nuclear materials is possible up to distances up to about 20 m.

There were experiments for observation of shadow images of biological objects with use of the PXR beam [33, 34, 35]. More recently, phase-contrast images in the PXR beam were obtained [36].

Since pioneering work [37], a series of experimental research about increasing of positrons production in crystalline targets were performed, see e. g. [38, 39, 40]. The control of the production of coherent bremsstrahlung and positrons from a crystalline target by PXR emitted from the same target in backward direction has been proposed and considered in Ref. [41].

Possibilities for optical diagnostics of small intensive beams are restricted because of diffraction limitations and coherent emission from dense beams. In order to overcome these limitations, application of X-ray diagnostics based on PXR source has been proposed in Refs. [42, 43]. Recently, observation of the beam profile with use of the PXR source with pinhole has been demonstrated in experiment [44].

In Ref. [45], it was proposed and analyzed the possibility for measurements of the size of crystalline grains of nanometers range with use of the spectral peak width of the PXR emitted in the backward direction.

Emission of wide PXR beam from the textured polycrystal was demonstrated in experiments described in Refs. [46, 47]. Such wide PXR beam can be used for imaging of large objects [46, 48]. Besides, the application of rolled textured metal foils as a radiator of PXR would allow the increase of beam current and PXR beam power without problems connected with target damage.

The application of the PXR for online diagnostics of the interaction of the beam with bent crystal was proposed in [49]. The possibility to use PXR for control of the bent crystal degradation was analyzed [50]. Thus, PXR can be used for online control of bent crystalline deflectors of high-energy beams. Experiments with PXR began in CERN [51] and in Protvino [52].

Thus, there are a lot of fields for applications of the PXR. However, not all basic properties of the PXR are well known by now. For instance, properties of the PXR generated from bent crystal has been poorly studied by now, as well as coherent properties of the PXR beam.

8 Some possibilities for X-ray beam production based on radiation from crystals at ThomX in LAL

ThomX is a project proposed by a collaboration of French institutions and one company to build an accelerator based compact X-ray source in Orsay (France) [53, 54]. The main goal of the project is to deliver a stable and a high energy X-ray beam (up to ~ 90 keV) with a flux of

the orders of $10^{11} - 10^{13}$ photons per second generated by the Compton backscattering process. At present, the ThomX machine is under construction. The ThomX accelerator facility is composed by the linac driven by 2998 MHz RF gun, a transfer line and a compact storage ring where the collisions between laser pulses and relativistic electron bunches result in the production of the X-rays. The energy of accelerated electron beam would be 50 – 70 MeV. If there would be a possibility to install a goniometer under a vacuum on the electron beam, one can also provide another source of X-ray beam. A few kinds of radiation generated by electron beam passing through a crystal can be used, such as channeling radiation, coherent bremsstrahlung and PXR. This could extend the capabilities of the ThomX [55]. As for the PXR, the X-ray beam can be used as it was described in previous section as well as for basic research.

Acknowledgments

This paper became possible due to supports from International Associated Laboratory on the field of high energy physics "Instrumentation Developments for Experiments at Accelerators facilities and accelerating Techniques" (LIA IDEATE), and LAL, and also due to travel financial support from the STCU.

References

[1] Ter-Mikaelian M. L. High-Energy Electromagnetic Processes in Condensed Media (New York: Wiley-Interscience, 1972)

[2] Ter-Mikaelian M. L. Phys. Usp. 44 571 (2001)

[3] Fainberg Ya. B., Khizhnyak N. A. Sov. Phys. JETP 5 720 (1957)

[4] Nitta H. Phys. Lett. A 158 270 (1991)

[5] Shchagin A. V., Maruyama X. K., in Accelerator-Based Atomic Physics: Techniques and Applications (Eds. S. M. Shafroth, J. C. Austin) (New York: AIP Press, 1997) p. 279

[6] Potylitsyn A. P. Electromagnetic Radiation of Electrons in Periodic Structures (Heidelberg: Springer, 2011)

[7] Rullhusen P., Artru X., Dhez P. Novel radiation sources using relativistic electrons (Singapore, World Scientific, 1998) 143160.

[8] Baryshevsky V. G., Feranchuk I. D., Ulyanenkov A P Parametric x-ray radiation in crystals: Theory, experiment and applications (No. 213) (Springer Science & Business Media, 2005)

[9] Shchagin A. V. Fresnel coefficients for parametric X-ray (Cherenkov) radiation, Physics - Uspekhi 58 819 - 827 (2015)

[10] Bazylev V. A., Zhevago N. K. Radiation of Fast Particles in Medium and in External Fields) (Moscow: Nauka, 1987)

[11] Shchagin A. V. Radiation Phys. Chem. 61 283 (2001)

[12] Shchagin A. V., Khizhnyak N. A. Nucl. Instrum. Meth. Phys. Res. B 119 115 (1996)

[13] Shchagin A. V., Takabayashi Y. Nucl. Instrum. Meth. Phys. Res. B 309 198 (2013)

[14] Shchagin A. V., Pristupa V. I., Khizhnyak N. A. Phys. Lett. A 148 485 (1990)

[15] Brenzinger K.-H. et al. Z. Phys. A 358 107 (1997)

[16] Takabayashi Y., Shchagin A. V. Nucl. Instrum. Meth. Phys. Res. B 278 78 (2012)

[17] Shchagin A. V., Pristupa V. I., Khizhnyak N. A. Nucl. Instrum. Meth. Phys. Res. B 99 277 (1995)

[18] Sones B., Danon Y., Block R. C. Nucl. Instrum. Meth. Phys. Res. B 227 22 (2005)

[19] Fiorito R. B. et al. Phys. Rev. E 51 R2759 (1995)

[20] Shchagin A. V. in: Advanced Radiation Sources and Applications (NATO Science Series, Ser. II, Vol. 199, Ed. H Wiedemann) (Dordrecht: Springer, 2006) p. 27

[21] Shchagin A. V., Sotnikov V. V. Voprosy Atom. Nauki Tekh. Ser. Plazmennaya Elektron. Novye Metody Uskoreniya (4(6)) 316 (2008)

[22] Morokhovskii V. L., Shchagin A. V. Sov. Phys. Tech. Phys. 35 623 (1990)

[23] Shchagin A. V. J. Phys. Conf. Ser. 236 012020 (2010)

[24] Brenzinger K.-H. et al. Phys. Rev. Lett. 79 2462 (1997)

[25] Shul'ga N. F., Tabrizi M. JETP Lett. 76 279 (2002)

[26] Shchagin A. V. JETP Lett. 80 469 (2004)

[27] Shchagin A. V. Phys. Lett. A 247 27 (1998)

[28] Morokhovskii V. V. et al. Phys. Rev. Lett. 79 4389 (1997)

[29] Shchagin A. V., Khizhnyak N. A., Fiorito R. B., Rule D. W., Artru X. Nucl. Instrum. Meth. Phys. Res. B 173 154 (2001)

[30] Shchagin A. V., Sanin V. M., Sotnikov V. V., Voronko V. A. Problems of Atomic Science and Technology, Series "Nuclear Physics Investigations" 42(1) 187 (2004)

[31] Shchagin A. V., Sanin V. M., Sotnikov V. V., Voronko V. A., Yegorov A. M. Problems of Atomic Science and Technology, Series "Nuclear Physics Investigations" 42(1) 194 (2004)

[32] Shchagin A. V., Sanin V. M., Sotnikov V. V., Voronko V. A., Yegorov A. M. Problems of Atomic Science and Technology. Series: Plasma Physics, 1(10) 203 (2005)

[33] Hayakawa Y., et al. in: Proceedings of the 1st Annual Meeting of Particle Accelerator Society of Japan and the 29th Linear Accelerator Meeting in Japan, 2004

[34] Sones B., Danon Y., Block R. in: Proceedings of ANS Annual Meeting, 2004.

[35] Piestrup M. A., Wu X., Kaplan V. V., Uglov S. R., Cremer J. T., Rule D. W., Fiorito R. B. Rev. Sci. Instr. 72 2159 (2001)

[36] Hayakawa Y. et al. JINST 8 C08001 (2013)

[37] Chehab R., Couchot F., Nyaiesh A. R., Richard F., Artru X., in: Proceedings of the 1989 IEEE Particle Accelerator Conference (PAC89), Chicago, IL, USA, p. 283 (1989)

[38] Artru et al., Nucl. Instrum. Meth. Phys. Res. B 119 246 (1996)

[39] Chehab R. et al., Phys. Lett. B 525 41 (2002)

[40] Artru X, Chaikovska I, Chehab R, Chevallier M, Dadoun O, Furukawa K, Guler H, Kamitani T, Miyahara F, Satoh M, Sievers P, Suwada T, Umemori K, Variola A Nucl. Instrum. Meth. Phys. Res. B 355 60 (2015)

[41] Shchagin A. V. Nuovo Cimento C 34 181 (2011)

[42] Gogolev A., Potylitsyn A., Kube G. J. Phys.: Conf. Ser. 357 012018 (2012)

[43] Takabayashi Y. Phys. Lett. A 376 2408 (2012)

[44] Takabayashi Y., Sumitani K. Phys. Lett. A 377 2577 (2013)

[45] Shchagin A. V. J. Phys.: Conf. Ser 236 012020 (2010)

[46] Takabayashi T., Endo I., Weda K., Moriyoshi C., Shchagin A. V. Nucl. Instrum. Meth. Phys. Res. B 243 453 (2006)

[47] Nawang S. et al., Journal of the Physical Society of Japan 75 124705 (2006)

[48] Lobach I., Benediktovitch A., Feranchuk I., Lobko A. Nucl. Instrum. Meth. Phys. Res. B 360 75 (2015)

[49] Shchagin A. V., J. Kharkiv Univ., Phys. Ser. "Nuclei, Particles Fields" 30 35 (2006)

[50] Gogolev A. S., Potylitsyn A. P., Taratin A. M., Tropin Yu.S., Nucl. Instrum. Methods B 266 3876 (2008)

[51] Scandale W. et al. Phys. Lett. B 701 180 (2011)

[52] Afonin A. G., Britvich G. I., Chesnokov Yu. A., Chirkov P. N., Durum A. A., Kostin M. Yu., Lutchev A. V., Maisheev V. A., Yanovich A. A., Shchagin A. V., Truten' V. I., Ganenko V. B., Kirillin I. V., Shul'ga N. F., Kubankin A. S., Nasonov N. N., Potylitsyn A. P., Gogolev A. S., Uglov S. R., Cherepennikov Yu. M., Karataev P. Problems of Atomic Science and Technology, Series "Plasma electronics and new methods of acceleration" 4(86) 315 (2013)

[53] "ThomX Conceptual Design Report" (Eds. Variola A., Loulergue A., Zomer F.), LAL RT 9, 28 (2010)

[54] "ThomX Technical Design Report" (Eds. Variola A., Haissinski J., Loulergue A., Zomer F.) LAL RT 14-21 SOLEIL/SOU-RA-3629 (2014)

[55] Chaikovska I., Chehab R., Shchagin A., A versatile x-ray source based on electromagnetic radiation from moderately energetic electrons, Note DEPACC #2015-001, LAL, Orsay, le 2 dcembre 2015

Hybrid and Metal Microdetector Systems for measuring in real time spatial distribution of charged particles and X-rays beams

V. Pugatch[a], I. Momot[a], O. Kovalchuk[a], O. Okhrimenko[a], Y. Prezado[b]

[a] *Institute for Nuclear Research, National Academy of Sciences of Ukraine, Kyiv*
[b] *Laboratoire d'Imagerie et Modélisation en Neurobiologie et Cancérologie (IMNC, CNRS), Orsay*

Abstract: Metal and hybrid micro-detector systems were tested at experimental facilities (HERA-B, LHCb, ESRF, KINR Tandem-generator) for measuring and imaging in real time spatial distribution of charged particles as well as X-ray beams. Monte-Carlo simulations as well as tests with low energy proton beam indicate a possibility to provide shaping and monitoring in real time of mini-beam structures for the purposes of fractionated hadron radiation therapy.

PACS numbers: 29.40.Wk

Keywords: Monitoring of the charged particles and X-ray beams, Metal and hybrid micro-detectors, Real time systems.

1 Introduction

Various applications of the ionizing radiation beams require precise, long term reliable monitoring of their spatial distribution in real time. In particular, the tissue-sparing effect of spatially fractionated beams was established in biological studies performed with mini-, micro-beams of synchrotron radiation [1, 2]. The concept of hadrons minibeam radiation therapy has been proposed as well [3]. Homogeneous distribution of the dose delivered by every beam as well as the highest possible Peak-to-Valley-Dose-Ratio (PVDR) for all beams in a multi-beam structure are required for reaching the best therapeutic result. To measure the dose profiles Gafchromic films are usually explored in conventional radiotherapy [4]. Their off-line analysis provides excellent position accuracy (few micrometers) of the dose distribution. Yet, it is a time consuming procedure and it is impossible to have an online dose monitoring.

In this talk the application of metal and hybrid micro-detector systems operating in real time is briefly presented for the X-rays beams monitoring while more detailed results are discussed for measuring charged particles beams also in multi-beam structures shaped by slit or matrix collimators. Studies were performed with prototypes of such systems exploring low energy protons at the KINR Tandem generator.

2 Experimental studies

2.1 Metal Foil Detectors at high energy hadron beams

Physics and techniques principles of the Metal Foil Detector (MFD) have been developed at the Institute for Nuclear Research NASU (Kiev, KINR) [5]. Incident on a metal foil sensor

particles result in Secondary Electron Emission (SEE) from 10-50 nm of its surface. A positive charge appearing at isolated sensor is measured by sensitive Charge Integrator. A single layer MFD had been explored for the multi-target steering at the HERA-B experiment [6]. To provide unambiguous reconstruction of secondary vertices the interaction rate of 40 MHz had to be equally distributed over eight targets operated simultaneously in the halo of the 920 GeV proton beam. This has been realized by making targets as an MFD structure thin metal strips connected to sensitive charge integrators. It has been proved that the SEE yield under the protons impinging onto a single target was strictly proportional to that target partial contribution into the total interaction rate. The equal sharing ($\sim 12,5\%$) of the overall luminosity among eight operating metal targets-detectors has been demonstrated by means of the reconstructed primary vertices.

The 12 sector MFD has been built and explored for the luminosity monitoring of the experiment HERA-B. The reliably detected flux of relativistic particles was in the range of 10^4 particles/s per MFD sensor. Based on this technology Radiation Monitoring System (RMS) [7] has been built at the Large Hadron Collider for the LHCb experiment for monitoring of the radiation load on the Silicon Tracker sensors.

2.2 Metal and Hybrid Micro-Detectors at X rays beams

A reliable performance of the Metal Foil Detectors mentioned above as well growing demand for the low mass, radiation hard micro-detectors have evolved into the development of the Metal Micro-strip and Micro-pixel detectors (MMD). Such detectors have been successfully created at KINR in close collaboration with MPIfK (Heidelberg), DESY (Hamburg), Institute of Microdevices NASU (Kiev) and CERN (Geneva) [8, 9, 10]. To achieve the micrometer level position resolution and low thickness the silicon micro-strip detector technology combined with plasma-chemistry etching has been developed and used for the MMD design and production [8, 9]. Current technology allows for production of the $\sim$ 2 m thick metal strip sensors with width and pitch at the level of few micrometers. The sensitivity of the MMD to the radiation flux is determined by the physics conversion factor as well as by the readout electronics. For instance, the MMD successfully applied for the 13 keV X-rays beam profile monitoring at HASYLAB (DESY, Hamburg) has had the conversion factor of 1.5×10^4 photons/electron [9].

Characterization studies of the Metal Micro-detectors have been performed at the Minibeam Radiation Therapy (MBRT) setup at ESRF (Grenoble) measuring in real time dose distribution of the synchrotron radiation [11]. The biomedical features of that therapy requires high doses up to several kGy/sec. X-rays with peak energy ranging from 50 to 600 keV (peak energy of 100 keV) were produced with intensity up to 5×10^{11} photons/(c $\times$ mm^2). The spatially fractionated minibeam patterns were produced by multi slit collimator or utilizing a rotating chopper. Existing position sensitive gaseous or solid state detectors cannot operate reliably in real time at high radiation load exploited for the MBRT.

TimePix detector designed at CERN [12] has been used in these studies in a metal or hybrid mode for real time measurement of the dose distribution. TimePix detector in a metal mode comprises a bare readout microchip (256×256 pixels) and a metal grid for collecting SEE. Each readout pixel has a size of (55×55) μm^2. High spatial resolution as well as radiation hardness of the TimePix (up to 4.6 MGy) are suitable for measuring steep dose gradient areas and PVDR. The results obtained have demonstrated reliable performance of the TimePix in real time measurements at the radiation load of few kGy/s distributed over 10 beam-prints

with a size of each 0.6×10 mm^2 and center-to-center distance of 1.2 mm. PVDR measured by the TimePix and gafhromic films agreed well.

Data obtained for various modifications of mini- as well as micro- beam configurations will be used for creating a novel MMD-based radiation hard monitoring system for radiation therapy applications. In comparison with the latest developments in beam profile monitoring by various detector systems Metal Micro-strip Detectors have an advantage of being extremely thin and semi-transparent device, providing nearly non-destructive beam analysis in real time.

TimePix detector in a hybrid mode has been also applied for the X-rays diffraction studies of a dynamics of phase transitions in metal alloys under heating/cooling at the experimental setup of the Institute for Problems in Material Science NASU (Kiev) [13]. Metal samples under heating/cooling transform their crystal structure resulting in a shift of corresponding diffraction peaks of scattered X-rays. TimePix detector allowed to get precise data on peaks position and their evolution in real time exploring fast framing rate of up to 100 Hz with the USB interface FitPix [14]. This is a key feature for dynamical phase transition studies. One may treat the TimePix detector as an electronic plate imaging in real time a dynamics of phase transitions.

2.3 Hybrid and Metal micropixel detectors measuring spatial distribution of low energy ions in a focal plane of the mass-spectrometer

The TimePix (Hybrid and Metal) detector response to low energy ions has been studied as a function of ion mass, charge, energy and beam position observed at the focal plane of the laser mass-spectrometer of the Institute of Applied Physics (Sumy, Ukraine) [15]. Ion beams have been generated at the sample-target by the pulsed infrared (1064 nm) laser. Position of the TimePix detector alongside the focal plane, accelerating voltage and magnetic field were adjusted to observe few tens keV positively charged ions of the different isotopes (from carbon to lead). Real time observation of the mass-distribution of isotopes has proved usability of the TimePix detector for tuning and adjusting mass-spectrometer. This provides an improvement in a mass-resolution as well as introduces a new possibility of a simultaneous mass-spectrometry of few target samples, prepared, for instance, by different technologies. It was established that pixels response is more uniform for the TimePix (Metal) mode operation. Results of the tests show the ability of both detector modes to be used for building electronic focal plane of the mass-spectrometer to determine the chemical composition of a complex target samples. Mapping isotope population over the sample area by scanning it by a laser or charged particle micro-beam might be useful for applications in material studies, microbiology, medical diagnostics etc.

2.4 Feasibility studies of Metal and Hybrid microdetectors for Monitoring of the Hadron Beams for the purposes of fractionated radiation therapy

Spatially fractionated hadron beams (several hundred MeV/nucleon) are considered as promising tool to get better therapeutic results due to dose localization, and tissue-sparing effect observed with mini-beams of synchrotron radiation [3]. We report here some results of the experiment performed for optimization of the characteristics of the setup for carrying out feasibility studies at Heidelberger Ionenstrahl-Therapiezentrum (HIT, Heidelberg) related to the

design of collimators and their effectiveness for the purposes of the fractionated mini-beam hadron radiation therapy. Monte Carlo simulations (Gate_v.6.2 and Geant4 versions) of dose distribution resulting from spatially fractionated irradiations have been explored for the design of collimators shaping multi-beam structure. As figure of merit, peak and valley depth dose curves, penumbras, and central Peak-to-Valley Dose Ratios (PVDR) have been calculated for various collimators, incident ions and their energies.

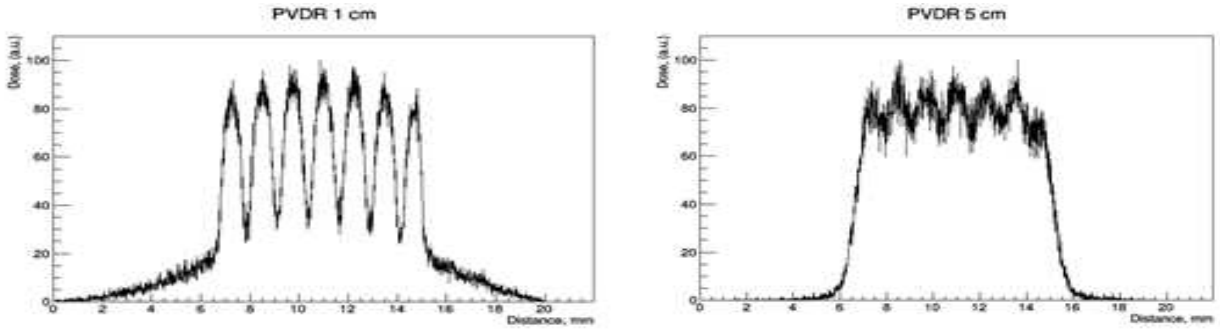

Figure 1: Monte-Carlo simulation of the dose profile (projection onto X-axis) from the 7×7 holes with diameter of 0.6 mm in matrix aluminum collimator with c-t-c distance of 1.2 mm. Protons energy: 87 MeV. Left: depth in a water phantom – 1 cm. Right – 5 cm.

An example of such calculations is shown in Fig. 1 presenting Monte-Carlo simulation of the dose profile expected at different depth in a water phantom irradiated by the 87 MeV proton multi-beam structure, shaped by the matrix aluminum collimator (7×7 holes with diameter of 0.6 mm and c-t-c distance of 1.2 mm). One may see clear separation of the beams (projection onto X-axis) at the depth of 1 cm (left part of the Fig. 1) with PVDR value about 5, while at the depth of 5 cm the fractionation of the beam becomes negligible (due to scattering of protons on their way through phantom). This means that the normal tissue would benefit from the spatial fractionation of the dose while a quasi-homogeneous dose distribution is achieved in the tumor position. It is clear that 1D- or 2D-scanning by the hadron pencil beam [15] over the tumor area would provide the best result, keeping in mind, otherwise, an additional radiation load on patient from the irradiated collimator. It is the task for the further bio-medical studies to find out the best therapeutic approach in shaping the multi-beam structure and evolution of the fractionation over the depth of tissue. One could assume that it might be in providing well separated beams on the way through the healthy tissue and making them merged in a tumor.

Test of the prototypes of the experimental setup for shaping and monitoring of the hadron beam for the purposes of the fractionated radiation therapy has been performed at the KINR Tandem generator.

Protons with the energy of 3 MeV were incident on the polyethylene target installed inside the reaction chamber (Fig. 2). For shaping multi-beam structure from the scattered protons collimators of two types were explored, slit and matrix. Both were manufactured out of 2 mm thick Al plates: SLIT - with 5 slits; MATRIX with $5 \times 5 = 25$ holes, covering active area of 14×14 mm^2 of the TimePix detector. Protons scattered by the target were registered by two TimePix detectors installed at 100 mm ddistance from the target center, at 45 degrees from both sides of the proton beam axis. One of the detectors was operated in a metal mode while another one in a hybrid mode with 300 μm thick silicon micropixel sensor. As an example Fig. 3

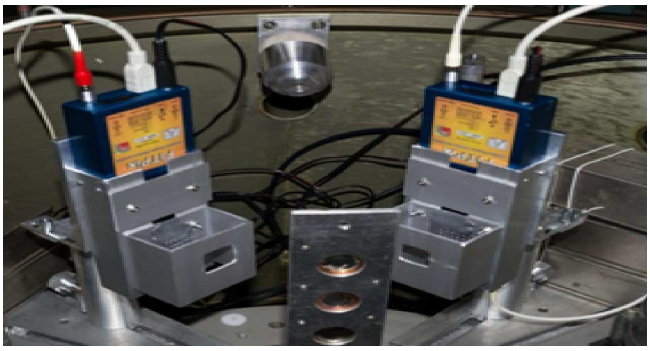

Figure 2: Photo of the reaction chamber at the KINR Tandem generator. Two TimePix detectors and matrix collimators in front of them were mounted inside of the chamber.

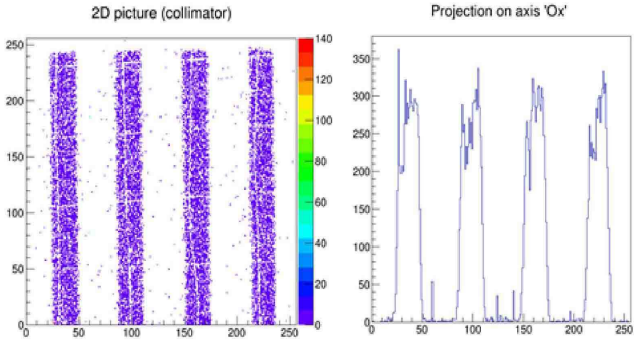

Figure 3: Left: 2D distribution of the of the direct proton beam intensity (color scale at the right side) measured by metal TimePix detector (X- and Y-axis – pixel number). Slit collimator was installed in front of the TimePix. Right: Projection of the data onto X-axis.

illustrates 2D image of the protons intensity distribution measured by metal TimePix detector with the SLIT collimator installed in front of it. Perfectly separated 'beams' were observed. We point out in Fig. 3 (Left) vertical and horizontal narrow regions with zero intensity inside the slits area. Those regions correspond to the image of the grid (metal wires, 100 μm diameter) installed in close vicinity to the TimePix readout microchip for providing its metal mode of operation with positive 20 V applied. Projection of the 2D data onto X-axis also exhibits the drop of the intensity inside the slit area at position of the grid wires. This illustrates a nice performance of the TimePix detector in reflecting details of the 2D beam intensity distribution with an accuracy of 55 μm.

The results obtained with a MATRIX collimator installed at the entrance window of the detector TimePix are illustrated in Fig. 4.

The important feature of the multi-channel detecting system is the uniformity of its response. For testing this feature of the TimePix detector we have measured the angular distribution of the protons scattered by the carbon target within the TimePix acceptance ($41\,^\circ < \theta < 49\,^\circ$) and compared it with the corresponding calculations. From that study we have concluded that the tested sample of the TimePix detector had non-uniform response of its 65 536 pixels varying within +/– 15 %.

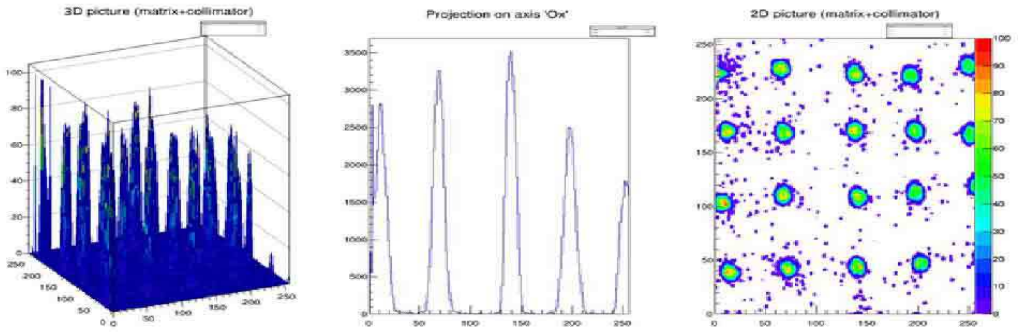

Figure 4: Right: 2D distribution of the of the scattered proton beam intensity (color scale at the right side) measured by hybrid TimePix detector (X- and Y-axis – pixel number) at 45 degrees. Matrix collimator was installed in front of the TimePix detector. Middle: Projection of the data onto X-axis. Left: 3D-view of the proton beam intensity distribution over the TimePix detector area.

3 Summary and Outlook

Metal and hybrid micro-detector systems tested at different experimental facilities for measuring spatial distribution of charged particles as well as X-rays beams have demonstrated reliable performance also in real time imaging of the measured data. The results obtained in frames of Monte-Carlo simulations as well as in the tests with low energy proton beam indicate a possibility to provide shaping and monitoring of mini-beam structures for the purposes of fractionated hadron radiation therapy. Based on these studies similar metal and hybrid micro-detector systems as well as slit and matrix collimators have been recently used in feasibility studies with high energy hadron beams at Heidelberger Ionenstrahl-Therapiezentrum (HIT, Heidelberg). We plan to publish their positive results, soon.

Acknowledgments

This research was partially conducted in the scope of the IDEATE International Associated Laboratory (LIA). We thank MEDIPIX Collaboration, in particular, M. Campbell, X. Llopart, S. Pospisil, C. Granja for introducing an opportunity to use TimePix detectors for these studies. We express our gratitude to the personnel of the KINR Tandem generator for providing stable beam and frank collaboration atmosphere. This work has been supported by the grants CO-4-1/2015 (NASU) and 58/382-2013 (DFFD).

References

[1] D. Slatkin, P. Spanne, F. A. Dilmanian, J.-O. Gebbers and J. A. Laissue, "Subacute neuropathological effects of microplanar beams of x-rays from a synchrotron wiggler", Proc. Natl. Acad. Sci. U.S.A. 92, 87838787 (1995).

[2] F.A. Dilmanian, T.M. Button, G. Le Duc, N. Zhong, L.A. Pena, J.A. Smith, S.R. Martinez, T. Bacarian, J. Tammam, B. Ren, P.M. Farmer, J. Kalef-Ezra, P.L. Micca, M.M.

Nawrocky, J.A. Niederer, F.P. Recksiek, A. Fuchs and E.M. Rosen, "Response of rat intracranial 9L gliosarcoma to microbeam radiation therapy", Neuro Oncol. 4, 2638 (2002).

[3] Y. Prezado and G. Fois, Proton-minibeam radiation therapy: a proof of concept, Med. Phys. 40, 031712-18 (2013).

[4] S. Devic, J. Seuntjens, E. Sham, E. B. Podgorsak, C. R. Schmidtlein, A. S. Kirov and C. G. Soares, "Precise radiochromic film dosimetry using flat-bed document scanner", Med. Phys. 32, 22452253 (2005).

[5] V. Pugatch et al., Metal foil detectors and their applications. Nucl. Instr. and Meth. A 535 (2004) 566569.

[6] V. Pugatch et al., Beam profile imaging target. Nuclear Physics. A701 (2002) 204-208

[7] V.M. Iakovenko, O.Y. Okhrimenko, V.M. Pugatch, S.Ya. Barsuk, M.-H. Schune. Selected physics measurements for the LHCb experiment and the radiation monitoring system. Nuclear Physics and Atomic Energy. 12 (2011) 221.

[8] V. Pugatch et al. Plasma technologies for manufacturing of micro-strip metal detectors. Voprosi atomnoi nauki i technki (in Russian). 1 (2007) 173-175.

[9] V. Pugatch. Position sensitive micro-strip and micro-pixel detectors. Science and Innovation. 8 (2012) 26-33.

[10] V. Pugatch et al. Micro-strip metal detector for the beam profile monitoring. Nucl. Instr. and Meth. A581 (2007) 531534.

[11] V. Pugatch, M. Campbell, A. Chaus, O. Kovalchuk, X. Llopart, O. Okhrimenko, S. Pospisil, Y. Prezado, M. Renier, L. Tlustos, "Metal Micro-detector TimePix imaging synchrotron radiation beams at the ESRF Bio-Medical Beamline ID17", Nucl. Instr. Meth. Phys. Res. A 682 (2012) 811.

[12] X. Llopart, R. Ballabriga, M. Campbell, L. Tlustos, W. Wong, Nucl. Instr. and Meth. A 581 (2007) 485

[13] M. V. Pugach, V. V. Burdin, M. Campbell, O. S. Kovalchuk, X. Llopart, . V. Minakov, V. M. Militsiya, . Yu. khrimenko, Yu. V. Podrezov, S. Pospisil, V. M. Pugatch, D. I. Storozhyk, L. Tlustos, S. O. Firstov, A. V. Chaus. Usage of the micropixel detector TimePix for observation of the dynamics of phase transitions in metals. Nuclear Physics and Atomic Energy. Vol. 13, #4 (2012) 382-386

[14] Z. Vykydal, J. Jakubek and S. Pospisil, "USB interface for Medipix2 matrix device enabling energy and position-sensitive detection of heavy charged particles", Nucl. Instr. Meth. Phys. Res. A 563 (2006) 112118

[15] V. Pugatch, M. Campbell, A. Chaus, V. Eremenko, S. Homenko, O. Kovalchuk, X. Llopart, O. Okhrimenko, S. Pospisil, A. Shelekhov, V. Storizhko, L. Tlustos. Metal and hybrid TimePix detectors imaging beams of particles. Nuclear Instruments and Methods in Physics Research A 650 (2011) 194197

[16] L. Grevillot, T. Frisson, N. Zahra, D. Bertrand, F. Stichelbaut, N. Freud, and D. Sarrut, "Optimization of GEANT4 settings for proton pencil beam scanning simulations using GATE", Nucl. Instrum. Methods Phys. Res. B 268, 32953305 (2010).

Studies of sensitive area for a single InGrid detector

A. Chaus[a,b], M.Titov[b], O.Bezshyyko[c], O.Fedorchuk[c]

[a] *Kyiv Institute for Nuclear Research*
[b] *CEA, Saclay*
[c] *Taras Shevchenko National University of Kyiv*

Abstract

The novel structures where Micromegas or GEM are directly coupled to the CMOS multi-pixel readout represent an exciting field and allow to reconstruct fine-granularity, two-dimensional images of physics events. One of such structures that has become subject of this article is a single InGrid detector. In order to study sensitive area of a single InGrid detector, an InGrid chip has been operated in Mini-TPC. Full simulation of experimental setup and electric field were performed. Experimental data were compared with simulation in several different configurations.

Keywords: Micromegas, InGrid, Gas detectors, TPC

1 Introduction

The availability of highly integrated amplification and readout electronics allows for the design of gas-detector systems with channel densities comparable to that of modern silicon detectors. The fine granularity and high-rate capability of GEM and Micromegas devices can be fully exploited by using high-density pixel readout with a size corresponding to the intrinsic width of the detected avalanche charge. However, for a pixel pitch of the order of 100 μm, technological constraints severely limit the maximum number of channels that can be brought to the external front-end electronics. While the standard approach to readout the signals is a segmented strip or pad-plane with front-end electronics attached through connectors from the backside, an attractive alternative is to place CMOS chip in the gas volume (without bump-bonded semiconductor sensor), with GEM or Micromegas amplification structure directly above it. With this arrangement signals are induced at the input gate of a charge-sensitive preamplifier (top metal layer of the CMOS chip). Every pixel is then directly connected to the amplification and digitization circuits, integrated in the underlying active layers of the CMOS technology. The proof-of-principle of this concept has been demonstrated in the past by several groups [1, 2, 3].

2 Pixel readout of Micro-Pattern Gas Detectors. The "InGrid" Concept

The original motivation of combining a Micro-Pattern Gas Detector (MPGD) with Medipix2 [4] and Timepix [5] chips was the development of a new readout system for a large TPC at the ILC. The digital Medipix2 chip was originally designed for single-photon counting by means of a semiconductor X-ray sensor coupled to the chip. In gas detector applications, the chip is placed in the gas volume without any semiconductor sensor, with a GEM or Micromegas

amplification structure above it [2, 3, 6]. Approximately 75 % of each pixel is covered with an insulating passivation layer; therefore, avalanche electrons are collected on the metalized bump-bonding pads exposed to the gas. Figure 1(Right) and (Left) shows an enlarged photo of the Medipix2 pixel cells.

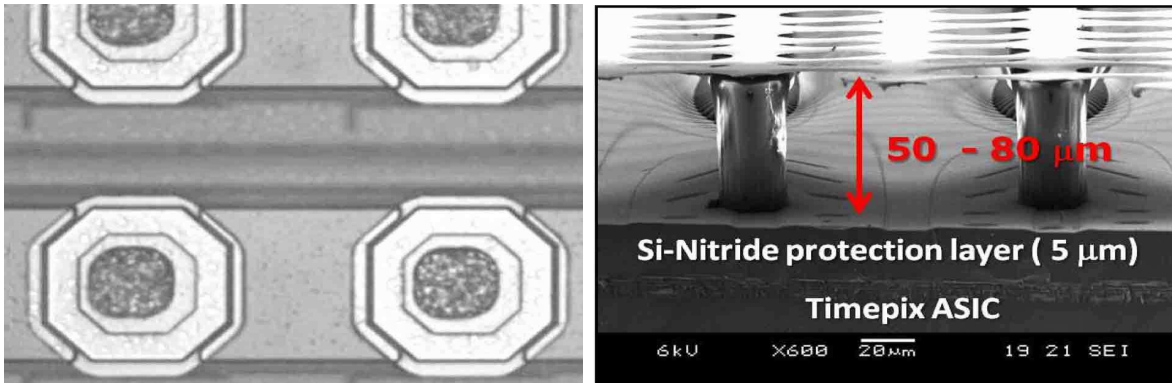

Figure 1: Left: Magnified view of bump-bonding openings on top of the Medipix/Timepix chip. Right: SEM image of the "InGrid" structure with "SiProt" layer.

3 Measurement setup

A special mini-TPC was designed, developed and constructed in Saclay; a schematical drawing of the chamber with the 10 cm field cage is shown in Figure 2. This chamber consists of a printed circuit board where the chip was mounted and wire bonded. The box is built of aluminium with a volume of $\sim 2l$ and has three high voltage connectors and input and output gas pipes. A transparent window for the radioactive source (Fe^{55} photons) was made from a 12 μm Mylar foil. A 10 cm gap field cage was also installed inside the box. The field uniformity is created with the help of 25 voltage degrader rings. Each ring has a height of 3 mm and an isolation of 1 mm between two ring segments. The segments are connected by 1 MΩ resistors and last (bottom) segment is connected to the ground by 10 MΩ resistor. The top and bottom segments are connected via high voltage connectors to the power supplies ($U_{cathode}$ and U_{first}). Remaining HV connector is used to supply grid voltage (U_{mesh}). All voltage parameters were chosen in order to have uniform electric field 200 V/cm inside the field cage. This optimal value was chosen from Magboltz simulation for Ar/Iso (95/5) gas mixture. This experimental setup gives us full sharing of primary electrons that were created in Ar=Iso (95:5) from ^{55}Fe X-rays. The distance between the end of the field cage and the surface of the "InGrid" chip inside the box is 8 mm.

Most of the studies in this analysis were performed using D7-W0056 chip from IZM-3 badge (W0056 plate); measurements were done with and without guard ring using gas P5 (Ar/Isobutan 95/5).

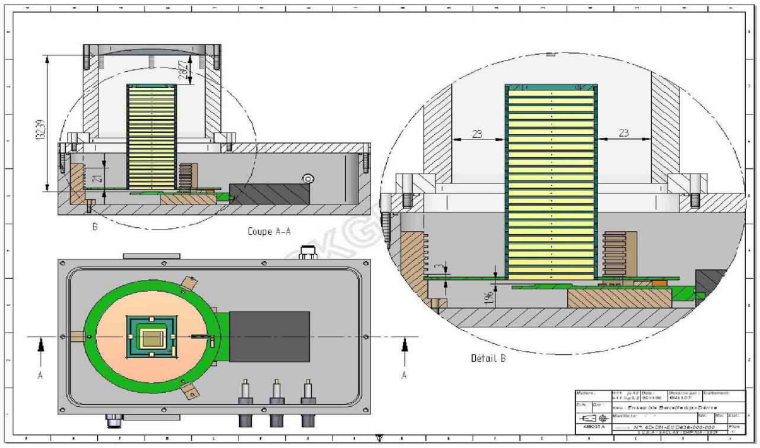

Figure 2: Schematic of the Saclay gas box with 10 cm drift cage

4 Results and discussion

4.1 Data analyses and selection criteria

All data were saved in ASCII files. Format of saving is (x,y,c), where "x,y" are the 2D coordinate of the active pixel and "c" is number of counts for respected counting mode (TOT of Time). For the analysis the ASCII files Medipix Analysis Framework (MAFalda) framework [7], which allows the recognition of particle/tracks, was used. *MAFalda* is a set of algorithms written in the C++ language and based on the Root framework and is dedicated to data analysis of any device of the Medipix family. For different purposes several algorithms were written. Further in the following, criteria used by "SingleIngrid" algorithm, will be explained.

To reject unusable events like cosmics or clusters that were coming from a conversion that was too close to the chip to provide enough separation of the primary electrons by diffusion, some cuts were used. The analyses used the following cuts:

- minimal size of electron cloud
- position of the geometrical center of electron cloud
- circularity of electron cloud

Minimal cluster size needed to skip the events coming from a conversion that was too close to the chip. We suppose that for escape peak for the chosen gas mixture the minimal number of the primary electrons will not be less than 25 electrons (active pixels) in the electron cloud.

Position of the geometrical center was used to avoid the clusters which are registered close to chip border and where part of electrons from the cloud can be lost. The clusters with the geometrical center $(\overline{x}, \overline{y})$ close to the middle of the chip are accepted. The range of 100 central pixels in the middle of the chip in x and y-direction was accepted. If geometrical center is in the range for x-direction

$$75 \leq \overline{x} \leq 175 \tag{1}$$

and the same range is chosen for y-direction, then this cluster is used in analyses. There were chosen 100×100 pixels in the center of the chip. Figure 3 shows the central region acceptable by the geometrical center cut.

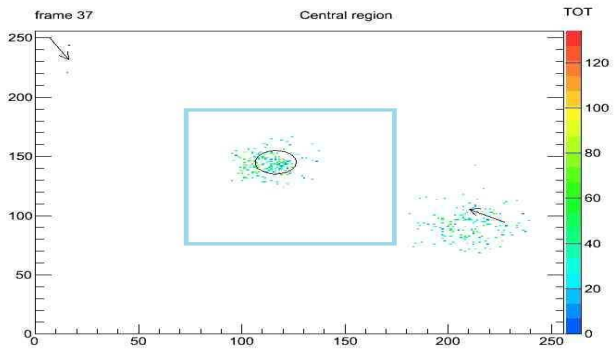

Figure 3: MAFalda event display with central area is highlighted. Only electron clouds with centers in this area are accepted by a geometry center cut.

Circularity of the cluster was used to exclude several electron clouds in TOT mode. The cut is chosen so that circularity is defined as R_a/R_b, where the R_a and R_b are ellipse radii calculated for the cluster. Only electron cloud with

$$0.75 \leq R_a/R_b \leq 1.25 \tag{2}$$

is accepted (Figure 4). This cut helps to reject event where two photon conversions consist in one frame.

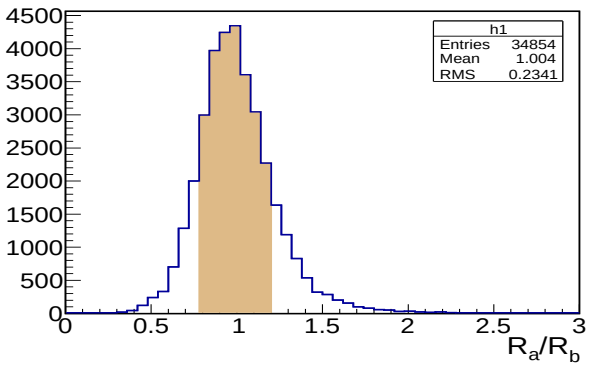

Figure 4: Histogram of the R_a/R_b of the electron cloud in one data sample. The filled area is the data which were used after cut.

4.2 Occupancy results

The optimal value was taken for electric field for current gas mixture from Magboltz simulation. To have the homogeneous electric field $E = 200$ V/cm inside the drift cage the cathode voltage $U_{cathode} = 3100$ V (top of drift cage) and $U_{first} = 1100$ V (bottom of drift cage) was chosen. One can see that field distortions on the border of the chip decrease the sensitive area to $\sim 35\%$, Figure 5 (Left). Figure 5 (Right) demonstrates projection on X-axis for this occupancy plot, but the size of sensitive area can't be enough.

The decision has been made to manufacture and install a guard ring to the setup. The guard ring was installed on the top on chip board in such a manner that the distance between

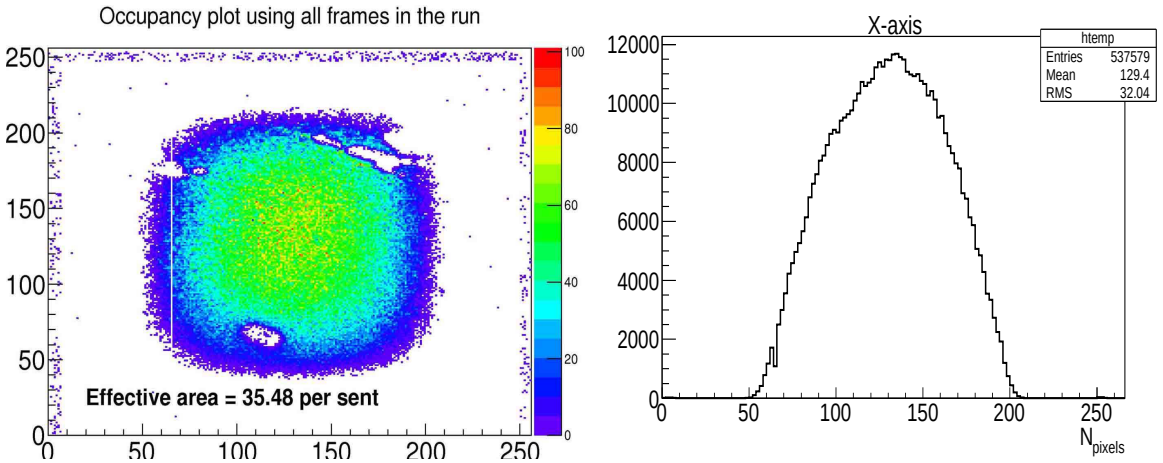

Figure 5: Occupancy plot for the chip D07-W0058 is shown: Left: for the following parameters $U_{mesh} = 350$ V, $U_{first} = 1100$ V and $U_{cathode} = 3100$ V.
Right: projection on X-axis.

mesh and guard ring surface is 1 mm. The voltage on guard ring was the same as on the mesh $U_{mesh} = U_{guard}$. By applying the guard ring the sensitive area can be increased significantly.

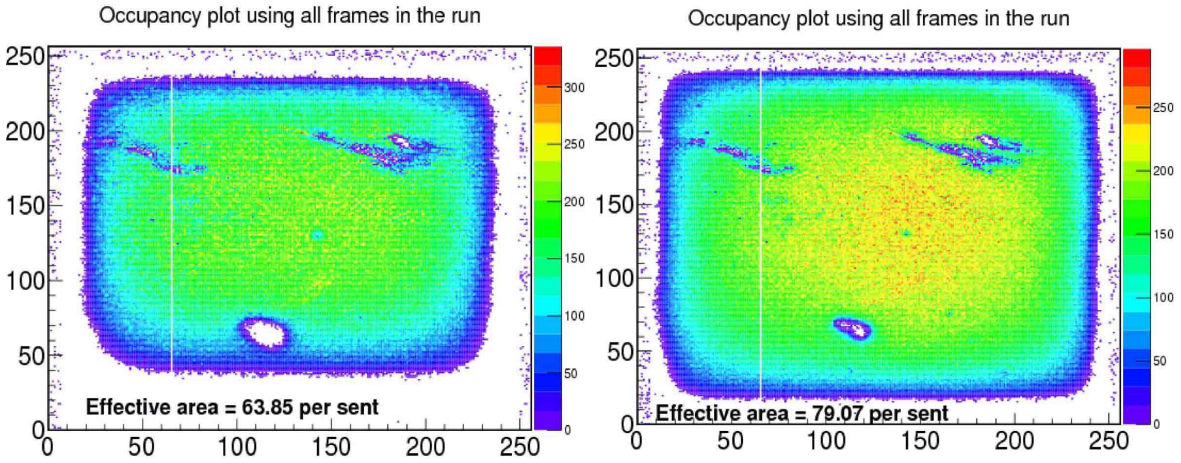
Occupancy plot using all frames in the run
Effective area = 63.85 per sent
Occupancy plot using all frames in the run
Effective area = 79.07 per sent

Figure 6: Occupancy plot for the chip D07-W0058 with guard ring is shown:
Left: for the following parameters $U_{mesh} = U_{guard} = 350$ V, $U_{first} = 600$ V and $U_{cathode} = 2600$ V. Right: for the following parameters $U_{mesh} = U_{guard} = 350$ V, $U_{first} = 1100$ V and $U_{cathode} = 3100$ V.

Using the guard ring with the same potential as the mesh gives us the possibility to decrease field distortions on the edge of the InGrid chip. However, in Figure 6 (Right) the sensitive area is ∼80% with guard ring and highest potential between drift cage and mesh ($U_{first} = 1100$ V), while in Figure 6 (Left) occupancy plot for $U_{first} = 600$ V and gave the sensitive area ∼64% is presented.

4.3 Simulation

For the more proper studies of the field distortions on the chips borders, the simulations were done. Geometry of experimental setup was reconstructed. It consisted of a drift cage and an InGrid chip. The hole in the guard ring is not square-shaped. Such shape was chosen, because one side of chip has wire bonding. To be compared with real experiment, distance between chip and guard ring is 1 mm. All geometry was created in CST EM Studio [8]. Using CST EM Studio electric field simulation was obtained. To compare the MC with measurements simulation without guard ring was done. When field map was obtained it was implemented to Garfield++ by using special tools [9]. Trajectories for every primary electron were obtained using Garfield++. Several simulations for different size of ground around chip (0 mm, 0.5 mm, 1 mm, 2 mm, full grounding of PCB) were performed to find admissible accordance between simulation and experimental data.

4.3.1 Comparison of simulation and experimental data

In this work comparison of experimental data with simulation was done. The realization of simulation was described. Best agreement is shown for a setup with guard ring and without ground around chip.

Statistics of simulation results is poor compared to experimental data, because simulation needs a lot of CPU time. But already at this stage we can see that it is possible to know status of future experiment using this type of simulation. Best agreement is shown for 800 V on bottom side of drift cage for experimental setup in comparison with simulation when ground is 0 mm around the chip.

In Figure 7 comparison of two sets of experimental setup with simulations is shown. One can see that geometrical forms of occupancy for simulation and experiment are similar.

5 Conclusions

The Micromegas and GEM detectors became a wide-spread tool for high-rate tracking of sensitive areas, precision reconstruction of charged particles in the TPC, X-ray etc. In its turn InGrid detectors combine advantages of Micromegas and CMOS chips with high granularity. Thus InGrid detectors could become one of the readout options for ILD TPC.

In this article the possibility to increase the size of sensitive area for a single detector was described. In order to select and analyse measurement data from the radioactive source (Fe^{55} photons), special algorithm and selection criteria were developed. In the studies it was shown that it is possible to reach almost 80% of sensitive area. These results well agreed with simulation. Still, there is a room for optimization when using different voltage on guard ring and on mesh (as was shown in simulation).

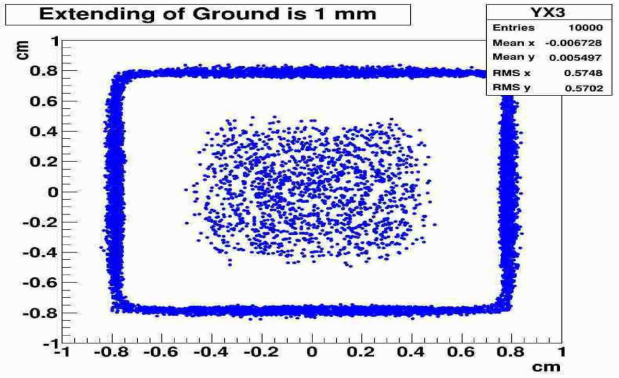

(a) MC, occupancy plot in case without guard ring

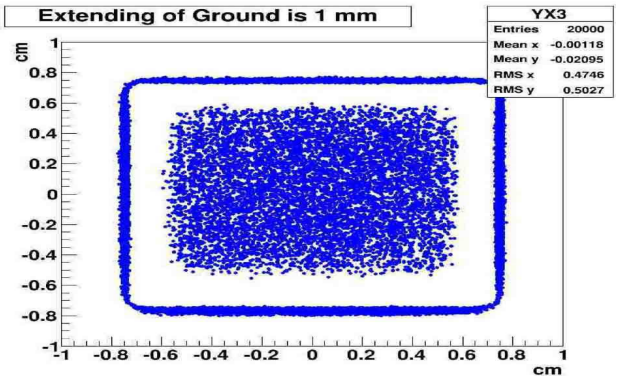

(b) MC, occupancy plot in case with guard ring.

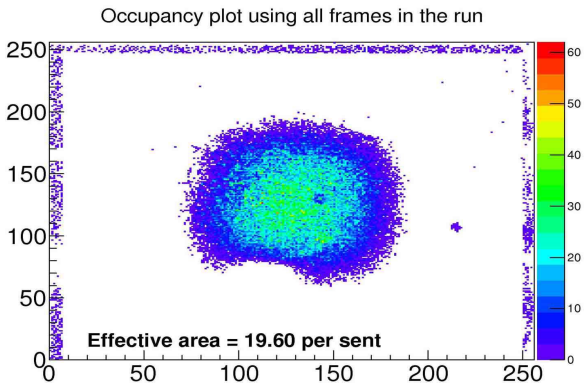

(c) Measured, occupancy plot in case without guard ring.

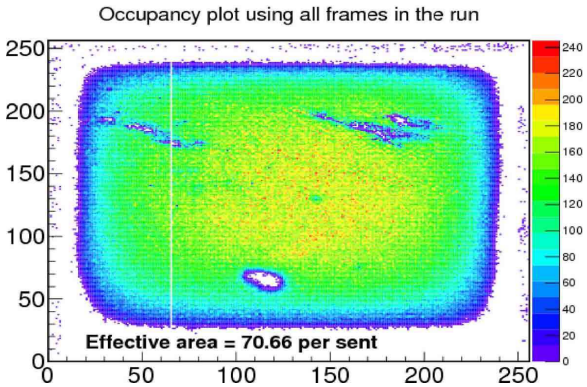

(d) Measured, occupancy plot in case with guard ring.

Figure 7: Monte Carlo simulation. Occupancy plots.

References

[1] R. Bellazzini *et al.*, Nucl. Instrum. Meth. A **535**, 477 (2004) doi:10.1016/j.nima.2004.07.269 [physics/0403019 [physics.ins-det]].

[2] M. Campbell *et al.*, Nucl. Instrum. Meth. A **540** (2005) 295 doi:10.1016/j.nima.2004.11.036 [physics/0409048].

[3] A. Bamberger, K. Desch, U. Renz, M. P. Titov, N. Vlasov, P. Wienemann and A. Zwerger, Nucl. Instrum. Meth. A **573** (2007) 361

[4] X. Llopart, M. Campbell, R. Dinapoli, D. San Segundo, E. Pernigotti, IEEE TNS 49 (2002) 2279-2283.

[5] X. Llopart, R. Ballabriga, M. Campbell, L. Tlustos, W. Wong, Nucl. Instrum. Meth. A **581** (2007) 385,

[6] P. Colas, A.P. Colijn, A. Fornaini, Y. Giomataris, H. van der Graaf, E.H.M. Heijne, X. Llopart, J. Schmitz, J. Timmermans, J.L. Visschers, Nucl. Instrum. Meth. A 535 (2004) 506

[7] MAFalda-framework, https://twiki.cern.ch/twiki/bin/view/Main/MAFalda.

[8] CST simulation packages, https://www.cst.com

[9] K.Zenker, A Garfield++ interface for CST ™, LC-TOOL-2013-022, 8p, http://www-flc.desy.de/lcnotes/notes/LC-TOOL-2013-022.pdf.

LHCb RMS status and operation at 13 TeV

O. Okhrimenko[a], S. Barsuk[b], F. Alessio[c], V. Pugatch[a]

[a] *Institute for Nuclear Research NAS of Ukraine, Kyiv, Ukraine*
[b] *LAL, Université Paris-Sud, CNRS/IN2P3, Orsay, France*
[c] *European Organization for Nuclear Research (CERN), Geneva, Switzerland*

Abstract

In this paper, results of the LHCb Radiation Monitoring System operation in 2015 are presented. Comparison of the RMS baselines behaviour during collisions at 8 and 13 TeV is shown. Integrated luminosity measurements are described.

PACS numbers: 29.40.Mc; 23.40.-s; 23.60.+e; 95.35.+d

Keywords: LHCb, Radiation monitoring, Beam and background control

1 Introduction

By the summer of 2015, the Large Hadron Collider (LHC) has started its operation at a new energy of 13 TeV center-of-mass proton-proton collisions. This is 5 TeV higher than the value of energy explored at CERN during Run1 in the years of 2011–2012. For the LHCb experiment [1], the Run2 period of data taking (2015–2017 years) will be marked by an increase of the instantaneous luminosity up to $4{\cdot}10^{32}$ $\mathrm{cm}^{-2}\mathrm{s}^{-1}$ which is 2 times higher than the initial design value, while keeping the average number of proton-proton interactions per bunch crossing (μ) at a constant value of 1.1, which is between 2 and 3 times higher than the initial design value. These actions are essential steps towards reaching the main goal of the LHCb experiment in precision measurements of the CP-violation phenomena as well as in searching for the rare decay modes of heavy flavored hadron probes. The new domain of the collision energy as well as the increase of the luminosity are good arguments for observation of NP signals. On the other hand, there is an obvious challenge to the experimental techniques for keeping reliable performance in these new and harsh environment. In particular, the silicon microstrip detectors of the LHCb Silicon Tracker (ST) [2] are very sensitive to the radiation load. The Radiation Monitoring System (RMS) installed at the ST IT-2 station in close vicinity to the beam pipe provides real time measurements of the charged particle flux spatial distribution allowing for evaluation of the dose absorbed by the silicon sensors and related increase of the leakage current. The data measured by the RMS are applied to evaluate instantaneous and integrated luminosity of the LHCb experiment relative.

2 The LHCb Radiation Monitoring System

The LHCb experiment is the forward spectrometer located at the interaction point IP8 of the LHC (CERN). The LHCb detector consists of following parts: Vertex Locator (VELO), Silicon (IT, TT) and Outer Trackers to reconstruct tracks of charged particles and their decay vertices;

Magnet to measure charged particle momentum; Cherenkov Detectors (RICH1, RICH2) to separate kaons and pions; Hadronic and Electromagnet Calorimeters (HCAL, ECAL) to measure the particles energy; Muon detector to detect the muons. The level of charged hadron fluxes at the location of the silicon sensors of the ST IT-2 station varies from 10^4 to 10^5 $cm^{-2}s^{-1}$ at nominal LHCb luminosity of $2{\cdot}10^{32}$ $cm^{-2}s^{-1}$ [3]. These fluxes are high enough to make a significant impact onto the performance of the IT silicon sensors and their frond-end electronics caused by the radiation load. The main goal of the RMS is a measurement of that radiation dose load to exclude their damage as a result of an unexpected radiation incident, i.e. change of the beam trajectory, partial beam loss in the region of the detector etc [4, 5].

The RMS is based on the Metal Foil Detector (MFD) technology. The principle of the MFD operation is Secondary Electron Emission (SEE) from the metal foil surface (emission layer $\sim$ 10–50 nm) caused by impinging charged particles. SEE causes positive charge in isolated metal foil read out by sensitive Charge Integrator (ChI). The ChI is equipped by a current-to-frequency converter allowing to achieve high dynamic range (up to 10^6). A current from the stable external source (250 pA) is injected to the ChI's inputs to make baselines ($\sim$ 25 kHz).The MFD is a 5-layer structure manufactured out of 50 μm thick Al foils supported by insulating epoxy frames. The central sensitive layer is connected to the readout electronics, while two neighboring (from both sides) accelerating layers are biased by positive voltage (24 V) to reduce recombination after SEE. The additional two outer shielding layers are grounded. RMS sensor and accelerating layers are divided into 7 parts (110×75 mm, with a layout which is similar to IT silicon sensors size). The RMS consists of 4 modules (Top, Cryo, Bottom, Access) containing 7 sensors each (in total 28 sensors), which are located at IT-2 station ($\sim$ 8.4 m from the LHCb interaction point) around the beam-pipe.

3 Results

3.1 RMS in 2011–2012

The performance of the RMS system was evaluated during the period 2011–2012 while the initial calibration of the RMS was performed in September–October 2010 [6, 7]. In this period, the RMS was exposed to about 29 pb^{-1} of luminosity. The calibration was done during high-intensity beams ($> 10^{11}$ protons-per-bunch).

During the period of data taking 2011–2012, the LHCb experiment took data in these conditions: center-of-mass pp collision energy of 7–8 TeV; average luminosity of $4{\cdot}10^{32}$ $cm^{-2}s^{-1}$; average number of visible collisions per bunch crossing (μ) 1.7; number of colliding bunches per fill up to 1262; bunch spacing 50 ns (corresponding to a total of $\sim$ 20 MHz of bunch crossing rates). A total of about 3.3 fb^{-1} of integrated luminosity was accumulated.

The RMS measures in real time fluxes of charged particles from the LHCb interaction point IP8 as well as radiation induced background. The data accumulated by the RMS were explored to calculate the absorbed dose distribution and related leakage currents increase in the silicon microstrip sensors of the LHCb Inner Tracker. For the operational years 2011–2012, the values are in the range from 0.3 to 1.5 kGy and from 50 to 400 μA, respectively, depending on the sensor position and strip length. The accuracy of the RMS measurements was about 10% , and obtained data were in good agreement with other measurements and Monte-Carlo simulations. More details were described in [8].

3.2 RMS first data in 2015

After the first long shutdown (LS1), LHCb has started collecting data in 2015 under following conditions: proton-proton collisions c.m.s. energy 13 TeV; average luminosity up to $3.8{\cdot}10^{32}$ cm^{-2}s^{-1}; average number of visible collisions per bunch crossing (μ) 1.1; number of colliding bunches per fill up to 1866; bunch spacing 25 ns ($\sim$ 40 MHz of bunch crossing rates). In total, about 0.4 fb^{-1} of integrated luminosity has been currently (October 2015) delivered. Data taking will resume at these conditions in 2016 and LHCb plans to record > 5 fb^{-1} up to the end of 2018, when a second long shutdown will take place.

During LS1, the Top and Access RMS modules were replaced to improve the operational performance (the drift of baselines has become there comparable with modules response to pp collisions). As an example of the upgraded RMS performance the baselines evolution of the Cryo 2 and Access 5 sensors is shown in Figure 1 (top plots) during pp collisions at LHCb in the year 2015 (fill 4449). The fill duration was $\sim$ 15h, 1278 colliding bunches at 25 ns spacing, an average instantaneous luminosity—$2.34{\cdot}10^{32}$ cm^{-2}s^{-1} and average $\mu = 1.08$. Different colors indicate a status of the LHC. Blue one corresponds to "NO BEAM" conditions. The baselines are measured here as 'signal zero' level to be subtracted later to obtain the RMS response to pp collisions. The yellow, green and magenta colors corresponds to "INJECTION", "RAMP" and "ADJUST" LHC status, respectively. During this time proton beams are injected in LHC, ramped to the energy of 6.5 TeV, focused and made collided by applying local corrections on the beams orbits. Finally, the status of "STABLE BEAMS" is declared when the LHCb experiment starts recording data with the full detector on and the DAQ system ready. The red color corresponds to this state of "PHYSICS". For the sake of comparison with the data of the year 2012, the same plot is generated for fill 3318 for the Cryo 2 sensor.

From the Figure 1, it can be seen that the baselines/responses of the new Access module has no large drift anymore but the baselines/responses of all modules are affected by some super-imposing signal during beams circulating at the LHC—from the INJECTION state all the way through the physics data taking period. The two sets of three plots at the bottom in Figure 1 show the baselines/responses parameters (mean and standard deviation) during the various states of a fill. The left plot corresponds to the NO BEAM status before beams injection (blue histogram) and INJECTION + RAMP states (yellow-green histograms). It can be seen that the baseline width has grown up between NO BEAM and INJECTION states. The plot in the middle of the Figure 1 corresponds to the PHYSICS status during the pp collisions. The right plot corresponds to the NO BEAM state after beams were dumped to show that the baselines returned back the nominal ones (i.e. as before injection). The baselines widening has an impact on the accuracy of the RMS fluxes measurements (10–30% depending on the sensor position).

Using data from the Cryo and Bottom modules the integrated luminosity of fill 4449 (2015 year) was estimated using the RMS calibration. The obtained value of 16 ± 6 pb^{-1} agrees well with the official LHCb luminosity of 13 ± 2 pb^{-1}. The Top and Access modules will be calibrated with 2015 data later this year.

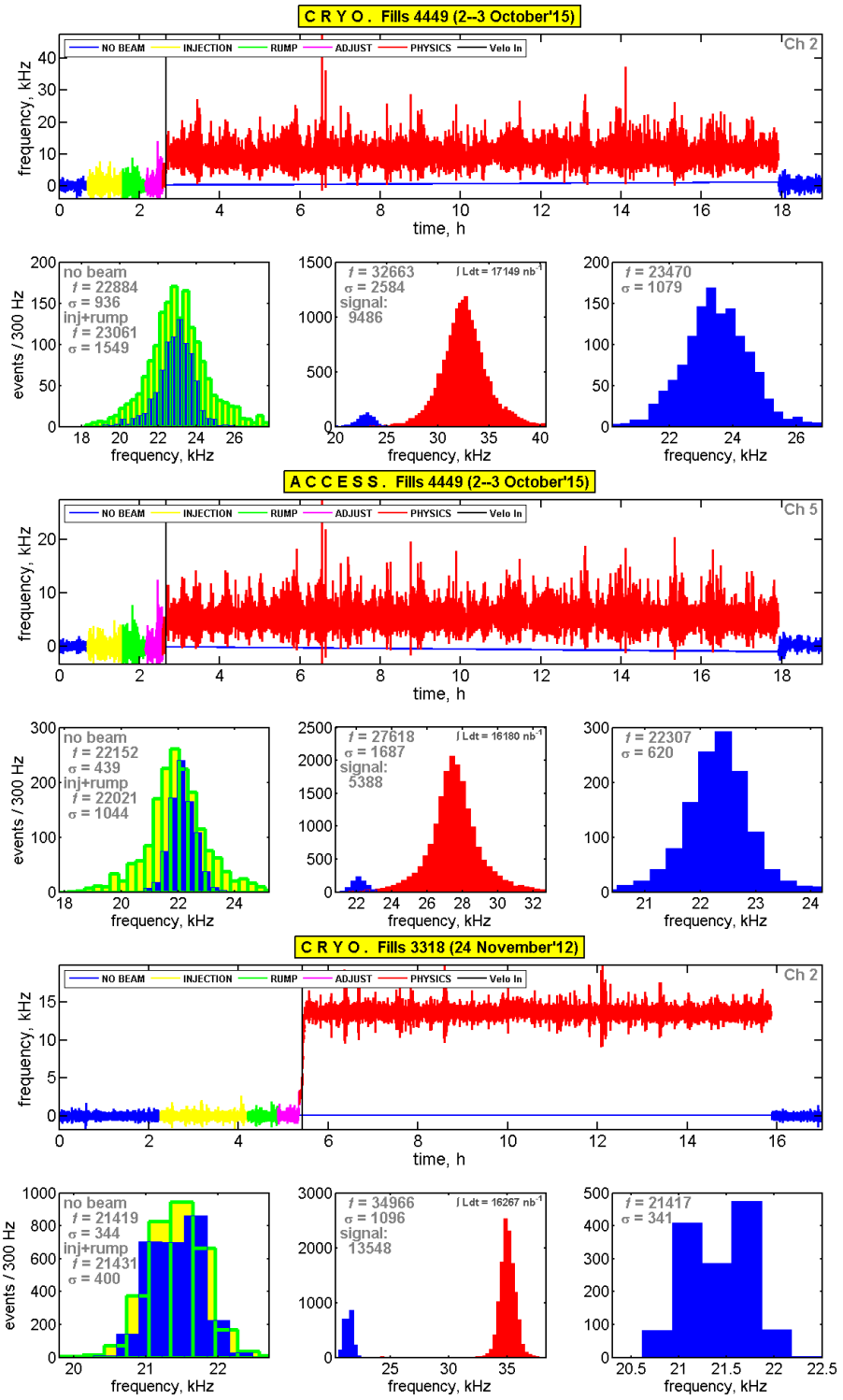

Figure 1: Trend plots for baselines behaviour of Cryo 2 and Access 5 sensors during *pp* collisions at fill 4449 and fill 3318 (top plots) and histograms of these baselines (bottom plots). Different colours corresponds to different LHCb states: blue—NO BEAM; yellow—INJECTION; green—RAMP; magenta—ADJUST; red—PHYSICS.

4 Conclusions

During the years 2011–2012 the Radiation Monitoring System has successfully provided monitoring of the radiation load on Si-sensors of the LHCb Inner Tracker. RMS calibrated data allowed to evaluate the LHCb integrated luminosity. The RMS data are in good agreement with other detectors and Monte-Carlo simulations. The first data taken in 2015 year show that in spite of the baselines widening due to some currently unknown reason RMS allows to monitor the radiation load with an accuracy of 10–30% depending upon the sensor position. The understanding of this problem is under way.

5 Acknowledgement

This research was partially conducted in the scope of the IDEATE International Associated Laboratory (LIA). This work has been supported by the grants CO-4-1/2015 (NASU) and F58/382-2013 (DFFD). We thank the LHCb ST and B&B groups and the LHCb Collaboration. Special thanks to Fred, Helge, and Richard.

References

[1] The LHCb Collaboration, JINST S08005 (2008).

[2] The LHCb Collaboration, LHCb Inner Tracker TDR, CERN/LHCC 2002-29.

[3] V. Talanov, LHCb Note 2000-013.

[4] V. Pugatch et al., LHCb Note 2007-062.

[5] V. Pugatch et al., Ukr. J. Phys, 54(4) (2009) 418.

[6] O. Okhrimenko, V. Iakovenko, V. Pugatch, NPAE 2010 Proceedings (June 7-4, 2010, Kyiv, Ukraine) pp.639–643.
http://www.kinr.kiev.ua/NPAE-Kyiv2010/html/Proceedings/9/Okhrimenko.pdf.

[7] V. Iakovenko, O. Okhrimenko, V. Pugatch, S. Barsuk, M.-H. Schune, Nuclear Physics and Atomic Energy 12(3) (2011) 225–234.

[8] O. Okhrimenko, V. Iakovenko, V. Pugatch, F. Alessio, G. Corti, Proceedings of ICALEPCS 2011 (October 10–14, 2011, Grenoble, France) pp.1115–1118.
http://accelconf.web.cern.ch/AccelConf/icalepcs2011/papers/wepmu024.pdf.

Focusing of relativistic electron Gaussian bunches by nonresonant wakefield excited in plasma

V.I. Maslov[a1], N. Delerue[b], I.P. Levchuk[a], I.N. Onishchenko[a]

[a] *NSC Kharkov Institute of Physics and Technology, Kharkov, Ukraine*
[b] *Laboratory of Linear Accelerator, Orsay Science Centre, Orsay, France*

Abstract: Focusing of relativistic electron Gaussian bunches by nonresonant wakefield, excited by them in plasma, is investigated by numerical simulation. It has been shown that in the case where the electron plasma frequency is larger than the repetition frequency of bunches, all bunches are in focusing wakefield of excited beatings except bunches, which are located at the fronts of beatings where they are not focused.

PACS numbers: 29.17.+w; 41.75.Lx

Keywords: train of relativistic electron bunches, wakefield, plasma lens, focusing

1 Introduction

Focusing of bunches by radial wakefield is an important problem. The intensity of this focusing is larger on a few orders in comparison with usual magnetic focusing [1]. However focusing, which occurs in the plasma at space charge compensation of bunches, is also not enough intense. The intensity of focusing can be increased significantly by using an excited transverse wakefield. Focusing by excited resonant wakefield was studied in [2, 3]. Also a uniform focusing by excited wakefield has been studied in [3, 4] for long bunches and in [5] for short bunches. Because it is difficult to maintain in an experiment a uniform and stationary plasma density, resonant for train of electron bunches, in this paper focusing of train of bunches of relativistic electrons by excited non-resonant wakefield is considered.

2 Nonresonant wakefield plasma lens for short train of bunches

Numerical simulation has been performed using 2d3v-code lcode [6]. For the numerical simulations the following parameters are selected: $n_{res} = 10^{11}$ cm^{-3} is the resonant plasma density which corresponds to $\omega_{pe} = \omega_m = 2\pi \cdot 2.8 \cdot 10^9$, relativistic factor of bunches equals $\gamma_b = 5$. ω_m is the repetition frequency of bunches, $\omega_{pe} = (4\pi n_{res} e^2/m_e)^{1/2}$ is the electron plasma frequency. The density of bunches $n_b = 6 \times 10^8$ cm^{-3} is distributed in the transverse direction according to Gaussian distribution, $\sigma_f = 0.5$ cm, $\lambda = 10.55$ cm is the wavelength, $\xi = V_b t - z$, V_b is the velocity of bunches. Time is normalized on ω_{pe}^{-1}, distance – on c/ω_{pe}, density – on n_{res}, current I_b – on $I_{cr} = \pi m c^3/4e$, fields – on $(4\pi n_{res} c^2 m_e)^{1/2}$.

As it has been shown in [3], at the resonant excitation of wakefield the shorter first fronts of the bunches are defocused by smaller fields, and longer back fronts of the bunches are focused by larger fields (see Fig. 1) i.e. focusing by resonant wakefield is inhomogeneous.

[1]Corresponding author: vmaslov@kipt.kharkov.ua

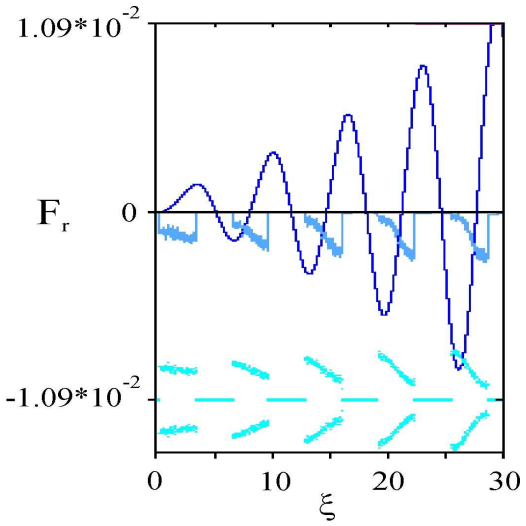

Figure 1: Longitudinal, along train, distribution of radius r_b (bunches-horns in cyan) and density n_b (trapezoids in blue) of train of resonant rectangular bunches and of radial wakefield F_r (oscillating line in dark blue), after their focusing/defocusing at the distance $z = 33$ cm from the boundary of injection at $\xi_b = \lambda/2 = 5.275$ cm, $I_b = 0.45 \times 10^{-3} = 6$ A. Normalized length of 30 for the train of bunches in the Fig. 1 corresponds to a length of 50.6 cm or to a duration of 1.68 ns. The achieved normalized radial wakefield $F_r = 1.09 \times 10^{-2}$ after five bunches corresponds to 3.27 kV/cm.

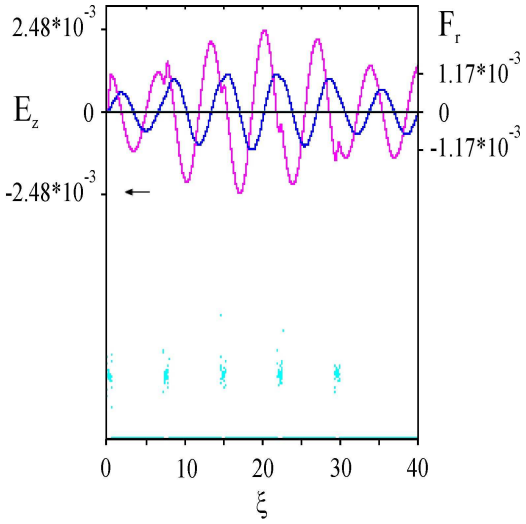

Figure 2: Longitudinal, along train, distribution of radius r_b (points in cyan) of train of very short Gaussian bunches, of radial wakefield F_r (oscillating line of smaller amplitude in blue) and of longitudinal wakefield E_z (oscillating line of larger amplitude in magenta) near the boundary of injection at $n_e = 1.35 n_{res}$, $\xi_b = 0.1\lambda = 1.055$ cm, $I_b = 1.56 \times 10^{-3} = 20.9$ A. The arrow shows the direction of the bunch motion.

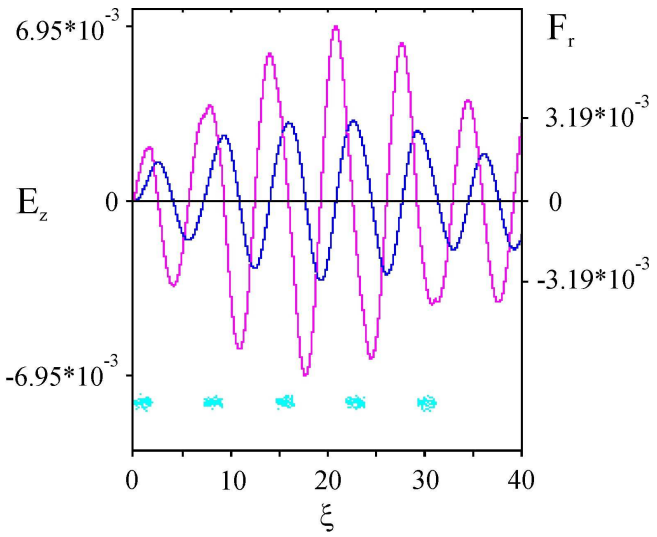

Figure 3: Longitudinal distribution, along the train, of radius r_b (short linear segments) of train of rectangular bunches of length, $\xi_b = \lambda/4 = 2.6375$ cm, of radial wake force F_r (oscillating line of smaller amplitude) and of longitudinal wakefield E_z (oscillating line of larger amplitude) near boundary of injection at $n_e = 1.35 n_{res}$, $I_b = 10^{-3} = 13.4$ A.

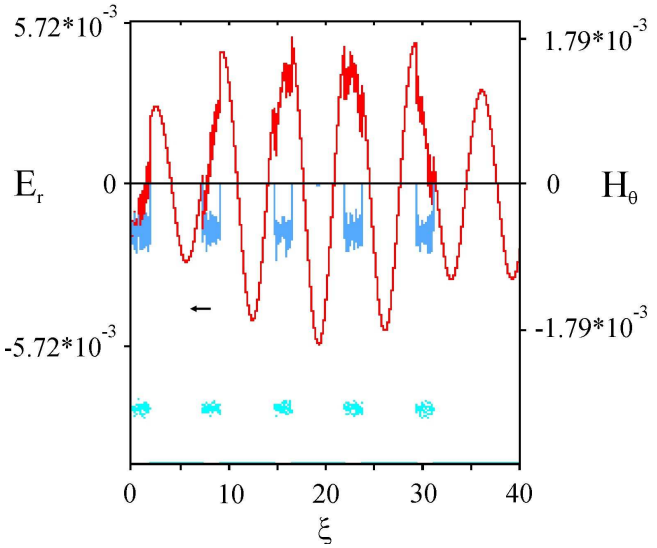

Figure 4: Longitudinal, along train, distribution of radius r_b (short linear segments) of train of rectangular bunches of length $\xi_b = \lambda/4$, of radial wakefield E_r (oscillating line) and of magnetic wakefield H_θ (trapezoids) near boundary of injection at $n_e = 1.35 n_{res}$, $I_b = 10^{-3}$.

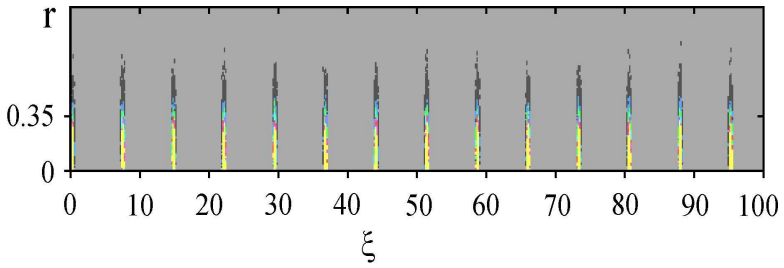

Figure 5: Spatial in (r, ξ) distribution of density n_b of train of very short approximately Gaussian bunches $\xi_b = 0.1\lambda$ near boundary of injection at $n_e = 1.35 n_{res}$, $I_b = 1.56 \times 10^{-3}$.

Let us consider the optimum parameters for the case of nonresonant wakefield plasma lens for short train of identical bunches of relativistic electrons. I.e. we will show that for selected: the length of bunches, less than half the wavelength $\xi_b < \lambda/2$, their number N_b and repetition frequency of bunches ω_m there is a range of suitable electron plasma frequency ω_{pe} such that all bunches are in focusing wakefields F_r. As it will be demonstrated below, that in the case $\omega_{pe} > \omega_m$ all point (very short) bunches are in focusing or in a zero radial field, we use the range of parameters when $\omega_{pe} > \omega_m$. For determination the optimal parameters we use two conditions. Namely, that all N_b bunches are placed on the length of a beating, it is necessary $0 < \omega_{pe} - \omega_m < \omega_{cr}$. ω_{cr} is some critical frequency, associated with N_b. At the same time, for all electrons of all bunches are in focusing wakefields, it is necessary $\xi_b < xi_{cr}$.

In the case of point $\xi_b \to 0$ bunches one restriction is removed, and the relative position of bunches and F_r at $n_e/n_{res} - 1 = 0.35$ (n_{res} is determined from $(4\pi n_{res} e^2/m_e)^{1/2} = \omega_m$) has the form shown in Fig. 2. One can see that $N_b = 5$ bunches are in focusing wakefields F_r. In the case of bunches of finite length, $\xi_b = \lambda/4$ at the plasma density, equal to $n_e = 1.35 n_{res}$, the relative position of bunches and F_r has the form shown in Figs. 3, 4. F_r is the total, i.e. radial field of the space charge of the bunch, wakefield and its own magnetic field of the bunch current H_θ. E_r is the total, i.e. radial field of the space charge of the bunch and wakefield. As one can see, for each frequency difference $\omega_{pe} - \omega_m$ there exist the length of train and the length of the bunches, when all the electrons of all bunches are in focusing fields.

Let us consider the distribution of longer train of short relativistic electron bunches (Fig. 5) relative to excited wakefield beatings at $\omega_{pe} > \omega_m$ (Fig. 6).

At $\omega_m < \omega_{pe}$ beatings are excited. All bunches are in focusing fields of beatings except at fronts of beatings, where they are not focused.

In the case of bunches of length $\xi_b = \lambda/4$, $\lambda = 2\pi V_b/\omega_p$ one can see Fig. 7 and Fig. 8.

All bunches are in focusing fields except at fronts of beatings, where they are not focused. Let us compare focusing in nonresonant (Fig. 9) $\omega_m < \omega_{pe}$ and in resonant (Fig. 10) $\omega_m = \omega_{pe}$ cases.

One can see that in nonresonant case all bunches are focused except at fronts of beatings, where they are not focused.

Now we consider the long train of short Gaussian bunches. The train is shaped according to linear dependence. The space interval between bunches equals to the wavelength (see Fig. 11). One can see that all bunches are in maxima of focusing field and thus they are decelerated slowly, as they are in zero decelerating field, excited by previous bunches.

Now we consider the long train of Gaussian bunches, shaped according to linear dependence. The space interval between bunches is equal to the wavelength, and the bunch length equals

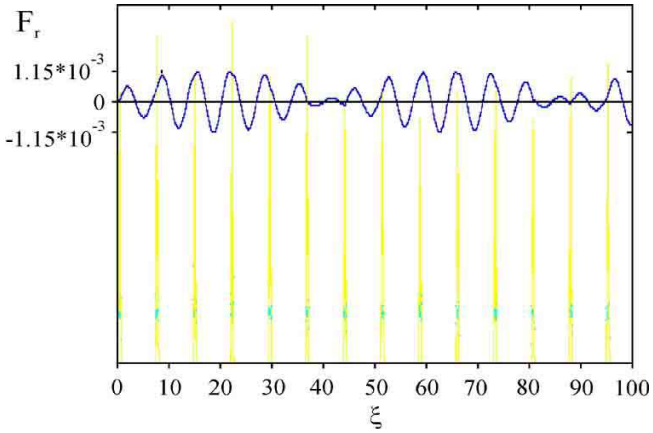

Figure 6: Longitudinal, along train, distribution of radius rb (points), of density nb (vertical lines) of train of very short approximately Gaussian bunches $\xi_b = 0.1\lambda$ and of radial wake force F_r (oscillating line) near boundary of injection at $n_e = 1.35 n_{res}$, $I_b = 1.56 \times 10^{-3}$.

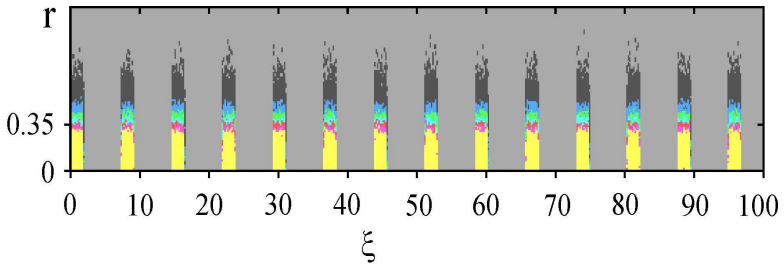

Figure 7: Spatial in (r, ξ) distribution of density nb of train of rectangular bunches of length $\xi_b = \lambda/4$ near boundary of injection at $n_e = 1.35 n_{res}$, $I_b = 10^{-3}$.

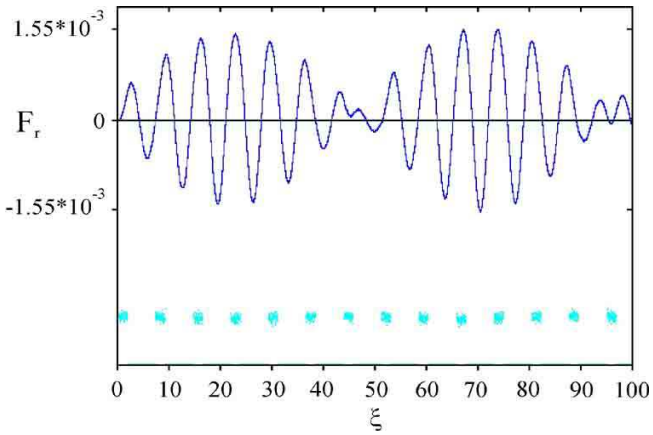

Figure 8: Longitudinal, along train, distribution of radius r_b (short linear segments) of train of rectangular bunches of length $\xi_b = \lambda/4$ and of radial wake force F_r (oscillating line) near boundary of injection at $n_e = 1.35 n_{res}$, $I_b = 10^{-3}$.

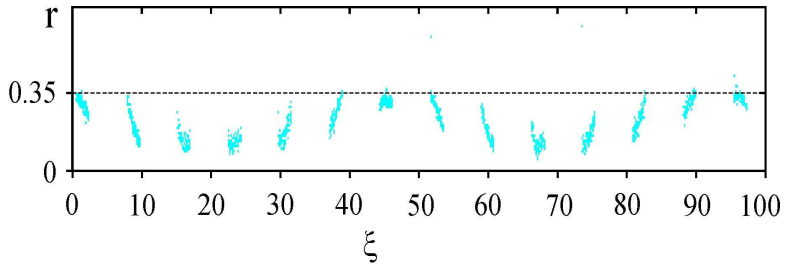

Figure 9: Longitudinal, along train, distribution of radius r_b of train of rectangular bunches of length $\xi_b = \lambda/4$ at $n_e = 1.35 n_{res}$, $I_b = 10^{-3}$ after their focusing at the distance z=50cm from the boundary of injection.

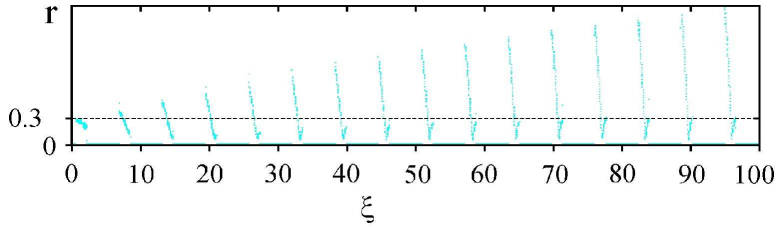

Figure 10: Longitudinal, along train, distribution of radius r_b of resonant train of rectangular bunches of length $\xi_b = \lambda/4$ at $I_b = 10^{-3}$ after their focusing/defocusing at the distance $z =$ 50 cm from the boundary of injection.

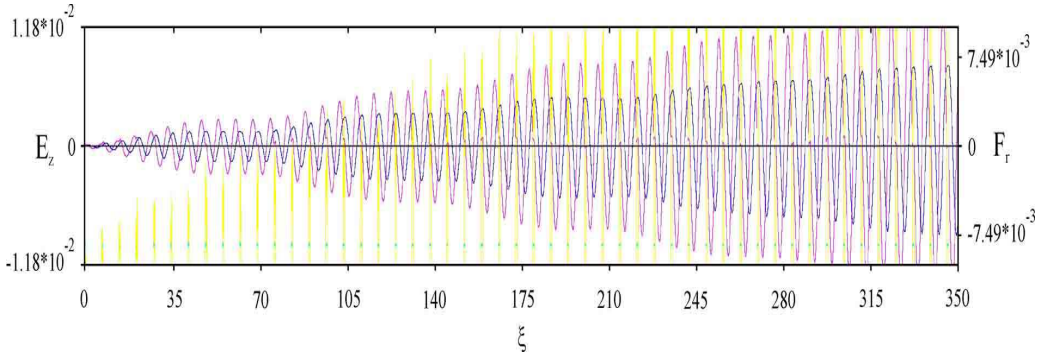

Figure 11: Longitudinal, along train, distribution of radius r_b (points) and density n_b (vertical lines) of long shaped according to linear dependence train of very short bunches, of radial wake force F_r (oscillating line of smaller amplitude) and of longitudinal wakefield E_z (oscillating line of larger amplitude) near boundary of injection at $I_b = 10^{-3}$.

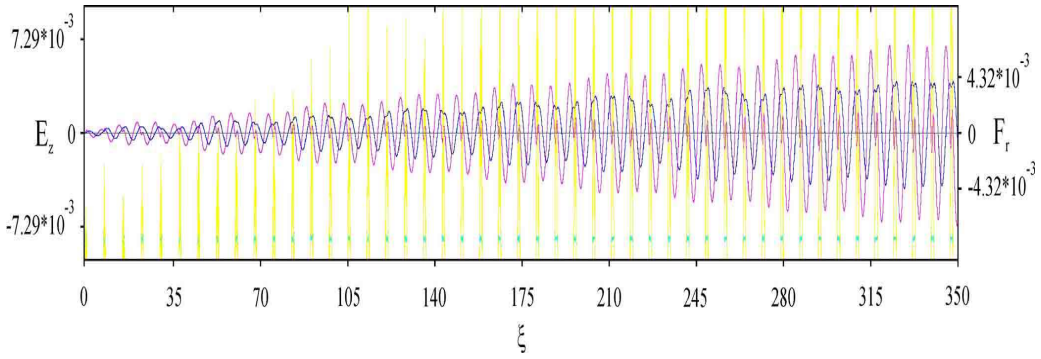

Figure 12: Longitudinal, along train, distribution of radius r_b (points) and density n_b (vertical lines) of long shaped according to linear dependence train of approximately Gaussian bunches, the length of which equals $\xi_b = \lambda/5 = 2.11$ cm, of radial wake force F_r (oscillating line of smaller amplitude) and of longitudinal wakefield E_z (oscillating line of larger amplitude) near boundary of injection at $I_b = 2.5 \cdot 10^{-3} = 33.5$ A.

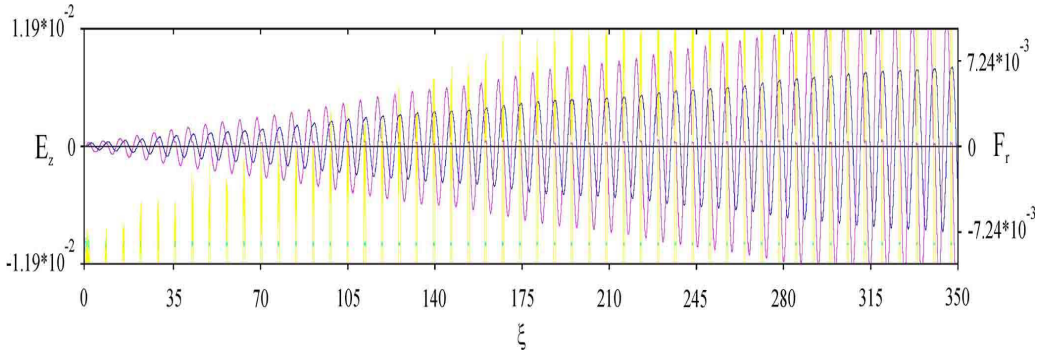

Figure 13: Longitudinal, along train, distribution of radius r_b (points) and density n_b (vertical lines) of long train with precursor shaped according to linear dependence along train as well as along each bunch, of radial wake force F_r (oscillating line of smaller amplitude) and of longitudinal wakefield E_z (oscillating line of larger amplitude) near boundary of injection at $I_b = 10^{-3}$.

$\xi_b = \lambda/5$ (Fig. 12). Also we consider a long train of short bunches with precursor, shaped according to linear dependence along the train and along each bunch (Fig. 13). The space interval between bunches equals wavelength. One can see that in both cases all bunches are in maximal focusing fields and in a small E_z.

Thus, bunches of sequence, shaped according to linear dependence, and bunches of sequence, shaped according to linear dependence with precursor, are in maximal focusing fields.

3 Conclusions

Focusing of relativistic electron bunches by nonresonant wakefield, excited by them in a plasma, has been investigated by numerical simulation. It has been shown that in the case where the electron plasma frequency is larger than the repetition frequency of bunches, all bunches are in focusing wakefield of excited beatings except bunches, which are located at the fronts of beatings which are not focused.

References

[1] G. Hairapetian, P. Devis, C. Joshi, C. Pelegrin, T. Katsouleas, Phys. Plasma. 2 (1995) 2555.

[2] Ya.B. Fainberg, V.A. Balakirev, V.I. Karas, A.K. Berezin, V.A. Kiselev, I.N. Onishchenko, A.P. Tolstoluzhsky, Pizma ZhTF. 22 (1996) 31.

[3] V.I. Maslov, I.N. Onishchenko, I.P. Yarovaya, Problems of Atomic Science and Technology. Series Plasma Physics. 1 (2013) 134.

[4] K.V. Lotov, V.I. Maslov, I.N. Onishchenko, O.M. Svistun, Problems of Atomic Science and Technology. 3 (2012) 159.

[5] V.I. Maslov, I.N. Onishchenko, I.P. Yarovaya, East European Journal of Physics Department of Physics and Technologies. 1 (2014) 92.

[6] K.V. Lotov, Phys. Plasmas. 5 (1998) 785.

Modelling point defects dynamics in irradiated foils: patterning and pattern selection

D. Kharchenko, V. Kharchenko, I. Lysenko

Institute of Applied Physics NAS of Ukraine

Abstract

Dynamics of nano-sized vacancy clusters formation in a prototype systems of an irradiated foils is studied by using a dynamical model describing spatio-temporal behavior of vacancy concentration and temperature of irradiated sample. It is shown that pattern selection processes and morphology of defect structures can be controlled by damage rate. Oscillatory dynamics of both vacancy concentration and sample temperature is analyzed. It is shown that the mean size of vacancy clusters (from 30nm up to 300nm) evolves in oscillatory manner due to pattern selection processes.

PACS numbers: 05.40.-a, 89.75.Kd, 65.80.-g, 81.16.Rf

Keywords: defects, pattern formation, nano-structure, thermal effects

1 Introduction

It is well known that irradiated materials are nonequilibrium systems manifesting self-organization of nano-structures of point defects due to laser or particle irradiation. These processes are results of rearrangement of mobile point defects (vacancies (v), interstitials (i, doped atoms) produced by an irradiation influence. It leads to formation of surface structures like dots having sizes of nano- or micrometers on semiconductors and metals [1]. Depending on irradiation conditions (displacement damage rate and temperature) point defects can arrange into objects of higher dimension such as clusters (di-, tri-, tetra-vacancy clusters), defect walls with vacancy and interstitial loops, voids, precipitates and bubble lattices. Fabricated in such a way nano-structured thin films or foils can be exploited in developing novel electronic devices, memory storage, detectors, etc. A rearrangement of mobile nonequilibrium point defects leads to emergence of mechanical stresses in irradiated foils. This results to self-organization of nano-structures leading to compensation of such stresses [2].

Usually, considering dynamics of defects in a bulk one admits that the temperature of the irradiated sample remains constant due to high thermal conductivity (for example, for metals) and one can control the surface morphology varying damage rate (defects production rate) only. This effects is possible for massive samples. In most of studies it is assumed that the system attains the thermal state realized under stationary external conditions. At the same time it is well known that in thin foils (with thickness around $0.3 \div 0.5\mu m$) a nonequilibrium defect concentration and a temperature of a sample are able to reach much higher values than stationary ones and oscillate around them. In thin foils local temperature variations of a sample due to irradiation and point defect rearrangement can be realized. Considering foils as a sample in an environment characterized by a constant temperature one deals with processes of local changes in the sample temperature due to its heating, production of defects

and their annihilation (a range of ionizing particles is smaller then thickness of the sample). A local increase in the sample temperature results in defects annealing. It leads to defect energy release into a heat increasing the temperature of the sample. As a result a number of defects decreases with increasing the heat transfer. Next, the sample cools, heat transfer decreases and new defects accumulate. A repetition of this scenario leads to self-oscillations of the sample temperature and point defects concentration. An emergence of such self-oscillations in homogeneous systems were reported in Ref. [3]. There are many experimental observations of self-organization of point defects in solids with spatio-temporal oscillations of point defect concentration (see, for example, Refs. [4, 5]). Among them one can note: void size oscillations were observed in irradiated nickel samples [6]; temperature oscillations of crystals CH_4 were reported in Ref. [5]; periodic variations of microhardness of Nimonic 90 with γ-precipitates with radiation dose growth were discussed in Ref. [7].

From the theoretical and practical viewpoints one of the interesting problem relates to study surface layer self-organization of point defects due to irradiation influence with redistribution of the conjugated temperature field. In this work we study spatio-temporal evolution of point defects and local temperature in a prototype model of irradiated sample following the approach developed in Refs. [2, 8], where local temperature field in irradiated layers evolves according to main mechanisms proposed in Ref. [3]. We take into account fluctuations in damage rate related to the fact that bombarding particles have dispersion in energy. In our consideration we assume Gaussian fluctuations in defect production rate and study an influence of these fluctuations onto stationary surface patterns realization. It should be noted that we study patterning effects due to point defects interaction in a prototype theoretical model excluding sputtering and erosion of the surface. The main attention is paid to describe formation of clusters of point defects and patterning of the conjugated temperature field caused by agglomeration of defects. We consider a development of spatio-temporal patterns manifesting pattern selection processes.

2 Prototype model of irradiated foils

Considering a system (irradiated metallic foil), dynamics of concentration of point defects (interstitials and vacancies, $c_{i,v} = c_{i,v}(\mathbf{r}, t)$, $\mathbf{r} = \{x, y, z\}$) and local temperature $T(\mathbf{r}, t)$ of a sample can be described by following equations:

$$\begin{aligned} \partial_t c_v &= \mathcal{K} - \beta_v(c_v - c_v^0) - \alpha c_i c_v - \nabla \cdot \mathbf{J}_v, \\ \partial_t c_i &= \mathcal{K} - \beta_i c_i - \alpha c_i c_v - \nabla \cdot \mathbf{J}_i, \\ C\rho \partial_t T &= \chi \Delta T - \frac{\gamma_0}{h}(T - T_0) + \zeta E_f \mathcal{K} + E_f[\beta_v(c_v - c_v^0) + \alpha c_i c_v], \end{aligned} \tag{1}$$

where $\mathcal{K}$ is the defect production rate; $\beta_{i,v} = \rho_d D_{i,v}$ is the inverse lifetime of defects of i/v type defined through the dislocation density ρ_d and diffusion coefficient $D_{i,v}$, c_v^0 is the equilibrium vacancy concentration, α is the recombination rate. In equation for the local temperature T (measured in energetic units) of a sample C is the specific thermal capacity, χ is the thermal conductivity, γ_0 is the heat transfer coefficient, h is the foil thickness, T_0 is the environment temperature; $\zeta \gg 1$ is the ratio of energy of irradiation which transforms into heating and energy of irradiation which transforms into defect generation; E_f is the energy of defect formation; the last term defines energy release when defects are captured by dislocations and due to

recombination with interstitials. As far as we consider thin foils one can put $z = 0$ and study planar problem only. Here we assume that a substrate for the layer location does not affect the irradiation influence, or its influence on substrate is negligible small, and is not considered. Formally, by using the well known relation between diffusivities $D_i/D_v \gg 1$, one can exclude the fast variable c_i, setting $\partial_t c_i \simeq 0$. The diffusion flux of vacancies as mobile species is defined as follows $\mathbf{J}_v = -D_v \nabla c_v + c_v \mathbf{v}$, where the first term is responsible for the free diffusion of defects, the second term relates to the thermodynamical (chemical) force $\mathbf{f} = -\nabla(U/T)$ influence inducing a speed $\mathbf{v} = D_v \mathbf{f}$; here U is the interaction potential between defects. The lateral force exerting on the defect from the deformed elastic continuum is $-\nabla U = \theta_d \nabla \vartheta|_{z=0}$, where $\vartheta(\mathbf{r}) = \nabla \cdot \mathbf{u}$, $\mathbf{u} = \mathbf{u}(\mathbf{r}, t)$ is the vector of material displacement in the layer, $\theta_d \equiv \Omega K$ is the strain potential of defect, K is the elasticity modulus. As was shown in previous studies (see Ref. [2]) the deformation of the surface layer depends nonlocally on the defect concentration on the surface as follows: $\vartheta(z = 0) = \frac{\nu \theta_d}{\rho c_{||}^2} \mathcal{L} c_v, \quad \mathcal{L} = (1 + l_{||}^2 \Delta)$; here $\nu = (1 - 2\sigma_P)/(1 - \sigma_P)$, σ_P is the Poisson coefficient of the layer; $c_{||}^2 = E/\rho(1 - \sigma_P^2) = \sigma_{||}/\rho$ is the bending stiffness; E is the Young modulus; ρ is the density; $\sigma_{||}$ is the tensile isotropic stress in the defect-enriched surface layer of the height h (thickness of radiation induced defect enriched surface layer); $l_{||} = h(\rho c_{||}^2/12\sigma_{||})^{1/2}$.

Next, it is convenient to use rescaled concentration $x \equiv \mu c_v$ with $\mu \equiv \alpha/\beta_i$. Measuring time in unites $\tau_d \equiv (\rho_d D_v^0)^{-1}$, spatial coordinate in units $L_D \equiv (\rho_d)^{-1/2}$, one can introduce dimensionless quantities $t' \equiv t/\tau_d$, $\mathbf{r}' \equiv \mathbf{r}/L_D$, $\ell \equiv l_{||}/L_D$, $\epsilon \equiv \nu \theta_d^2/\mu \rho c_{||}^2 T_0$, $\Theta \equiv T/T_0$, $\eta \equiv C\rho h/\tau_d \gamma_0$, $\kappa \equiv \chi h/L_D^2 \gamma_0$, $\varpi \equiv E_f h/T_0 \mu \tau_d \gamma_0$, $\varepsilon \equiv E_v/T_0$. Generally, in order to make a statistical description one assumes that defects can be produced in stochastic manner due to fluctuations in damage rate. Hence, by taking $\mathcal{K} \to \mathcal{K}(t) = \mathcal{K}_0 + \xi(t)$, where $\xi(t)$ is a white Gaussian noise with properties $\langle \xi(t) \rangle = 0$, $\langle \xi(t)\xi(t') \rangle = 2\mathcal{K}_0 \sigma^2 \delta(t - t')$ one admits that fluctuations in the damage rate are possible at nonzero flux described by $\mathcal{K}_0$; σ^2 denotes fluctuations intensity.

3 Results and discussion

Considering $\mathcal{K}$ and T_0 as independent parameters and using material constants for pure Ni one can obtain phase diagram illustrating domain of oscillatory dynamics (see Fig.1a). The typical set of the system parameters is: $\mathcal{K} \sim 10^{-3} dpa/sec$, $T_0 \in [300, 900]K$, $L_D \simeq 10^{-7} m$, $\tau_d \simeq 10^{-6} sec$, $E_f = 1.6eV$, $h = 0.5\mu m$, $\eta = 100$, $\kappa = 1$, $\ell = 0.7$, $\zeta = 7$, $\varpi = 0.1$, $\mu \simeq 10^8$. According to obtained diagram one finds that in the deterministic limit ($\sigma^2 = 0$) oscillatory dynamics is realized at values of $\mathcal{K}$ and T_0 lying above the solid line. In the stochastic case ($\sigma^2 \neq 0$) fluctuations do not change lower values of $\mathcal{K}$ and T_0 belonging to the solid line. The noise leads to bounding the domain of oscillatory dynamics limiting upper values of damage rate and the temperature T_0. Hence, oscillations are possible inside the bounded domain for $\mathcal{K}$ and T_0 in the stochastic system ($\sigma^2 \neq 0$).

From the linear stability analysis one can obtain a period r_0 of spatial patterns realized during irradiation (see Fig.1b). It is seen that with an increase in the damage rate $\mathcal{K}$ the period of patterns slightly increases. The noise does not affect the quantity r_0 essentially (not shown here). Exposing the target at elevated environment temperature T_0 one can generate patterns with larger period.

To make a quantitative analysis we solve numerically the system (1) on a quadratic grid with linear size $9.2L_D$. Typical patterns of both defect concentration field and temperature

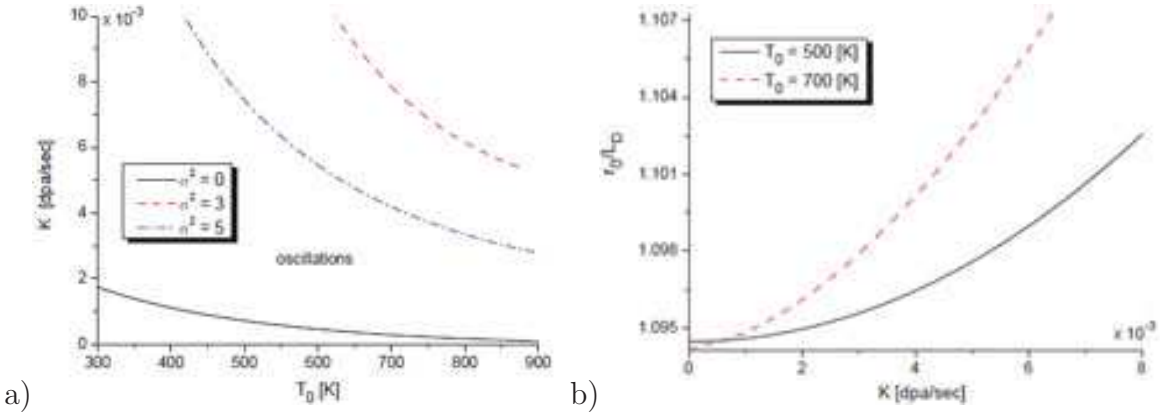

a) b)

Figure 1: (a)Phase diagram for linear stability analysis. Domain of oscillatory dynamics is bounded by solid curve. (b) Dependencies of period of patterns at different T_0

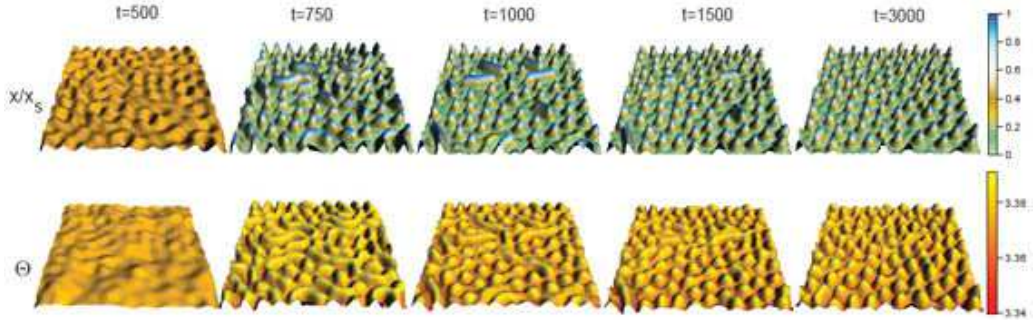

Figure 2: Snapshots of vacancy concentration field (top panels) and temperature field (bottom panels) at $T = 500K$: $\mathcal{K} = 3 \cdot 10^{-3} dpa/sec$ in the deterministic case; x_s denotes the stationary homogenous vacancy concentration

of the target at different times are shown in Figs.2. It is well seen that during the system evolution formation of vacancy patterns with nonuniform distribution of the temperature field is realized. The local temperature is larger in domains with vacancy clusters. Here one gets dot-like patterns, where vacancies are concentrated in spherical clusters forming voids/holes on the surface of the target. Increasing the damage rate one induces a formation of nonequilibrium vacancies able to form elongated clusters transformed into ripples.

From Fig.3a it follows that both $\langle x \rangle$ and $\langle \Theta \rangle$ manifest small decaying oscillations near the steady states. Such oscillatory behaviour is responsible for pattern selection processes. At this stage one can observe formation of patterns with spherical and elongated structures. During exposing the system selects one type of spatial structures. As far as temperature variations are strongly related to behaviour of vacancies, therefore, temperature oscillations become possible at this stage. Oscillatory dynamics of a mean radius of vacancy islands $\langle R(t) \rangle$ and their number $N(t)$ (see Fig.3b) illustrate that pattern formation starts from organization of small amount of clusters having large characteristic lengths. During the system evolution some of them dissolves, some new clusters can emerge due to interactions of supersaturated vacancies. With an increase in the exposition time most of clusters become identical and are characterized by the constant averaged radius at large time scales. To estimate $\langle R \rangle$ we take $L_D \simeq (\rho_d)^{-1/2}$ with $\rho_d \simeq 10^{14} \div 10^{12} m^{-2}$. It gives typical size of vacancy clusters $\langle R \rangle \simeq 0.3 L_D \simeq 30 \div 300 nm$; the

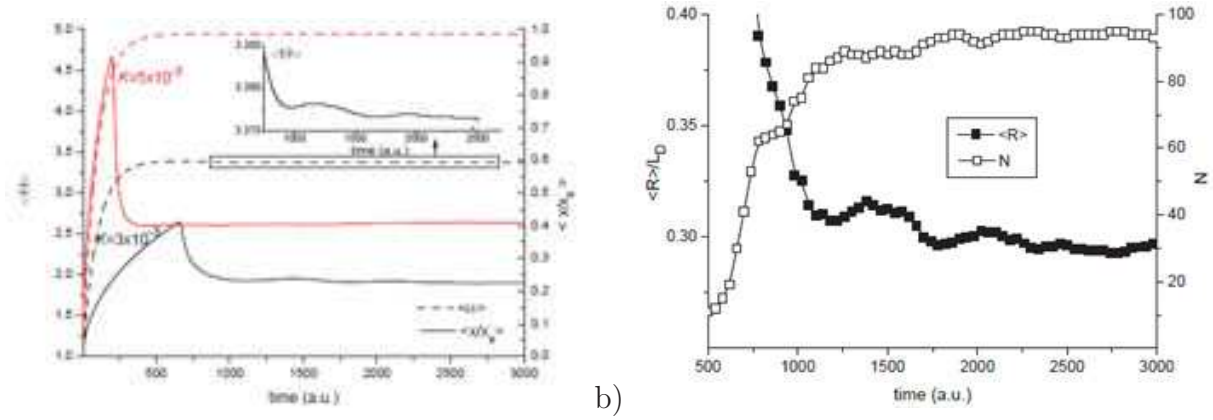

Figure 3: Evolution of averaged temperature of a sample and concentration of defects (panel a) and mean radius $\langle R \rangle$ of spherical vacancy clusters (filled squares) with the corresponding number of clusters (empty squares) (panel b) at $\mathcal{K} = 3 \cdot 10^{-3} dpa/sec$, $T_0 = 500K$

related distance between them is around diffusion length. Dynamics of $\langle R \rangle$ is accompanied by an increase in the number of islands toward the corresponding stationary value.

4 Conclusions

It was shown that pattern selection processes are realized due coupling between defect concentration and sample temperature fields. We have shown that stochastic contribution can reduce the domain of pattern selection processes. Oscillatory dynamics of both vacancy concentration and temperature of the sample averaged over the whole system is discussed. It was found that pattern selection processes are accompanied by decaying oscillatory dynamics of mean size of vacancy islands and their number.

5 Acknowledgement

The support of the LIA project is greatly acknowledged.

References

[1] Daniel Walgraef *Spatio-Temporal Pattern Formation* (Springer-Verlag, New York, Berlin, Heidelberg, 1996).

[2] V.I.Emel'yanov, Quantum Electronics, **36**(6), 489 (2006); V.I.Emel'yanov, D.M.Seval'nev, Laser Physics, **21**, 566 (2011)

[3] P.A.Selischev, V.I.Sugakov, *Auto-oscillation processes in impure crystals under irradiation* (in: Effects of Radiation on Materials, Ed.by R.E.Stoller, Arvind S.Kumar, David S.Gelles, ASTM, Philadelphia, pp.594-599, 1992)

[4] K.Krishan, Phil.Mag., **45**, 401 (1981)

[5] J.M.Carpenter, Nature, **36**, 358, (1987)

[6] J.K.Steel, D.I.Potter, J.Nucl.Mat., **218**, 95 (1995)

[7] K.Varatharajan, R.V.Nandedkhar, *Microhardness-microstructure study of aged Nimonic 90 irradiated with helium* (in Effects of Radiation on Materials, Ed.by R.E.Stoller, Philadelphia, pp.263-270, 1989)

[8] V.O.Kharchenko, D.O.Kharchenko, Eur.Phys.Jour.B, **85**, 383 (2012);V.O.Kharchenko, D.O.Kharchenko, Cond.Mat.Phys., **16**, 33001 (2013);D.O.Kharchenko, V.O.Kharchenko, A.I.Bashtova, Rad.Eff. and Def. in Sol., **169**, N 5, 418, (2014)

ALERT: A Low Energy Recoil Detector

G. Charles[a]

[a] *Institut de Physique Nucléaire d'Orsay, CNRS-IN2P3, Université Paris-Sud, Université Paris-Saclay*

Abstract

We present here a preliminary study of a tracker that could be used to reconstruct recoil nuclei fragments at CLAS. The main characteristics of this tracker are its ability to reconstruct protons with a minimum momentum of about 70 MeV/c and to identify all particles with a mass between the proton and the alpha. The detectors have also been selected in order to be included in the trigger to ensure a fast event selection. This paper focused on the state of our research on the project as well as on the expected performances obtained from simulations.

Keywords: Tracker, Drift chamber, stereo-angle, hadronic physics

1 Introduction

The ALERT tracker is intended to be used at Jefferson Laboratory (JLab) is located in Virginia (USA). It is an electron accelerator facility, with a beam of energy up to 12 GeV now accessible after the recent three years long upgrade. The beam will be distributed to four halls and in particular in Hall B where the CLAS12 experiment will start taking data at the end of 2016. With the predecessor of CLAS12, CLAS [1], a whole new physics program has emerged based on the use of detectors dedicated to low energy nuclear recoils (kinetic energy of few MeV). The recoils are produced during high energy reactions such as deep inelastic scattering (DIS) eA $\rightarrow$ eX or deep virtual Compton Scattering (DVCS) eA $\rightarrow$ eA. In particular, radial time projection chambers (rTPC) were successfully used in CLAS to measure the structure function of the free neutron by tagging slow protons out of deuterium targets [2] and to measure coherent DVCS off helium nuclei [3]. An international group of scientists from the CLAS collaboration has formed around the project of creating a new nuclear recoil detector for the upgraded CLAS12. We seek to develop a new detector offering better timing and spatial resolution as well as better particle identification than the previous rTPCs [4].

2 Detector setup

The construction of a low energy recoil detector for CLAS12 is challenging in many aspects. Indeed such detector will have to run in a high rate region (several MHz of protons in particular) in a very strong magnetic field (5T) due to the magnetic shield of the CLAS12 spectrometer. At the same time it needs to provide fast and precise response (< 2 μs) in order to be used by the trigger, in coincidence with the normal CLAS12 trigger. Finally, in order to detect the recoil before they are absorbed in any materials the chamber needs to be right around the target. We envision a 30 cm long detector with a radius of 10 cm surrounding a 30 cm long gaseous target at 3 bars, the layout can be seen figure 1.

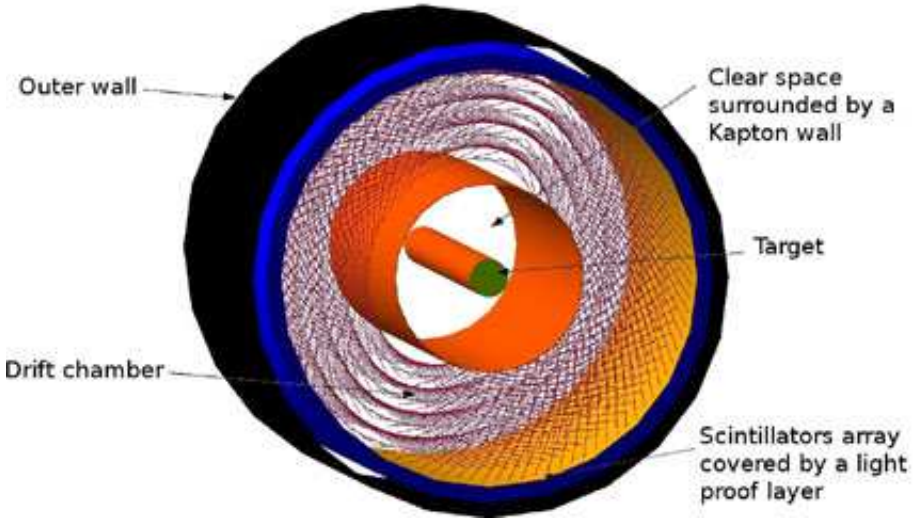
Outer wall
Clear space surrounded by a Kapton wall
Target
Drift chamber
Scintillators array covered by a light proof layer

Figure 1: Schematic layout of the detector, viewed from the beam direction.

2.1 Drift chamber

The drift chamber is composed of 8 layers of sense wires. The later are each surrounded by field wires to create the electric field. The geometry of the basic cell, composed of one sense wire and a certain number of field wires, needs to be determined. The cell must ensure a good uniformity of the electric field around the sense wire but the total number of wires should be as low as possible to reduce multiple scattering, the total tension on the forward end plate and the number of particles stopped by the wires. The quantity of material in the detector can also be limited by using lighter wires, such as aluminium wires or any other light conductive material.

As mentionned earlier, the thickness of the forward end plate is critical as the scattered electrons will go through it. In order to keep it thin, the wires will be readout only on one side of the chamber. The position along the beam axis is thus determined by the stero-angle given to the wires. This angle will probably be between 10° and 15°. Its value will be tuned by simulations.

The last key parameter of the drift chamber is the space between the wires. Indeed, it influences the speed and the precision of the detector.

To optimize the parameters, tests on a prototype will be carried out. It will be an 8 layer drift chamber. Each layer will have either a different cell geometry or different spacing between wires (from 1.5 mm to 3 mm). We will also test different gas mixtures to study its influence on the efficiency and the speed of the detector.

2.2 Scintillators

The scintillators are used to measure the time of flight for particle identification. The main aspects considered to determine their size and material are the following ones:

- Simulations have shown that a resolution of 200 ps or less may be necessary to perform separation at an acceptable level (see next section)

- They should have a granularity that will allow a matching with the drift chamber without ambiguity
- Precise light detection in a 5 T magnetic field when coupled to a silicon based photo-detectors
- Number of channels and cost

The preliminary design for the scintillators is based on a multi-layer array of which the granularity still remains to be determined. The layer closest to the beam would be thinner to detect alpha and low momentum particles and give a good time resolution. The second layer would stop the particles to determine their energy. The use of several thin layers of scintillators will also help to differentiate the different nuclear species which are penetrating the scintillators differently. In particular time of flight has difficulties differentiating nuclei that have same mass/charge ratio.

2.3 Electronics

The main requirements for the electronics is to have a 10 ns time resolution or better while keeping an energy resolution that allows particle identification through energy deposition in the detector. In this project, we will perform tests on electronics initially developed for other detectors and eventually propose modifications. First, we will investigate the possibility to use stand-alone preamplifiers. Based on the gain in the drift chamber and the number of primary ionizations, it should be possible to use a design similar to the one developed for the Heavy Photon Search [5] experiment installed in the Hall B. The main challenge is to adapt the board and elements to the higher voltages (up to 2 kV for the drift chamber). The time resolution has already been shown to be around 2 ns [5], so well below our 10 ns requirement. However, more studies will be needed to evaluate how the gains of the chamber and the preamplifier can be tuned to ensure a signal over noise ratio that allows to discriminate electrons from protons and light nuclei between each other (p, 2H, 3H, 3He and 4He). Second, we will study the possible use of DREAM electronics [6] which was developed for the Micromegas detectors of CLAS12. A charge simulator of drift chamber wire signal will be built and used with existing electronics in order to optimize its parameters for our application: sampling frequency, peaking time and gain. Like the previous solution, it has the advantage to be already compatible with the CLAS12 data acquisition system.

3 Expected performances

3.1 Implementation

A simulation of ALERT has been developed using Geant4 [7]. In order to include multiple scattering and energy loss effects, all the different layers and elements, in particular the wires, have been included. A Kalman filter is under development but for now the fitting algorithm is using a global helix fit. The point coordinates sent to the fit are given by using the particle path returned by Geant4 and smearing its position each time it crosses a signal wire layer by the resolutions expected. The resolutions are given by the product of the time resolution (10 ns) by the drift speed ($\approx 2 \cdot 10^4$ m·s^{-1}) expected in the ^{4}He (90%)- iC_4H_{10} mixture in a plan

perpendicular to the wire. The resolution along the wire also takes into account the stereo-angle.

3.2 Acceptance and resolutions

Figures 2 and 3 show from top left to bottom right, the angular resolutions, the z resolution, where z is the coordinate along the beam axis, and the transverse momentum resolution at the vertex for protons and for alphas. To understand the acceptance, it is important to notice that a particle is considered detected when it reaches the scintillators.

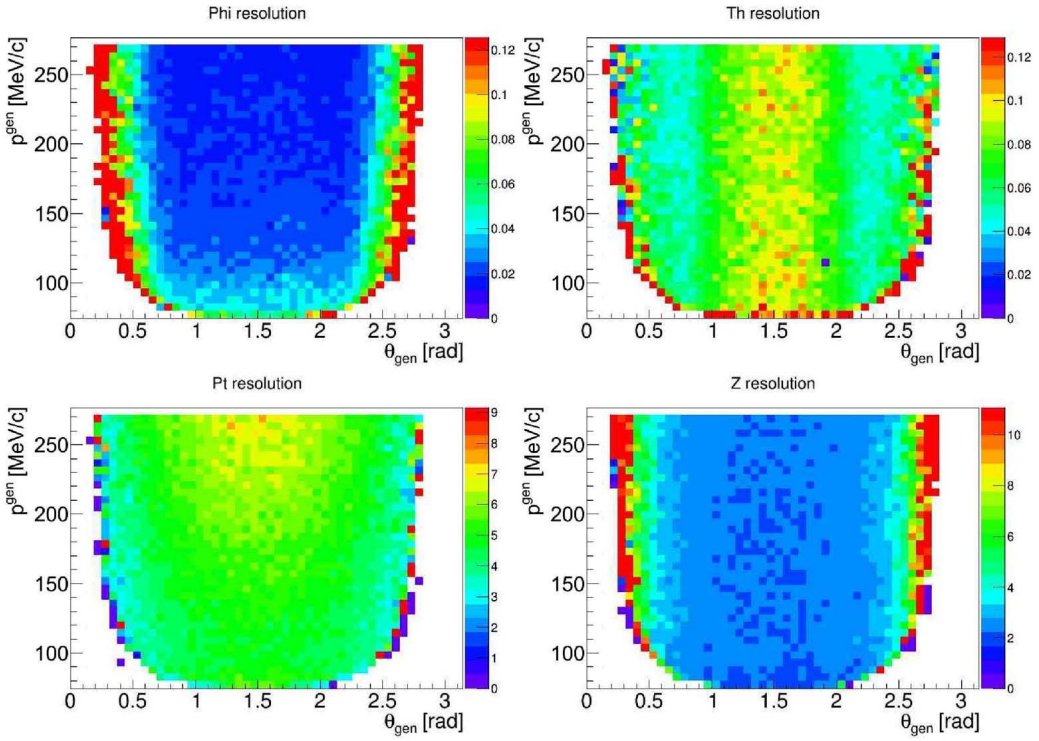

Figure 2: Expected time of arrival as a function of the radius of the trajectory for protons.

As expected the acceptance is larger near $\pi/2$ as the particle goes through less material when emitted at this angle. Also the resolutions for alphas are generally better than for protons due to the fact that the curvature is larger making the fit easier. A fast Monte Carlo using the acceptances and energy resolutions has been made available for collaborators. Conclusions concerning the match between our design and their needs will then be made.

3.3 Particle identification

One of the key point of this detector is its ability to differenciate different species. The differentiation relies upon the time of arrival in the scintillators, the initial time being given by another particle reconstructed by the rest of CLAS12, and the reconstructed radius in the drift chamber (fig. 4).

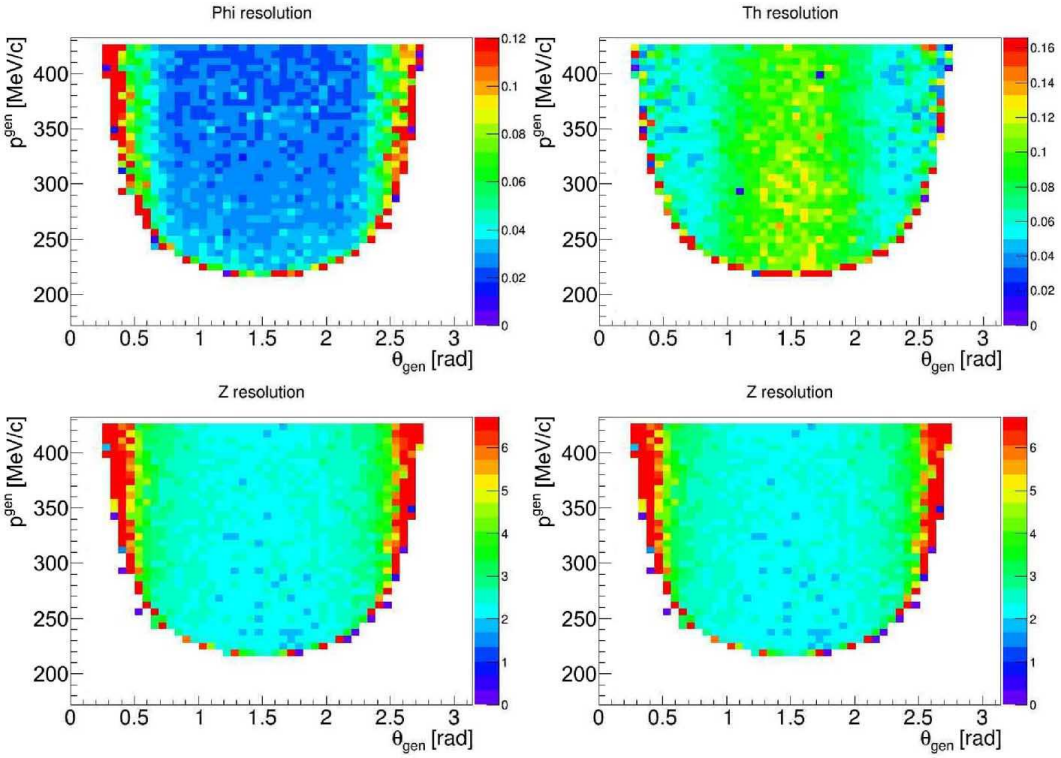

Figure 3: Expected time of arrival as a function of the radius of the trajectory for alpha particles.

As one can see, this method allows to separate clearly almost all kind of species we are interested in. To discriminate ^{2}H from α a more traditional method based on the energy deposited in the drift chamber and/or the scintillators will be used.

4 Conclusions

The preliminary design shows that the speed, precision as well as separation power of a drift chamber coupled with an array of scintillators fullfills the needs of the second generation of experiments measuring recoil nuclei fragments. Two prototypes will be build in the next years. These prototypes will permit to finalize the design of the detector. In the mean time, collaborators will use the available fast Monte Carlo to check if it meets their needs. Finally, depending on the results of the two previous steps, the ALERT collaboration will submit a proposal to conduct experiment at CLAS12 using the detector described here.

5 Acknowledgement

The support of the LIA project is greatly acknowledged. This work was supported by a grant from the French National Research Agency (ANR) as part of the Jeunes chercheuses et jeunes chercheurs Programme (ANR-13-JS05-0001).

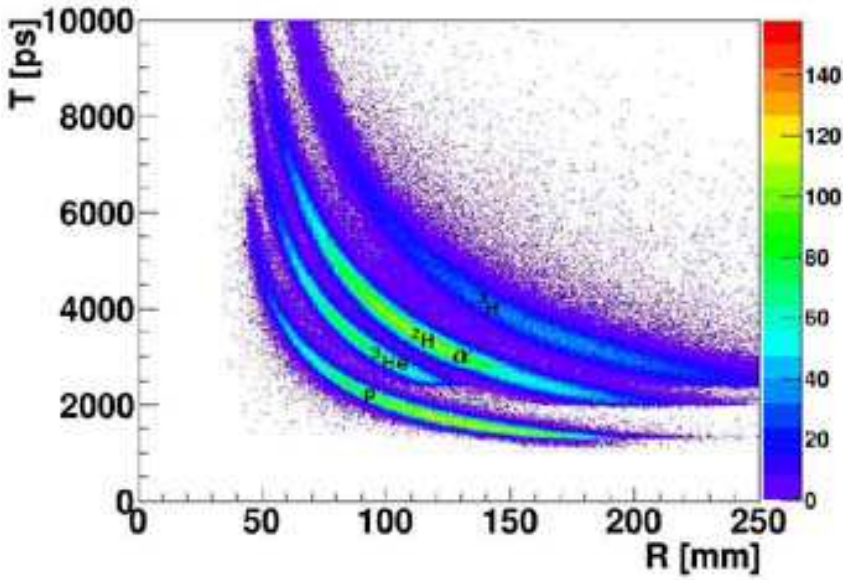

Figure 4: Expected time of arrival as a function of the radius of the trajectory for different particles.

References

[1] *The CEBAF large acceptance spectrometer (CLAS)*, B.A. Mecking et al., Nucl. Instr. Meth. A 503, 513 (2003)

[2] *Measurement of the Neutron F2 Structure Function via Spectator Tagging with CLAS*, N. Baillie et al. Phys. Rev. Lett. 108, 142001

[3] *Helium Compton Form Factor Measurements at CLAS, Jefferson Lab, CLAS Collaboration*, E. Voutier for the CLAS collaboration PoS DIS2013 (2013) 057

[4] *BoNuS: Development and Use of a Radial TPC using Cylindrical GEMs*, H. C. Fenker et al. Nucl.Instrum.Meth. A592 (2008) 273-286

[5] *The Heavy Photon Search Test Detector*, M. Battaglieri et al. Nucl.Instrum.Meth. A777 (2014) 91-101

[6] *Mise au point de dtecteur Micromegas pour l'exprience CLAS12 au laboratoire Jefferson*, G. Charles, PhD thesis, 2013

[7] *Geant4a simulation toolkit*, S. Agostinelli et al., Nucl. Instr. Meth. A 506 (2003) 250-303

Molybdenum containing scintillating bolometers for double-beta decay search (LUMINEU program)

D.V. Poda[a,b], L. Bergé[a], R.S. Boiko[b], M. Chapellier[a], D.M. Chernyak[b], N. Coron[c], F.A. Danevich[b], L. Devoyon[d], A.-A. Drillien[a], L. Dumoulin[a], C. Enss[e], A. Fleischmann[e], L. Gastaldo[e], A. Giuliani[a,f,g], D. Gray[h], M. Gros[h], S. Hervé[h], V. Humbert[a], I.M. Ivanov[i], A. Juillard[j], V.V. Kobychev[b], F. Koskas[d], M. Loidl[k], P. Magnier[h], E.P. Makarov[i], M. Mancuso[a,f], P. de Marcillac[a], S. Marnieros[a], C. Marrache-Kikuchi[a], X.-F. Navick[h], C. Nones[h], E. Olivieri[a], B. Paul[h], Y. Penichot[h], G. Pessina[g,l], O. Plantevin[a], T. Redon[c], M. Rodrigues[k], V.N. Shlegel[i], O. Strazzer[d], M. Tenconi[a], L. Torres[c], V.I. Tretyak[b,m], Ya.V. Vasiliev[i], M. Velazquez[n] and O. Viraphong[n] (LUMINEU Collaboration)

[a] *CSNSM, Univ. Paris-Sud, CNRS/IN2P3, Université Paris-Saclay, 91405 Orsay, France*
[b] *Institute for Nuclear Research, MSP 03680 Kyiv, Ukraine*
[c] *IAS, CNRS, Univ. Paris-Sud, 91405 Orsay, France*
[d] *CEA, Centre d'Etudes Saclay, Orphée, 91191 Gif-Sur-Yvette Cedex, France*
[e] *Institut für Angewandte Physik, Universität Heidelberg, D-69120 Heidelberg, Germany*
[f] *Dipartimento di Scienza e Alta Tecnologia dell'Università dell'Insubria, I-22100 Como, Italy*
[g] *INFN, Sezione di Milano-Bicocca, I-20126 Milano, Italy*
[h] *CEA, Centre d'Etudes Saclay, IRFU, 91191 Gif-Sur-Yvette Cedex, France*
[i] *Nikolaev Institute of Inorganic Chemistry, 630090 Novosibirsk, Russia*
[j] *IPNL, Université de Lyon, Université Lyon 1, CNRS/IN2P3, 69622 Villeurbanne Cedex, France*
[k] *CEA, LIST, Laboratoire National Henri Becquerel, 91191 Gif-Sur-Yvette Cedex, France*
[l] *Dipartimento di Fisica, Università di Milano-Bicocca, I-20126 Milano, Italy*
[m] *INFN, Sezione di Roma, I-00185 Roma, Italy*
[n] *ICMCB, CNRS, Université de Bordeaux, 33608 Pessac Cedex, France*

Abstract

A scintillating bolometer technology, promising to be used in a next-generation cryogenic experiment to search for neutrinoless double-beta decay, is currently under development within the LUMINEU (Luminescent Underground Molybdenum Investigation for NEUtrino mass and nature) program. The recent results about the R&D of high quality large volume molybdenum containing crystal scintillators (zinc and lithium molybdates), including ones produced from ^{100}Mo-enriched powder, and aboveground / underground tests of cryogenic detectors based on these crystals are presented here.

Keywords: Double-beta decay, Scintillating bolometer, $ZnMoO_4$, Li_2MoO_4, Low background experiment, Radiopurity

1 Introduction

The recent discovery of neutrino oscillations (the Nobel prize award in physics 2015), phenomena which demonstrate that neutrinos have mass [1], stirs up an additional great interest in

the searches for neutrinoless double-beta ($0\nu2\beta$) decay, a nuclear transformation of the type $(A, Z) \rightarrow (A, Z + 2) + 2e^-$. This never observed process is beyond the Standard Model (SM) and definitely requires finite value of neutrino mass, equivalence between neutrino and anti-neutrino (Majorana nature of neutrinos), and violation of the total lepton number by two units (see details in the recent review [2] and references herein).

The LUMINEU (Luminescent Underground Molybdenum Investigation for NEUtrino mass and nature) program [3, 4] is going to bridge the gap for high-sensitivity next-generation $0\nu2\beta$ studies by the development of a technology based on Mo-containing scintillating bolometers, heat-light double read-out cryogenic calorimeters, and the demonstration of its feasibility by the successful realization of a small-scale experiment to search for $0\nu2\beta$ decay of ^{100}Mo with zero background in the range of interest (around $Q_{2\beta} = 3034$ keV, the total energy of the two electrons emitted in $0\nu2\beta$ decay of ^{100}Mo). It will play an important role in the selection for the technology to be adopted for a tonne-scale cryogenic $0\nu2\beta$ experiment within the CUPID (CUORE Upgrade with Particle IDentification) project [5]. The main R&D results in the framework of the LUMINEU program are briefly presented here.

2 R&D of scintillating bolometers within LUMINEU

2.1 Tasks of the LUMINEU program

LUMINEU is performing an extensive R&D of Mo-containing scintillating bolometers which involves several general tasks related with: I) crystal scintillators; II) light detectors; III) temperature sensors; IV) prototypes of scintillating bolometers; V) final detectors for a pilot $0\nu2\beta$ experiment. Below we describe briefly the program and the main requirements of these tasks.

A high detection efficiency for $0\nu2\beta$ decay can be obtained in an experiment with the so-called "active-source" technique for which a $0\nu2\beta$ source (e.g. ^{100}Mo) is embedded into a detector. The baseline detector material for LUMINEU is a zinc molybdate ($ZnMoO_4$) scintillator, however another promising Mo-based material, lithium molybdate (Li_2MoO_4), is also under consideration. Therefore, task I is devoted to the development of purification and crystallization procedures for producing large volume, high optical quality, radiopure scintillators both from natural and ^{100}Mo-enriched molybdenum. In view of the high cost of enriched ^{100}Mo and the prospect to grow $\sim$ 1000 crystals (for a large-scale project), one needs to optimize a production line in order to get high throughput and low irrecoverable losses of the enriched material. Specifying these requirements, the main objectives are scintillators with a mass of $\sim$ 1 kg (scintillation elements up to 0.4 kg) produced with more than 70% crystal yield, a few % of irrecoverable losses, and with a level of internal radioactive contamination by ^{228}Th and ^{226}Ra $\leq$ 0.01 mBq/kg (the total alpha activity of radionuclides from U/Th, except that of ^{210}Po, is below 1 mBq/kg).

The main background source above 2615 keV in a bolometric $0\nu2\beta$ experiment is caused by α decays of natural radioactivity. Usually, a scintillator produces less light for α particles with respect to $\gamma(\beta)$'s of the same energy (this phenomenon is known as quenching). Therefore, by using a light detector complementary to a bolometer which scintillates at low temperature, one can efficiently discriminate an α-induced background. It is convenient to make this light detector as a thin bolometer and mount it close to a scintillator-based bolometer, which all

together constitute a scintillating bolometer. Therefore, task II includes the fabrication of optical bolometers from high purity Ge wafers, widely used for this purpose. An important part of the activity within this task is dedicated to the optimization of light detectors with the aim to get an acceptable performance. Since both $ZnMoO_4$ and Li_2MoO_4 scintillators are characterized by very modest light yield (of the order of $\sim$ 1 keV per 1 MeV deposited energy), efficient light collection and absorption are important parameters. The energy resolution (FWHM) of the photodetector should be good enough to provide a 99.9% discrimination between light signals caused by $\sim$ 3 MeV $\gamma(\beta)$ and α particles impinging in the Mo-based scintillator. In particular, an α/γ separation at the level of 5σ at $\sim$ 3 MeV can be achieved with a light detector characterized by FWHM $\sim$ 15% at 5.9 keV X-ray of ^{55}Fe (typically used for calibration of these devices) [6]. Finally, random coincidences of two neutrino double-beta decay of ^{100}Mo, allowed in the SM process and registered with a half-life $\sim 10^{18}$ yr [1], can constitute a major background for a bolometric $0\nu2\beta$ experiment with Mo-containing scintillators, as it was pointed out for the first time in Ref. [7]. Therefore a light detector should have a fast response (e.g. a rise time $\sim$ 1 ms or less) and an as high as possible signal-to-noise ratio to provide an efficient discrimination of random coincidences.

A small temperature rise appeared after particle interaction inside a bolometer can be measured by a dedicated thermometer. Within task III, LUMINEU is developing three technologies of temperature sensors: Neutron Transmutation Doped (NTD) Ge thermistors [8], superconducting Transition-Edge Sensors (TES) [9], and Magnetic Metallic Calorimeters (MMC) [10]. The first two types exploit the dependence of resistivity on temperature, while the last one that of magnetization on temperature. All results given below were obtained with scintillating bolometers instrumented with NTD Ge-based thermometers.

Task IV involves the construction of small / middle size prototypes of scintillating bolometers and their low temperature test, below tens mK, both at aboveground (at CSNSM) and underground (at Modane in France and Gran Sasso in Italy) cryogenic facilities. The crucial point of this activity is achieving excellent performance of Mo-containing scintillating bolometers in terms of energy resolution (FWHM $\leq$ 10 keV at 3 MeV) and particle identification (α/γ separation more than 99.9%), as well as proving low bulk radioactive contamination of crystals.

Task V requires the fabrication of at least two complete single modules based on massive $ZnMoO_4$ crystals (with mass up to 0.4 kg; one produced from natural molybdenum and another one enriched in ^{100}Mo), and a realization of a pilot experiment with the aim to demonstrate the abovementioned key performance and radiopurity, which are associated with a zero-background $0\nu2\beta$ experiment. Current status of the LUMINEU tasks are briefly summarized below (task III will not be highlighted here in more detail than it was done above).

2.2 R&D and preformance of Mo-containing scintillating bolometers

A technology of fabrication of large area light detectors (with diameter up to 50 mm and thickness around 250 μm) from high purity germanium wafers (Umicore, Belgium) was developed at CSNSM (Orsay, France) [6]. The adopted LUMINEU standard is a $\oslash$44-mm Ge slab coated by SiO to improve light absorption [11]. In addition to the batch of the LUMINEU NTD Ge-based light detectors, photodetectors produced within the LUCIFER $0\nu2\beta$ project [12], as well as state-of-the-art extra thin ($\sim$ 30–50 μm) germanium optical bolometers developed at IAS (Orsay, France) [13] were used to build and test LUMINEU scintillating bolometers. First test

of MMC-based light detectors developed within LUMINEU [14] demonstrate their potential to get $\sim$ 100 times faster response than that typical for NTD Ge-based photodetectors.

A dedicated protocol for molybdenum purification (double sublimation of molybdenum oxide in vacuum and double recrystallization of ammonium molybdate from aqueous solutions) has been adopted by LUMINEU to get high purity initial compound for crystal growth [4]. The chosen advanced directional solidification method developed at NIIC (Novosibirsk, Russia), low-thermal-gradient Czochralski (LTG Cz) technique, demonstrates the possibility to grow large (up to 1.5 kg) $ZnMoO_4$ crystals with a high crystal yield ($\sim$ 80% of charge) [4]. The aboveground low temperature test of first LUMINEU crystals (scintillation elements with size of $\oslash$20×40 mm and $\oslash$35×40 mm and masses of 55 g and 160 g respectively), produced from $ZnMoO_4$ boules grown from deeply purified materials, shows excellent signal-to-noise ratio, high signal amplitude, expected values of light-to-heat ratio and light quenching factor for α particles [4]. Only internal ^{210}Po contaminant was clearly observed over about two weeks of data taking which indicates high crystals' radiopurity and effectiveness of the purification procedure.

Advances in large volume $ZnMoO_4$ growth have been achieved by applying double crystallization. In particular, by using this technique an improved quality $\sim$ 1.0 kg boule was grown from molybdenum purified by double recrystallization [15]. Two $ZnMoO_4$ optical elements produced with a size expected for a pilot LUMINEU $0\nu2\beta$ experiment ($\oslash$50×40 mm; masses 336 and 334 g) were used to construct identical scintillating bolometers [16] according to a new special design compatible with the EDELWEISS set-up at the Modane undeground laboratory (LSM, France). Results of long term (about 3000 h) low background measurements with these devices [15, 17] demonstrate an excellent energy resolution (e.g. FWHM $\sim$ 9 keV at 2615 keV) and an efficient α/γ separation (15σ above 2.5 MeV) achieved with $ZnMoO_4$-based scintillating bolometers, as well as very high internal radiopurity of $ZnMoO_4$ crystals (e.g. activity of ^{228}Th and ^{226}Ra $\leq$ 0.004 mBq/kg), which completely satisfy the LUMINEU requirements and those of a future large-scale experiment. An illustration of the main performance of a 334-g $ZnMoO_4$ detector is shown in Fig. 1. Taking into account that the additional crystallization improves quality of a crystal boule and could also enhance bulk radiopurity thanks to segregation of radionuclides during growing process, double crystallization can be used for the production of large LUMINEU crystals.

A first ^{100}Mo-enriched $Zn^{100}MoO_4$ crystal with a mass of $\sim$ 0.17 kg has been successfully developed with 84% crystal yield and $\sim$ 4% irrecoverable losses of the enriched material [18]. The used $^{100}MoO_3$ (99.5% enrichment in ^{100}Mo) was purified by sublimation in vacuum and double recrystallization from aqueous solutions. Molybdenum purification is related with the major part of losses (85%) and the minor part with the crystal growth. The $Zn^{100}MoO_4$ boule had a non-regular shape and yellow coloration unlike similar size natural $ZnMoO_4$ crystals. It is caused by still existing difficulties during the solidification, in particular by the effect of a second phase formation. A $Zn^{100}MoO_4$ scintillating bolometer array, built from two produced small $Zn^{100}MoO_4$ elements (59 g and 63 g) and tested aboveground, shows bolometric properties similar to non-enriched $ZnMoO_4$ detectors [18]. The energy resolution of both bolometers was reasonably good taking into account a high counting rate due to the background conditions of the sea-level laboratory. In particular, 5 and 10 keV FWHM at 609 keV γ's of ^{214}Bi from environmental radioactivity was obtained with the 59-g and 63-g $Zn^{100}MoO_4$ bolometers respectively [18]. After 42 h of data taking only a hint associated with ^{210}Po was observed in the α region, which implies encouraging radiopurity of the crystals [18]. During an underground

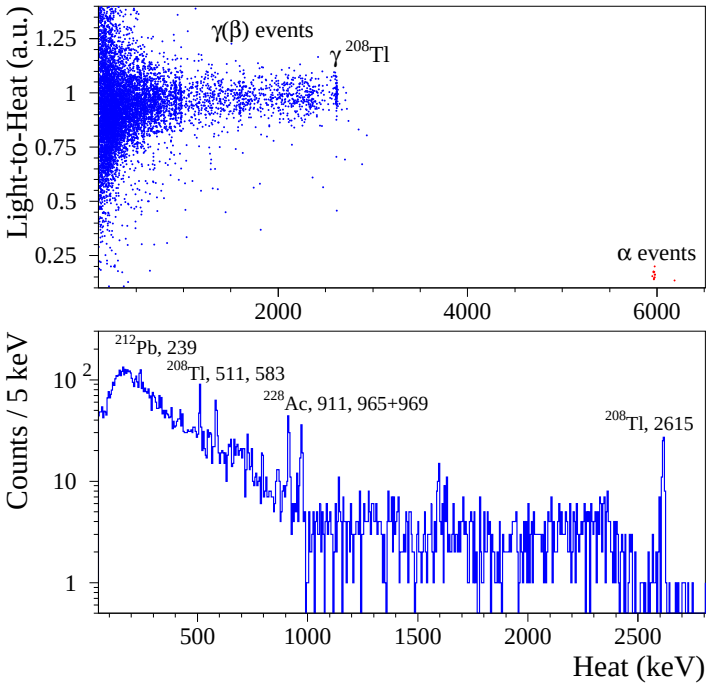

Figure 1: (Top) A 2-D histogram showing light-to-heat ratio versus heat for the data of the 14-h ^{232}Th calibration measurements with the 334-g $ZnMoO_4$-based scintillating bolometer operated in the EDELWEISS set-up at LSM. A high potential of full separation between α events and $\gamma(\beta)$ band (red and blue dots respectively) is clearly evident. The region, where events caused by decays of α radionuclides from U/Th (above 4 MeV) are expected, is mainly populated by ^{210}Po, which demonstrates encouraging internal radiopurity. (Bottom) 1-D projection of the 2-D histogram shown at the figure top. Energies of γ quanta are given in keV.

test at LSM, the $Zn^{100}MoO_4$ array which had a non-standard holder was strongly affected by a microphonic noise deteriorating the detector's energy resolution. It is caused by the absence of a suspension system in the EDELWEISS set-up (to be implemented soon), which can reduce effect of microphonics, in contrast to the cryostat [19] used for the aboveground measurements. Anyway, a full particle identification by $Zn^{100}MoO_4$ detectors was clearly demonstrated in the underground test.

The $ZnMoO_4$ solidification procedure was further improved by introducing a small amount of tungsten oxide (up to $\sim$ 0.5 wt%) to stabilize the melt and several high quality $\sim$ 0.15-kg crystal boules were grown. No effect of W-doping on bolometric properties of $ZnMoO_4$ was evidenced by the aboveground measurements with a scintillating bolometer array constructed from stoichiometric and W-doped $ZnMoO_4$ crystals ($\oslash$20$\times$40 mm each) [20].

Recently, a first large volume colorless $Zn^{100}MoO_4$ crystal ($\sim$ 1.4 kg) has been developed [17, 21]. Two large scintillation elements were produced with a shape of hexagonal prism (with diagonal 60 mm and height 40 mm, masses 379 g and 382 g) in order to have an improved light output according to studies [22]. Massive $Zn^{100}MoO_4$-based scintillating bolometers have been tested in the CUORE R&D test cryostat at Gran Sasso National Laboratories (LNGS, Italy) and the data analysis is in progress. A new test in the EDELWEISS set-up at Modane is foreseen. Meanwhile, background conditions of a middle-scale $0\nu2\beta$ experiment with 48

$Zn^{100}MoO_4$ scintillating bolometers (⌀60×40 mm, 495 g each) installed in the EDELWEISS set-up have been simulated with GEANT4-based code [21]. Considering the already achieved performance, radiopurity, and pulse-shape discrimination of random coincidences developed by LUMINEU [23], a background counting rate $\approx 5\times10^{-4}$ counts/yr/kg/keV at $Q_{2\beta}$ of ^{100}Mo, corresponding to zero-background conditions, can be reached [21].

In spite of the achieved progress in the development of large $Zn^{100}MoO_4$, growing a regular cylindrical shape crystal boule with similar quality along its length is still a difficult task (e.g. see Fig. 1 in [17]). This problem can be resolved, without further R&D, just by pulling a short crystal boule. Another solution could be related with a choice of another Mo-based material, Li_2MoO_4, which is characterized by comparatively easy crystal growth process and has bolometric properties similar to $ZnMoO_4$. In particular, several perfect quality Li_2MoO_4 crystal boules with masses 0.1–0.4 kg were grown by LTG Cz method from deeply purified Mo and commercial Li_2CO_3 (99.99% purity grade) [24]. A first large Li_2MoO_4-based (⌀40×40 mm, 151 g) scintillating bolometer was tested aboveground with quite encouraging results [24], which were reinforced by subsequent $\sim$ 350-h underground measurements at LNGS [25]. In particular, an excellent spectrometric properties (FWHM $\sim$ 4 keV at 2615 keV), an efficient particle identification and high radiopurity for U/Th nuclides (^{228}Th and ^{226}Ra $\leq$ 0.02 mBq/kg) were obtained [25]. There is only an issue caused by considerably high activity of ^{40}K inside the tested crystal ($\sim$60 mBq/kg), which can be a problem due to random coincidences in a future $0\nu2\beta$ experiment. Fortunately, this issue can be easily resolved by selection of a Li-containing raw material with low concentration of ^{40}K and by recrystallization of Li_2MoO_4 crystals. It is worth to note that two scintillating bolometers based on large Li_2MoO_4 crystals (⌀50×40 mm, 242 g each) produced from different Li-based powder with low ^{40}K content (tested by HPGe γ spectroscopy) are under investigation in order to prove low bulk activity of ^{40}K. A Li-powder with the lowest ^{40}K content will be used to produce a first $Li_2{}^{100}MoO_4$ crystal. A dedicated low temperature test will be performed in order to completely demonstrate that Li_2MoO_4-based scintillating bolometer is a viable detector for a large-scale cryogenic $0\nu2\beta$ experiment.

3 Conclusions

A protocol for producing high quality large volume Mo-containing crystal scintillators from deeply purified molybdenum with both natural isotopic composition and enriched in ^{100}Mo has been developed within the LUMINEU program. A technology for the development of high performance LUMINEU single modules based on radiopure large $ZnMoO_4$ and Li_2MoO_4 crystals is well established providing high energy resolution (better than 10 keV FWHM at 2615 keV), efficient α/γ separation (more than 5σ) and required low level of bulk radioactivity (e.g. ^{228}Th and ^{226}Ra $\sim$ 0.01 mBq/kg). A first large $Zn^{100}MoO_4$ crystal ($\sim$ 1.4 kg) was successfully grown and two 0.4-kg $Zn^{100}MoO_4$-based scintillating bolometers have been preliminary tested at LNGS (Italy). The development of a first large $Li_2{}^{100}MoO_4$ crystal scintillator is in progress and a pilot LUMINEU test of massive $Zn^{100}MoO_4$- and $Li_2{}^{100}MoO_4$-based scintillating bolometers in the EDELWEISS set-up at LSM (France) is foreseen at the beginning of 2016. After completing this test we will make a final choice about the Mo-containing crystals to be produced from $\sim$ 10 kg of ^{100}Mo (enriched isotope is already available) for a middle-scale $0\nu2\beta$ experiment (LUCINEU project) based on the LUMINEU technology. A Monte Carlo simulation of 48 0.5-kg $Zn^{100}MoO_4$-based scintillating bolometers installed in the EDELWEISS set-up demonstrates

the possibility to get a satisfactory low background counting rate in the range of interest (at $\sim$ 3 MeV). The LUMINEU activity is now part of the CUPID project, a proposed bolometric tonne-scale $0\nu2\beta$ experiment experiment to be built as a follow-up to CUORE and exploiting as much as possible the CUORE infrastructures.

4 Acknowledgements

This work is part of the LUMINEU project funded by the Agence Nationale de la Recherche (ANR, France). The Li_2MoO_4 aboveground test was performed with the determinant contribution of ISOTTA, a R&D ASPERA common call. The Ukrainian group was supported in part by the IDEATE International Associated Laboratory (LIA). DVP was supported by the P2IO LabEx (ANR-10-LABX-0038) in the framework "Investissements d'Avenir" (ANR-11-IDEX-0003-01) managed by the ANR (France).

References

[1] K.A. Olive et al. (Particle Data Group), *Review of Particle Physics*, Chin. Phys. C 38 (2014) 090001 and 2015 update.

[2] S.M. Bilenky, C. Giunti, *Neutrinoless double-beta decay: A probe of physics beyond the Standard Model*, Int. J. Mod. Phys. A 30 (2015) 1530001.

[3] M. Tenconi for the LUMINEU collaboration, *LUMINEU: a pilote scintillating bolometer experiment for neutrinoless double beta decay search*, Phys. Proc. 61 (2015) 782.

[4] L. Bergé et al., *Purification of molybdenum, growth and characterization of medium volume $ZnMoO_4$ crystals for the LUMINEU program*, JINST 9 (2014) P06004.

[5] G. Wang et al. (The CUPID Interest Group), *CUPID: CUORE (Cryogenic Underground Observatory for Rare Events) Upgrade with Particle IDentification*, arXiv:1504.03599 [physics.ins-det] (2015);
G. Wang et al. (The CUPID Interest Group), *R&D towards CUPID (CUORE Upgrade with Particle IDentification)*, arXiv:1504.03612 [physics.ins-det] (2015).

[6] M. Tenconi, *Development of luminescent bolometers and light detectors for neutrinoless double beta decay search*, Ph.D. thesis, University Paris-Sud, Orsay, France (2015).

[7] J.W. Beeman et al., *A next-generation neutrinoless double beta decay experiment based on $ZnMoO_4$ scintillating bolometers*, Phys. Lett. B 710 (2012) 318.

[8] X.-F. Navick et al., *NTD-Ge development in the LUMINEU project for Rare Events searches with cryogenic detectors*, Talk given at 16th Int. Workshop on Low Temperature Detectors (LTD-16), Grenoble, France, 20–24 July 2015.

[9] C. Nones et al., *High-impedance NbSi TES sensors for studying the cosmic microwave background radiation*, Astron. & Astrophys. 548 (2012) A17.

[10] M. Loidl et al., *Concept of metallic magnetic calorimeters for rare event search in the LUMINEU project*, J. Low Temp. Phys. 176 (2014) 624.

[11] M. Mancuso et al., *An experimental study of antireflective coatings in Ge light detectors for scintillating bolometers*, EPJ Web Conf. 65 (2014) 04003.

[12] J.W. Beeman et al., *Characterization of bolometric Light Detectors for rare event searches*, JINST 8 (2013) P07021.

[13] N. Coron et al., *Highly sensitive large-area bolometers for scintillation studies below 100 mK*, Opt. Eng. 43 (2004) 1568.

[14] D. Gray et al., *A large area light detector for scintillators in rare event searches developed in the LUMINEU context*, Talk given at 16th Int. Workshop on Low Temperature Detectors (LTD-16), Grenoble, France, 20–24 July 2015.

[15] E. Armengaud et al. (the LUMINEU and the EDELWEISS collaborations), *Development and underground test of radiopure $ZnMoO_4$ scintillating bolometers for the LUMINEU $0\nu2\beta$ project*, JINST 10 (2015) P05007.

[16] D.V. Poda for the LUMINEU and the EDELWEISS Collaborations, *Scintillating bolometers based on $ZnMoO_4$ and $Zn^{100}MoO_4$ crystals to search for $0\nu2\beta$ decay of ^{100}Mo (LUMINEU project): first tests at the Modane Underground Laboratory*, Accepted for publication in Nucl. Part. Phys. Proc., DOI: 10.1016/j.nuclphysbps.2015.09.290; arXiv:1502.01161 [physics.ins-det] (2015).

[17] D.V. Poda et al., *Radiopure $ZnMoO_4$ scintillating bolometers for the LUMINEU double-beta experiment*, AIP Conf. Proc. 1672 (2015) 040003.

[18] A.S. Barabash et al., *Enriched $Zn^{100}MoO_4$ scintillating bolometers to search for $0\nu2\beta$ decay of ^{100}Mo with the LUMINEU experiment*, Eur. Phys. J. C 74 (2014) 3133.

[19] M. Mancuso et al., *An aboveground pulse-tube-based bolometric test facility for the validation of the LUMINEU $ZnMoO_4$ crystals*, J. Low Temp. Phys. 176 (2014) 571.

[20] D.M. Chernyak et al., *Effect of tungsten doping on $ZnMoO_4$ scintillating bolometer performance*, Opt. Mater. 49 (2015) 67.

[21] F.A. Danevich et al., *Status of LUMINEU program to search for neutrinoless double beta decay of ^{100}Mo with cryogenic $ZnMoO_4$ scintillating bolometers*, AIP Conf. Proc. 1686 (2015) 020007.

[22] F.A. Danevich et al., *Optimization of light collection from crystal scintillators for cryogenic experiments*, Nucl. Instrum. Meth. A 741 (2014) 41.

[23] D.M. Chernyak et al., *Rejection of randomly coinciding events in $ZnMoO_4$ scintillating bolometers*, Eur. Phys. J. C 74 (2014) 2913.

[24] T.B. Bekker et al., *Aboveground test of an advanced Li_2MoO_4 scintillating bolometer to search for neutrinoless double beta decay of ^{100}Mo*, Astropart. Phys. 72 (2016) 38.

[25] L. Pattavina, *Scintillating bolometers of LMO in LNGS*, Talk given at fourth and final general meeting of the ISOTTA project, Orsay, France, 1–2 December 2014.